


Spring 1-1-2015

Direct Optical Ice Sensing and Closed-Loop Controller Design for Active De-icing of Wind Turbines Using Distributed Heating

Shervin Shajiee

University of Colorado Boulder, shervin.shajiee@colorado.edu

Follow this and additional works at: https://scholar.colorado.edu/asen_gradetds

 Part of the [Aeronautical Vehicles Commons](#), and the [Systems Engineering and Multidisciplinary Design Optimization Commons](#)

Recommended Citation

Shajiee, Shervin, "Direct Optical Ice Sensing and Closed-Loop Controller Design for Active De-icing of Wind Turbines Using Distributed Heating" (2015). *Aerospace Engineering Sciences Graduate Theses & Dissertations*. 124.
https://scholar.colorado.edu/asen_gradetds/124

This Dissertation is brought to you for free and open access by Aerospace Engineering Sciences at CU Scholar. It has been accepted for inclusion in Aerospace Engineering Sciences Graduate Theses & Dissertations by an authorized administrator of CU Scholar. For more information, please contact cuscholaradmin@colorado.edu.

**Direct Optical Ice Sensing and Closed-Loop Controller Design for
Active De-icing of Wind Turbines Using Distributed Heating**

by

Shervin Shajiee

B.S., Amirkabir University of Technology, 2001

M.S., Sharif University of Technology, 2004

M.S., University of Minnesota, 2008

A thesis submitted to the
Faculty of the Graduate School of the
University of Colorado in partial fulfillment
of the requirements for the degree of
Doctor of Philosophy
Department of Aerospace Engineering Sciences

2015

This thesis entitled:
Direct Optical Ice Sensing and Closed-Loop Controller Design for Active De-icing of Wind Turbines
Using Distributed Heating
written by Shervin Shajiee
has been approved for the Department of Aerospace Engineering Sciences

Lucy Y. Pao

Robert R. McLeod

Date _____

The final copy of this thesis has been examined by the signatories, and we find that both the content and the form meet acceptable presentation standards of scholarly work in the above mentioned discipline.

Shajjee, Shervin (Ph.D., Aerospace Engineering Sciences)

Direct Optical Ice Sensing and Closed-Loop Controller Design for Active De-icing of Wind Turbines Using Distributed Heating

Thesis directed by Lucy Y. Pao

Ice accumulation on wind turbines operating in cold regions reduces power generation by degrading aerodynamic efficiency and causes mass imbalance and fatigue loads on the blades. Due to blade rotation and variation of the pitch angle, different locations on the blade experience large variations of Reynolds number, Nusselt number, heat loss, and non-uniform ice distribution. Hence, applying different amounts of heat flux in different blade locations can provide more effective de-icing for the same total power consumption. This large variation of required heat flux motivates using distributed resistive heating, with the capability of locally adjusting thermal power as a function of location on the blade. The main contributions of this research are developing the experimental feasibility of direct ice sensing using an optical sensing technique as well as development of a computational framework for implementation of closed-loop localized active de-icing using distributed sensing. A script-base module was developed in a commercial finite-element software (ANSYS) which provides the capability of (i) Closed-loop de-icing simulations for a distributed network of sensors and actuators, (ii) investigating different closed-loop thermal control schemes and their de-icing efficiency (iii) optimizing thermal actuation for a distributed resistive heating, and (iv) analyzing different faulty scenarios for sensors and thermal actuators under known faults in the network. Different surrogate models were used to enhance the computational efficiency of this approach. The results showed that optimal value of control parameters in a distributed network of heaters depends on convective heat transfer characteristics, layout of heaters and type of closed-loop controller scheme used for thermal actuation. Furthermore, it was shown that closed-loop control provides much faster de-icing than the open-loop constant heat flux thermal actuation. It was observed both experimentally and numerically that high intensity pulsed thermal actuation slightly improves ice melting but relatively increases the amount of applied thermal stress to the blade structure. This thesis includes: (1) A literature study on different methods of ice detection and

a review on passive and active anti/de-icing techniques on wind turbines, (2) Development of an optical ice sensing method for direct detection of ice on the blade including experimental results, (3) Description of an aero/thermodynamic model, which predicts how much heat flux is needed locally for de-icing under variable atmospheric conditions, (4) Experimental results showing the proof-of-concept of closed-loop de-icing using distributed optical ice sensing, distributed temperature sensing, and resistive heating, and (5) Numerical modeling of ice melting on a blade for different distributed heater layouts and geometries in order to optimize thermal actuation strategy, improve de-icing efficiency, and finally (6) Development of a computational framework for closed-loop active de-icing using distributed localized heating and sensing.

Dedication

To Mahnaz, Abdolhossein, Hooman, Jamshid, and Isabelle for their love and patience

Acknowledgements

First, I would like to express my deepest gratitude to my advisor, Prof. Lucy Y. Pao for her exceptional guidance, patience, endless support as well as the freedom that she gave me during this research. I truly express my extended appreciation for her invaluable guidance and continuous support in every single moment over the past 5 years, her positive attitude and trust in my academic capabilities. She encouraged my research and allowed me to grow as a research scientist. Her advice on both research as well as on my career have been invaluable. I would also thank my academic co-advisor, Professor Robert R. McLeod for his support during my research. His great feedback and comments have improved the quality of my technical writing. I am thankful for his help in providing me with the experimental setup for optical sensing during the first three years of my research.

I would like to express my special thanks to Patrick N. Wagner for his help in building an icing chamber for my research. Also, I would like to thank Dr. Eric D. Moore for his guidance with the Optical Frequency Domain Reflectometry (OFDR) software and for his help in the integration of the closed-loop controller to the optical sensing setup. I would like to thank Dr. Ali Najafi from ANSYS Inc. for assisting in the calculations of the volume of ice residue in ANSYS and assisting in the development of computational modules in ANSYS for the closed-loop simulations of de-icing. Special thanks to ANSYS Inc. and Arin Rouse from ANSYS for the kind support and providing the software license during my research.

I appreciate the help of Dr. Patrick Moriarty from the U.S. National Renewable Energy Laboratory (NREL) for providing a blade part for our test setup, and Kyle Kemble from the Colorado Space Grant Consortium for using their cooling unit while developing the icing chamber for my research. I would like to thank my committee members, Professor Kurt Maute, Dr. Patrick Moriarty, and Dr. Andrew Clifton for

serving as my committee members and for their brilliant comments and feedback for my comprehensive and final exam. I am very grateful to my colleagues including Dr. Eric Simley, Fiona Dunne, Jakob Aho, Dr. Jason Laks, Dr. Hua Zhong, Dr. David Schlipf, Daniel Zalkind, and Arnold Braker for their valuable comments during the progress of this research. I am thankful to Annie Brookover, graduate advisor in the department of aerospace engineering sciences, for her administrative support and advice.

Finally, I would like to dedicate this thesis to my family: Abdolhossein, Mahnaz, Jamshid, Hooman and Isabelle for their patience, love, devotion, encouragement, and support. This research is in the memory of my father, Abdolhossein, for always teaching me to work hard.

This work has been partially supported by Center for Research and Education in Wind (CREW) seed grant during the first two years of my study. I greatly appreciate their support.

Contents

Chapter

| | | |
|----------|---|-----------|
| 1 | Introduction | 1 |
| 1.1 | Motivation | 1 |
| 1.1.1 | Types of Atmospheric Ice accumulation | 3 |
| 1.1.2 | Aerodynamic Power Degradation Due to Icing | 5 |
| 1.2 | Summary of Research Goals | 9 |
| 1.3 | Thesis Contributions | 10 |
| 1.4 | Thesis Outline | 11 |
| 2 | Ice Sensing and Thermal Actuation: Existing and Proposed Methods | 14 |
| 2.1 | Ice Sensing | 14 |
| 2.1.1 | Background Information | 14 |
| 2.1.2 | Proposed Direct Optical Ice Sensing | 15 |
| 2.2 | Ice Mitigation | 19 |
| 2.2.1 | Passive Ice Prevention | 19 |
| 2.2.2 | Active Thermal Actuation | 19 |
| 2.2.3 | Proposed Distributed Thermal Actuation | 20 |
| 3 | Blade Thermodynamics | 23 |
| 3.1 | Calculation of Heat Flux Requirement for De-icing | 23 |
| 3.2 | Variation of Convective Heat Flux for Different Wind Turbine Operating Conditions | 25 |

| | | |
|----------|---|-----------|
| 3.3 | Total Required Heat Flux for De-icing | 27 |
| 4 | De-icing Profitability Analysis | 30 |
| 4.1 | Aerodynamic Power Loss Data for Different Ice Accumulations | 31 |
| 4.2 | Profitability Derivations | 31 |
| 4.3 | Estimated Equipment Cost and Payback Time for the Proposed Active Distributed De-icing . | 34 |
| 5 | Experimental Setup and Closed-Loop Experiments | 36 |
| 5.1 | Experimental Setup Description | 36 |
| 5.2 | Computational Model Validation with Experiments | 40 |
| 5.3 | Closed-Loop De-icing Experimental Results | 43 |
| 5.3.1 | Low Intensity Continuous PID Controller | 44 |
| 5.3.2 | High Intensity Pulse Amplitude Modulation (PAM) | 45 |
| 6 | Evaluating Different Heater Layouts for De-icing Using Constant Heat Flux | 50 |
| 6.1 | Simulations of Different Heater Layouts for a Small-Scale Blade | 50 |
| 6.1.1 | De-icing Performance Metric for Heater Layout Evaluation | 52 |
| 6.1.2 | De-icing Performance Comparison for Different Heater Layouts | 53 |
| 6.2 | Simulations of Different Heater Layouts for a 1.5 MW Blade Tip Segment | 58 |
| 6.2.1 | Non-Uniform Ice Geometry and Boundary Conditions | 59 |
| 6.2.2 | Distributed Heater Layout Configurations | 62 |
| 6.2.3 | De-Icing Performance Metric for Heater Layout Evaluation | 63 |
| 6.2.4 | De-Icing Performance Comparison for Different Heater Layouts | 64 |
| 6.2.5 | Sensitivity Study of Other Boundary Conditions | 67 |
| 7 | Computational Closed-Loop Controller Design for De-icing Using Distributed Resistive Heaters and Temperature Sensors | 75 |
| 7.1 | Model Assumptions | 76 |
| 7.2 | Non-Uniform Ice Geometry and Boundary Conditions | 77 |

| | | |
|----------|---|------------|
| 7.3 | Closed-Loop Simulations of De-icing | 77 |
| 7.3.1 | De-icing Performance Metric for Controller Optimization | 78 |
| 7.3.2 | Proportional Closed-Loop versus Constant Flux De-icing | 80 |
| 7.4 | Controller Gain Optimization for a Distributed Network of Heaters | 87 |
| 7.5 | Analysis of a Known Faulty Temperature Sensor in the Network | 90 |
| 7.6 | Conclusions | 93 |
| 8 | Conclusions and Recommendations | 94 |
| | Bibliography | 98 |
| | Appendix | |
| A | Notation | 102 |
| B | Matlab Codes for Calculations of Sensible and Latent Heat Flux for Ice Melting | 105 |
| C | ANSYS-APDL Codes for Closed-Loop Distributed Thermal Actuation | 112 |
| C.1 | Codes written for the Implementation of a Proportional Closed-Loop Controller | 112 |
| C.1.1 | Heat flux Initialization for a Network of Five Heaters | 112 |
| C.1.2 | Proportional Controller Communicating with the Finite-Element Solver | 113 |
| C.2 | ANSYS Code for Calculation of Volume of Ice Residue | 116 |
| C.3 | ANSYS Code for Calculation of High Temperature Regions on the Blade | 117 |

Tables

Table

| | | |
|-----|--|----|
| 2.1 | Comparison of different methods for active de-icing of wind turbines | 22 |
| 4.1 | De-icing power ratio for different thermal actuation strategies | 30 |
| 6.1 | Quantitative performance cost comparison for different heater layouts modeled on the small blade segment | 58 |
| 6.2 | Quantitative performance cost comparison after one hour of heating at $q = 3000 \text{ Watt/m}^2$ for different heater layouts on the 1.5 MW blade segment | 66 |
| 7.1 | Optimal values of proportional controller parameters for distributed heaters in 5-piece configuration | 90 |

Figures

Figure

| | | |
|-----|--|----|
| 1.1 | Europe Icing Map | 2 |
| 1.2 | Power loss estimation due to icing at different wind speeds | 3 |
| 1.3 | Photos of ice accumulation on some commercial wind turbines | 4 |
| 1.4 | Comparison of lift coefficient (C_L) versus angle of attack (AOA) between a clean and an icy NACA0012 airfoil | 5 |
| 1.5 | Physical properties of ice/water versus temperature | 13 |
| 2.1 | Schematic de-icing control block diagram using direct optical sensing, temperature sensing and resistive heaters | 15 |
| 2.2 | Layout of an optical frequency-domain reflectometer | 16 |
| 2.3 | Experimental detection of water evaporation using optical sensing (OFDR) | 16 |
| 2.4 | Experimental results of direct optical ice sensing using OFDR | 21 |
| 2.5 | Summary of different approaches in the literature for ice sensing and de-icing | 21 |
| 3.1 | Simulated heat flux required for a rotating 500 KW wind turbine blade | 24 |
| 3.2 | Required heat flux versus initial ice temperature for a soft rime-ice layer on a non-rotating rectangular-shape surface with no convection | 29 |
| 4.1 | Anti/De-icing efficiency factor versus wind turbine rated power | 32 |
| 5.1 | Fabricated experimental setup for direct optical ice sensing and closed-loop de-icing | 37 |

| | | |
|------|--|----|
| 5.2 | A wind turbine blade segment equipped with distributed resistive heaters, optical and temperature sensors | 39 |
| 5.3 | Resistive heaters in aligned and staggered configurations | 40 |
| 5.4 | Schematic block diagram of closed-loop de-icing based on temperature and optical ice sensing | 41 |
| 5.5 | Created CAD model of the small-scale blade segment in SolidWorks | 42 |
| 5.6 | Temperature sensor installed on the small-scale blade segment for experimental validation of computational model created in ANSYS | 42 |
| 5.7 | Experimental input voltage to the resistive heaters used for computational model validation . | 47 |
| 5.8 | Validation of the computational model developed in ANSYS with the experiments for a stationary small-scale blade segment | 47 |
| 5.9 | Ice formation inside the fabricated icing chamber | 48 |
| 5.10 | Blade temperature versus input voltage to the heater network experimentally applied using a PID controller | 48 |
| 5.11 | Visual comparison of ice melting between a low intensity continuous PID actuation and a higher intensity PAM actuation with the same amount of electrical energy expenditure . . . | 49 |
| 5.12 | Experimental temperature output comparison between a low intensity continuous PID controller and high intensity PAM controller | 49 |
| 6.1 | Different modeled heater layouts and geometries | 52 |
| 6.2 | CAD model of accumulated ice with a uniform thickness of 3 mm on the small-scale blade segment in ANSYS | 54 |
| 6.3 | Ice residue for different layouts at $t = 200$ seconds after switching on the resistors with an input heat flux of $q = 400 \text{ Watt/m}^2$ | 54 |
| 6.4 | Ice residue for different layouts at $t = 400$ seconds after switching on the resistors with an input heat flux of $q = 400 \text{ Watt/m}^2$ | 55 |
| 6.5 | Ice residue for different layouts at $t = 600$ seconds after switching on the resistors with an input heat flux of $q = 400 \text{ Watt/m}^2$ | 56 |

| | | |
|------|--|----|
| 6.6 | Ice residue for different layouts at $t = 800$ seconds after switching on the resistors with an input heat flux of $q = 400 \text{ Watt/m}^2$ | 57 |
| 6.7 | Modeled glaze ice layer on the tip segment of a 1.5 MW wind turbine blade | 60 |
| 6.8 | Full 1.5 MW wind turbine blade including different segments | 61 |
| 6.9 | Generated mesh for the ice layer and the tip segment of a 1.5 MW wind turbine blade | 61 |
| 6.10 | Convective coefficient of heat transfer h versus spanwise radius normalized by the radius of the tip r/R_{tip} | 62 |
| 6.11 | Different layout of heaters modeled on the 1.5 MW blade segment | 63 |
| 6.12 | Optimizing the magnitude of the uniform heat flux for the 5-piece heater network | 69 |
| 6.13 | De-icing performance cost function for $q = 3000 \text{ Watt/m}^2$ | 69 |
| 6.14 | Percentage of total volume of ice residue vs. time for $q = 3000 \text{ Watt/m}^2$ | 70 |
| 6.15 | Percentage of volume of “LE ice 1” residue vs. time for $q = 3000 \text{ Watt/m}^2$ | 70 |
| 6.16 | Percentage of volume of “LE ice 2” residue vs. time for $q = 3000 \text{ Watt/m}^2$ | 71 |
| 6.17 | Percentage of volume of “Non-LE ice” residue vs. time for $q = 3000 \text{ Watt/m}^2$ | 71 |
| 6.18 | Percentage of $V_{T>30}$ vs. time for $q = 3000 \text{ Watt/m}^2$ | 72 |
| 6.19 | T_{max} on the blade vs. time for $q = 3000 \text{ Watt/m}^2$ | 72 |
| 6.20 | Blade tip segment of a 1.5 MW wind turbine blade with 20 mm of uniform glaze ice covering the suction surface of the blade segment | 72 |
| 6.21 | A leading edge heater on a 1.5 MW blade tip segment | 73 |
| 6.22 | Ice residue on the suction surface of the blade tip segment (5-mm uniform glaze ice) for boundary condition 1 after 800 seconds. | 73 |
| 6.23 | Sunshine input heat flux boundary condition applied to the outer surface of the ice | 73 |
| 6.24 | Ice residue on the suction surface of the blade tip segment (20-mm uniform glaze ice) for boundary condition 3 representing sunshine at $-5 \text{ }^\circ\text{C}$ | 74 |
| 6.25 | Volume of ice residue at different times (20-mm uniform glaze ice) for boundary conditions 3 and 4 representing sunshine at $-5 \text{ }^\circ\text{C}$ and $-30 \text{ }^\circ\text{C}$ | 74 |

| | | |
|------|--|----|
| 7.1 | Block diagram of closed-loop de-icing simulations in ANSYS | 78 |
| 7.2 | 1-piece heater configuration with a temperature sensor at the blade tip | 80 |
| 7.3 | Input heat flux of different open-loop and closed-loop thermal controllers for a 1-piece heater | 82 |
| 7.4 | Temperature sensor output when using the proportional controllers for a 1-piece heater . . . | 82 |
| 7.5 | Comparison of T_{max_b} between a constant heat flux and a proportional control actuation for a 1-piece heater | 83 |
| 7.6 | Volume of ice/water residue between a constant heat flux and a proportional control actua- tion for a 1-piece heater | 83 |
| 7.7 | De-icing performance cost function comparison between a constant heat flux and a propor- tional control actuation for a 1-piece heater | 84 |
| 7.8 | Different views of ice temperature distribution for 1-piece heater using proportional closed- loop thermal actuation | 85 |
| 7.9 | Different views of ice/water temperature distribution for 1-piece heater using constant heat flux of $q = 763 \text{ Watt/m}^2$ | 86 |
| 7.10 | 5-piece heater configuration with installed temperature sensors | 87 |
| 7.11 | Temperature sensor outputs with no faulty sensors in the network and a proportional controller | 91 |
| 7.12 | Temperature sensor outputs with a faulty temperature sensor and proportional controller . . . | 91 |
| 7.13 | Temperature distribution of the ice and blade top surfaces at $t = 1200$ seconds for the mod- eled 5-piece heater for two scenarios of no faulty sensor and faulty sensor 5 | 92 |

Chapter 1

Introduction

In this chapter, different problems of ice formation on wind turbines and the motivation of designing an active de-icing using distributed resistive heating will be presented. Further, main contributions of this thesis will be discussed. At the end, the outline of this thesis will be presented.

1.1 Motivation

Wind energy is currently among the world's fastest growing sources of electricity production and a key source of clean energy for the future. The available energy in the wind is proportional to the cube of the wind velocity; therefore a site's generation capacity is highly reliant on wind speed [4]. With good wind resources often in cold and wet regions, installation of wind turbines in these regions has been growing faster than the total installed wind power capacity in the world. From the year 2008 to the year 2011, the global total installed capacity of wind turbines approximately doubled while the installed capacity in cold regions increased more than three times from 3 GW to more than 10 GW. Many regions of North America (Minnesota, Alaska, Canada, etc.) and Europe experience more than fifty days per year of icing conditions. In cold weather climates, icing can require turbines to be shut down for long periods of time (days to weeks) until the weather becomes warmer. Turbine life expectancy is reduced through the increased fatigue due to uneven icing, and icing presents a risk for people and properties around the turbine due to the possibility of detaching ice fragments. Wind turbine outages during icing events can lead to a loss of more than 10% annual production [11,33]. Icing increases measurement errors in wind speed and direction; further reducing turbine aerodynamic efficiency. Figure 1.1 shows the icing map of Europe for 100 m above the ground level.

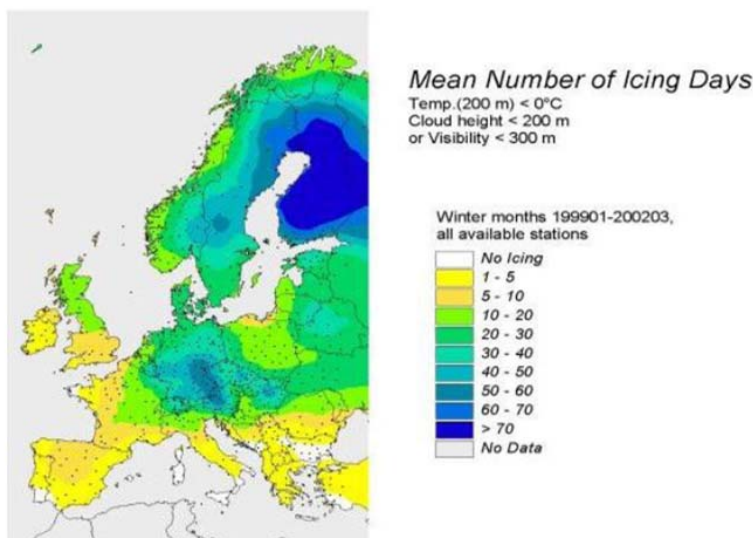


Figure 1.1: Icing map of Europe. Mean number of icing days at 100 m above ground level [50].

Due to locally varying topography, variations in icing severity and intensity may vary greatly within short distances. Therefore icing maps cannot be interpreted as exact and should be used in connection with local topographical information and with measurement data on the particular site [50]. Current indirect ice sensing techniques mainly use instruments for temperature and humidity measurement to estimate icing conditions on wind sites. Instrument ice detection is approximate and does not have the capability of accurate wind turbine blade icing. Instrument icing detection is mainly more appropriate for determination of overall ice severity and condition of a wind site. Currently in the literature, the link between instrument ice detection and turbine blade ice detection is unclear. To resolve this issue, a distributed on-the-blade optical sensing method is proposed in this thesis that provides the capability of accurate direct ice sensing that can effectively reduce the amount of total power consumption for effective de-icing on wind turbines.

Ice accumulation on wind turbine blades in cold regions decreases the power generation by 20-40%. Etemaddar et al. [12] observed different behaviors for below rated and above rated wind speeds. In below-rated wind speeds, for the 5 MW NREL reference wind turbine, power loss up to 35% was observed [12]. The thrust of the iced rotor in below rated wind speeds is smaller than the clean rotor by up to 14%, but in above rated wind speeds, it is up to 40% bigger than the clean rotor [12]. Icing also creates additional loads and mass imbalance on the blade structure which reduce the operational life of the wind turbine [21, 51].

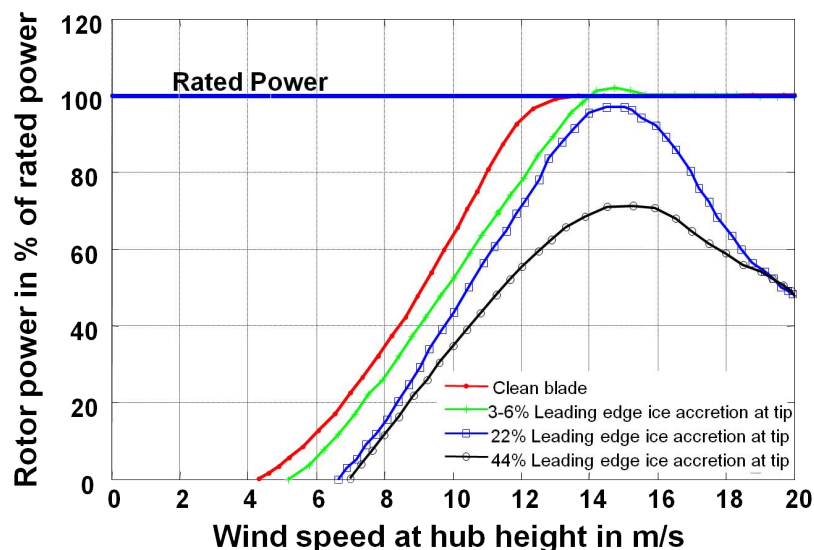


Figure 1.2: Power loss estimation due to icing at different wind speeds under different icing conditions (reproduced based upon Seifert and Richert, 1997) [52].

Many areas of Northern Europe and Northern America are affected, with the highest impact currently in Canada. At the end of 2012, Canada had 37% of the 11.5 GW of wind power capacity installed globally in moderate to severe icing climates, more than all of Europe (33%). It is forecasted that by 2017, 57% of the globally added capacity will be located in Canada in severe to moderate icing climate [60]. Seifert and Richert showed the effect of different amounts of ice accretion at the leading edge of the blade tip on aerodynamic efficiency of wind turbines [52]. Their analysis showed, for the case of severe ice accumulation, that more than 40% of the average generated power may be lost for the wind speed range of 5 to 20 m/sec for a typical 300 kW wind turbine using pitch control. This was based on different power curves calculated using the aerodynamic characteristics of the various iced sections found in wind tunnel tests and linear interpolation along the radius of the blade (Figure 1.2). This analysis can be extended for a range of turbine sizes by updating the power curve versus wind speed at hub height.

1.1.1 Types of Atmospheric Ice accumulation

There are two main types of atmospheric ice accumulation on wind turbine blades: in-cloud icing and precipitation icing [8, 13, 21, 22, 49]. In-cloud icing consists of soft rime, hard rime, and glaze ice, while



Figure 1.3: (a) Ice accumulation on the leading edge of wind turbine blades causes reduced turbine availability, and if operated, potentially damaging loading and increased public safety concerns. Photo by: Kent Larsson, ABvee (SE) from Ref. [5]; permission received from Goran Ronsten; (b) Ice accumulation may either fall off or be thrown off, causing safety issues for persons, animals, or properties that may be nearby. Photos are of 150 KW Grenchenberg turbines in Switzerland; photograph from Ref. [25]; permission received from Robert Horbaty.

precipitation icing includes freezing rain and wet snow.

In-cloud icing occurs when small, supercooled, airborne water droplets freeze upon impacting a surface. These water droplets can remain liquid in the air at temperatures down to -35°C due to their small size, purity, and lack of nucleation centers but will freeze upon striking a surface [31]. Therefore, once nucleation centers are provided such as a vibration or striking with a surface, the supercooled water quickly freezes. Different types of rime and glaze ice are formed depending on the droplet sizes and the energy balance of the surface. For small droplets with almost instantaneous freezing, soft rime forms. With medium sized droplets and slightly slower freezing, hard rime forms. If the buildup of rime is such that a layer of liquid water is present on the surface during freezing, glaze ice forms [19]. Accretions are different in size, shape, and property, depending on the number of droplets in the air (liquid water content - LWC) and their size (median volume diameter - MVD), the temperature, the wind speed, the duration of icing event, the chord length of the blade, and the collection efficiency. Rime ice forms at colder temperatures of accretion, while glaze forms at warmer temperatures [21]. Rime and glaze have different thermodynamic characteristics and therefore different required heat flux for melting. Hard rime ice is denser than soft rime and is more difficult to remove. The ability to not only detect the presence of ice, but the specific character, could enable significant energy savings by tailoring the response of a de-icing system. Variations of physical properties of ice/water (density, thermal conductivity, and specific heat) versus temperature are shown in Figure 1.5.

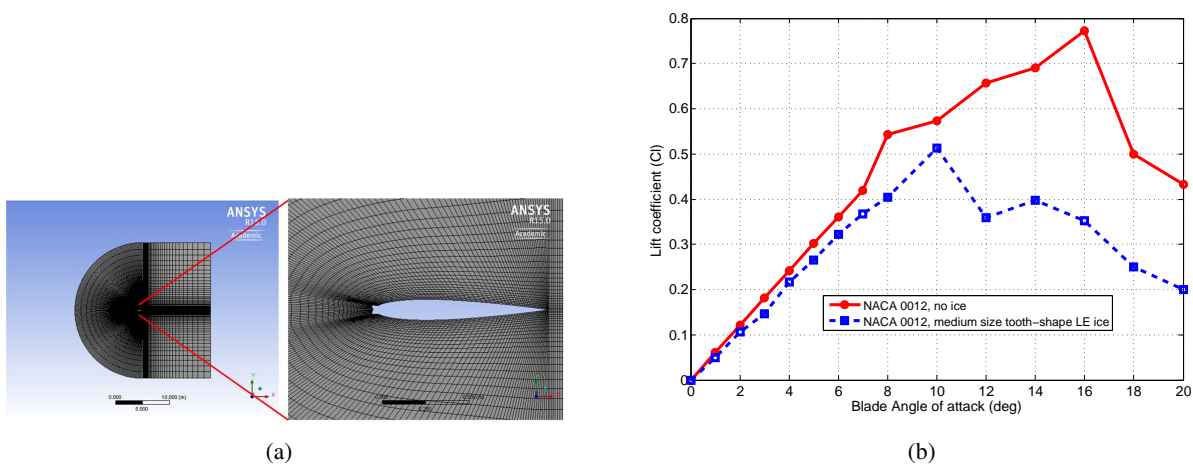


Figure 1.4: (a) Generated C-mesh around the airfoil of NACA0012 using Fluent for computational analysis. (b) Lift coefficient versus angle of attack for NACA0012 for the clean airfoil and the airfoil with a small tooth-shape leading edge (LE) ice.

1.1.2 Aerodynamic Power Degradation Due to Icing

The problem of ice formation on aerodynamic surfaces originates from the aerospace industry. Bragg and Loth conducted experimental and computational investigations for the effect of different ice shapes and locations on different airfoils with a focus on fixed wing aircraft aerodynamics [9]. Many utility and passenger airplanes use anti-freezing liquids before their flight. Today, the majority of fixed wing airplanes and helicopters must be equipped with active anti-icing or de-icing systems in order to fly under icing conditions in cold climates according to federal aviation regulations. The first de-icing method employed in the 1930s involved allowing a small amount of ice to form on a surface and then locally deforming that surface to break the ice using a pneumatically inflated rubber bladder on the leading edge of the wing [58]. Helicopters flying under icing conditions (such as search and rescue missions in polar regions) must have active de-icing systems. In 1985, piezoelectric de-icing was patented by Finke and Banks [14]. More recently, Ramanathan (2005) [45] and Palacios et. al. (2012) [41] investigated the implementation of piezoelectric de-icing on helicopter blades.

In 1952, NASA Glenn research center conducted various theoretical and experimental studies on design and development of electrothermal and hot-air anti-icing systems mainly for aerospace applica-

tions [17, 27]. National Aeronautics and Space Administration (NASA) conducted significant amount of theoretical research using Computational Fluid Mechanics (CFD) tools as well as experimental research using their wind tunnel test facilities. They investigated different airfoils under different conditions (such as temperature, humidity, liquid water content (LWC), Median Volume drop Diameter (MVD), angle of attack, free stream velocity and Reynolds number) with the main focus on aerospace applications [36]. LEWICE software was developed by NASA Glenn Research center for predicting ice shapes, collections efficiencies, and anti-icing heat requirements [37]. FENSAP-ICE developed by Newmerical Technologies [39] and TURBICE (Turbine Blade Icing Model) developed by VTT technical research center of Finland [59] are two other Navier-Stokes CFD-based commercial tools for predicting ice accretion and aerodynamic performance degradation of 3-D geometries. Reid et. al. numerically investigated the effect of aerodynamic degradation and guidelines for designing an electrothermal anti-icing system on the NREL phase VI wind turbine rotor using FENSAP-ICE [46–48].

Studying previously-developed de-icing techniques on fixed-wing airplanes and helicopters provides insight toward designing and developing future suitable de-icing methods for wind turbines. However, there are a number of fundamental differences between physics of ice accumulation and convective heat loss between fixed-wing airplanes, helicopters, and wind turbines due to different ranges of Reynolds numbers, Nusselt numbers, and turbulence characteristics. Therefore, all of the previously developed de-icing techniques for fixed-wing airplanes and helicopters are not exactly applicable to wind turbines. Qualitative comparison of different de-icing techniques will be discussed in further detail in chapter 2. In this thesis, a quantitative modeling of convective heat transfer on rotating wind turbine blades will be discussed in chapter 3.

Figure 1.3 shows examples of ice build-up accretion and some of the issues that result [5, 25]. Ice accretion on a blade mainly forms at the leading edge area and grows in different rough shapes. Seifert, Kimura, and Papadakis et al. showed different experimental ice geometries under different angles of attack and free stream velocities in 2-D [23,42,53]. Wang showed some ice accretion geometries formed in an icing wind tunnel on a small-scale rotating wind turbine blade [62]. Ice accretion reduces the aerodynamic power generation, reduces lift force, increases drag force, and expedites aerodynamic stall at much lower angles

of attack (Figure 1.4). To confirm this statement, a 2-D numerical simulation of lift coefficient is shown in ANSYS on NACA0012 airfoil for a clean and an icy scenario in Figure 1.4. A C-mesh is generated around the airfoil with higher resolution closer to the airfoil surface generated in ANSYS Fluent [3] for the computational aerodynamics analysis. Figure 1.4(b) shows the comparison of the airfoil lift coefficient versus angle of attack (AoA) for laminar flow for a clean airfoil and for when there is leading edge ice on the airfoil. It is seen that the small tooth-shape ice attached to the leading edge significantly reduces the lift coefficient at higher values of AoA. It also causes aerodynamic stall happening at lower AoA (10 deg for the icy airfoil compared to 16 deg for the clean airfoil).

There are a variety of methods that have been considered or are in use for reducing ice build-up on wind turbine blades [24, 54]. The passive solutions include hydrophobic coatings, or blades that have been sprayed with an anti-freezing chemical or painted black to maximise heat absorption. The active solutions break down to either (1) mechanical means, such as controlled blade acceleration and deceleration or piezo-electric vibration to shake off ice, or (2) thermal solutions, including heated air inside the blades or built-in electrothermal resistive heating elements [24]. Both Vestas and Siemens are currently developing thermal solutions. Siemens has collected data about the operation of wind turbines in extreme climate zones since 1994. In 2012, it offered a system for de-icing blades using a heating mat integrated into the blade. This heating mat has no wiring within the blade, but is electrically conductive and is installed close to the surface of the blade, to be switched on when necessary to melt the ice while letting the wind turbine continue operation. Siemens patented its heating mat in 2012 [24]. Vestas combines sensors, databases, and communications to operate a hot air flow unit that runs inside the blades [24].

Due to varying amounts of heat loss in different regions of a rotating blade, a more energy efficient de-icing method requires different amounts of thermal power in different blade regions, which motivates us to use distributed heating with adjustable local heat flux to reduce power consumption for de-icing [54, 56, 57]. Our thermodynamic analysis (will be discussed in chapter 3 in further detail) shows this noticeable variation of required heat flux for different locations, normally with the highest value at the leading edge of the tip of the blade. In this thesis, a distributed resistive heating system is proposed along with a distributed optical ice sensing for accurate direct detection of ice and a distributed tempera-

ture sensor network for closed-loop thermal actuation. The developed optical sensing method using Optical Frequency Domain Reflectometry (OFDR) in this research will be mainly used for direct detection of ice on a wind turbine blade. Using a distributed temperature sensor network will be proposed in parallel with optical sensing in closed-loop thermal actuation for further reduction of total de-icing energy consumption. While optical ice sensing using OFDR can mainly be used for detecting the presence and thickness of ice, using temperature sensors provide additional information of ice temperature variations before ice melting (while ice thickness is constant). This additional information of ice dynamic temperature under constant ice thickness condition can further reduce total de-icing energy consumption by decreasing the input heat flux to the thermal resistors as ice temperature increases while using only optical sensing information (ice presence and thickness) leads to a constant flux thermal actuation under constant ice thickness condition before ice melting starts. This will be discussed in further detail in chapter 7. Using distributed resistive heating thermal actuation can significantly reduce total energy consumption of de-icing on wind turbines and has minimal environmental impacts. More accurately and in general, the amount of energy consumption saving also depends on many other factors such as accurate ice location sensing on the blade, the thermal actuation strategy, geometry of ice, wind site icing conditions, wind turbine size and other operational conditions (wind speed, wind turbine blade angular speed, blade pitch angle, liquid water content (LWC), and ambient temperature) that needs to be considered for further detail analysis.

One of the main benefits of a resistive heating system over a hot-air system is the capability of distributing variable thermal energy throughout the blade with fewer modifications to the blade structure [54,56,57]. For a hot-air system, it is difficult to accurately guide hot air into the areas between the blade and the ice layer without much blade structure modification. One of the main pitfalls of the electrothermal de-icing system is applying higher thermal stresses to the blade due to direct contact of the resistors and blade structure, which needs to be considered carefully in the design. Battisti et al. describes the design of a hot-air de-icing system for a wind turbine (Ref. [6]). A more detailed comparison of different de-icing techniques can be found in Refs. [54] and [57]. In chapter 2, different existing ice sensing and thermal actuation methods on wind turbines will be discussed in more detail.

1.2 Summary of Research Goals

Nature of heat transfer for de-icing simulations using distributed heat sources on a rotating blade is very complex and happens in three-dimensions. The rate of heat transfer depends on many factors such as convection heat loss from the outer surface of the rotating blade to colder atmosphere, conduction from resistive heaters through the composite blade structure, turbulence created by air/blade structure interaction varying in time, and phase change of solid ice to water during melting. Due to these complexities, it is not possible to express the underlying physics of de-icing by means of an analytical model.

Biot number on a rotating wind turbine blade with accumulated ice is defined as $Bi = \frac{h \cdot \Delta_{ice}}{K_{ice}}$ where h is convective coefficient of heat transfer, Δ_{ice} is mean ice thickness, and K_{ice} is thermal conductivity of ice. Biot number larger than 0.1 implies that the heat convection from the blade surface relative to heat conduction throughout the blade and from the blade surface (heaters) to the ice layer has a relatively large effect and can not be neglected in de-icing analysis on a rotating blade. For a rotating wind turbine blade with medium convection ($35 < h < 50$ Watts/m².°K), and ice thickness of $1 < \Delta_{ice} < 10$ cm, and $K_{ice} = 2.3$ Watts/m².°K at -10°C, Biot number (Bi) is between 0.15 to 2.18. In addition, convection is not uniform throughout the blade (larger at the blade tip than root due to higher rotational speed) and therefore develops temperature gradients normal and parallel to the ice surface. Together with the multi-layer material (blade, ice, and water), phase change, and different boundary conditions, this complex conjugate heat transfer problem justifies the use of ANSYS for development of a 3-D computational model for distributed de-icing on the blade.

The goal of this research is to explore: development of an optical ice sensing for accurate direct detection of ice on a surface, development of a computational framework for simulating 3-D closed-loop distributed de-icing using temperature and optical sensing, and optimization of an active de-icing technique using distributed resistive heating to reduce de-icing energy consumption, de-icing time, volume of high-temperature regions, and maximum applied temperature on the blade structure.

To our knowledge, high fidelity computational analysis of variable heat flux through closed-loop control on wind turbines has not been previously discussed in the literature. In this dissertation, development of experimental and computational frameworks of closed-loop de-icing will be discussed using resistive

heating and temperature/optical sensing. Validation of developed computational framework with the experiments for a stationary blade segment will be discussed in chapter 5. Further in chapter 7, development of a script-based controller module in ANSYS will be discussed which interacts in real time with the finite element solver. At each time step, the finite element solver provides the solution of ice melting and the temperature distribution on the blade. Then, the controller updates the value of input thermal flux to heaters as a function of temperatures at specific locations on the blade structure which represent temperature sensors. This developed framework provides a general capability of closed-loop de-icing simulation based on finite element solution of heat transfer equations on an icy blade for advanced cases including a large number of distributed resistive heaters and temperature sensors and different complex ice geometries. This methodology can also be used for computational analysis of closed-loop de-icing of aerial vehicles and for optimization of thermal actuation given a particular type of controller. This thesis will investigate the computational results of a lower intensity proportional controller and a higher intensity pulsed proportional controller with direct on-the blade temperature sensing on a segment of a 1.5 MW wind turbine blade. De-icing performance of these closed-loop controllers will be compared with open-loop constant heat flux actuation. Furthermore, de-icing results for a 5-piece heater configuration and distributed temperature sensing for a proportional controller will be shown. Different surrogate modeling approaches will be used to perform optimization to find the best values for the controller parameters.

1.3 Thesis Contributions

In this dissertation, the experimental feasibility of a new active de-icing approach is demonstrated using distributed heaters, optical sensors for direct detection of ice on the blade, and distributed temperature sensors for closed-loop control. The proposed approach reduces total amount of energy consumption for de-icing with more effective ice-melting on the blade. An experimental setup was fabricated for closed-loop de-icing on a stationary blade segment using distributed heaters, optical sensors and temperature sensors. All of the subcomponents of the experimental setup in this thesis were designed and fabricated including an icing chamber, required electronic circuits for signal amplification, required signal processing codes for optical ice sensing, and closed-loop control software. The experimental results of de-icing are validated for

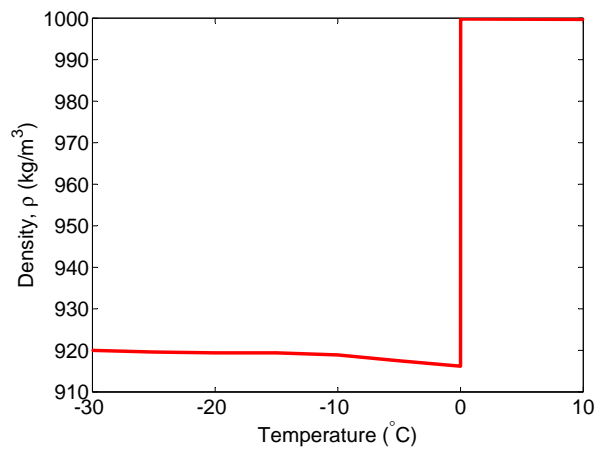
a Proportional, Integral, and Derivative (PID) controller with computational simulations of ice melting in ANSYS.

In addition, a computational framework is developed for implementation of closed-loop active de-icing using distributed resistive heating and temperature sensing. A script-base module is developed in ANSYS which provides the capability of (1) closed-loop de-icing simulations for a distributed network of sensors and actuators, (2) investigating different closed-loop thermal control schemes and their de-icing efficiency (3) optimizing of the controller parameters for each heater in a distributed network to provide more effective de-icing, (4) analyzing different known faulty sensors and thermal actuators in the network. It will be shown that closed-loop control provides much faster de-icing than an open-loop constant heat flux thermal actuation strategy with the same average heat flux. High intensity pulsed thermal actuation slightly improves ice melting but relatively increases the amount of applied thermal stress to the blade structure. The developed computational methodology in this thesis can be used to investigate more advanced closed-loop controller schemes aiming to find a global optimal actuation strategy for de-icing, optimal location of the sensors and thermal actuators in a distributed network. This methodology can also be used for analysis of different complex ice dynamics and geometries on a rotating wind turbine blade under different operational conditions such as Reynolds number, Nusselt number, and blade local angle of attack.

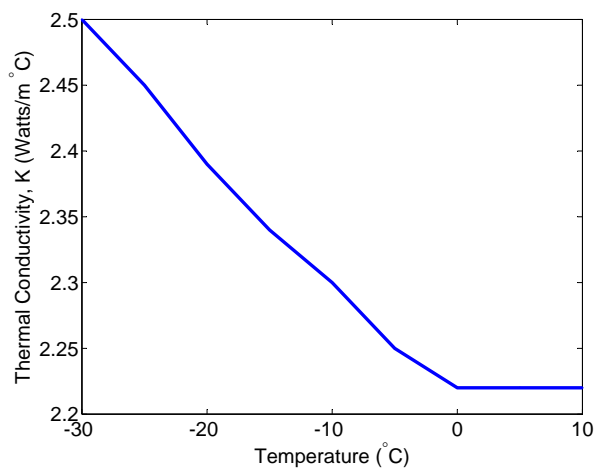
1.4 Thesis Outline

In chapter 2, background information is described on existing ice sensing methods. Further, an optical technique is proposed for direct ice sensing and experimental results are described. The developed optical sensing method in this thesis allows direct and local detection of ice on the blade and thus provides a suitable test bed for localized active de-icing. In the second part of this chapter, background information of current thermal actuation techniques is discussed and their effectiveness is compared for active de-icing of wind turbines. Furthermore, a method of thermal actuation is proposed using distributed resistive heating. In chapter 3, calculations of heat flux requirements are presented for de-icing on a wind turbine blade. In chapter 4, calculations of de-icing economical profitability are introduced based on wind site conditions and wind turbine size. In chapter 5, the components of the experimental setup will be described including a fabricated

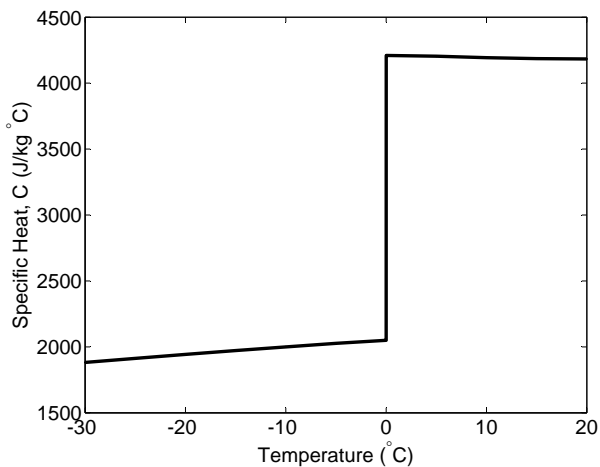
custom icing chamber, distributed optical ice/temperature sensors, thermal actuators, and data acquisition hardware as well as a developed closed-loop control scheme for experiments of de-icing. A computational model for evaluating distributed heating is later explained in this chapter. In chapter 5, closed-loop experimental results of active de-icing are presented including comparing the performance of continuous Proportional, Integral, and Derivative (PID) control with high-intensity pulsed actuation. In chapter 6, the de-icing efficiency of different heater layouts are computationally investigated under the assumption of constant heat flux for a small-scale blade segment (used in the experiments) and a larger blade segment of a 1.5 MW wind turbine. In chapter 7, a computational framework is developed for closed-loop controller design for de-icing using distributed resistive heaters and temperature sensors. This computational framework provides the capability of investigating different closed-loop controller schemes for distributed de-icing which can ultimately lead to actuation optimization in a distributed network of resistive heaters and sensors. In addition, the developed module in ANSYS provides the capability of analyzing de-icing performance under known faulty sensors or actuators in a distributed network. At the end, in chapter 8, main conclusions, contributions of this thesis, the directions of future work and recommendations on active de-icing of wind turbines will be summarized. Appendix A includes all of the notations used in this thesis. Appendix B includes all of the developed codes and modules in ANSYS-APDL software for computational simulations of closed-loop de-icing and the calculation of different terms inside de-icing performance cost function including volume of ice residue at different blade regions, volume of high-temperature regions on the blade due to thermal actuation, and maximum applied temperature to the blade structure during de-icing.



(a)



(b)



(c)

Figure 1.5: Physical properties of ice/water versus temperature. (a) density versus temperature variation. (b) thermal conductivity versus temperature variation. (c) specific heat versus temperature variation.

Chapter 2

Ice Sensing and Thermal Actuation: Existing and Proposed Methods

In this chapter, different methods of ice sensing and thermal actuation for de-icing in the literature are discussed and the pros and cons of different strategies will be summarized. Further, an optical sensing method is proposed for accurate direct detection of ice and experimental results will be presented.

2.1 Ice Sensing

2.1.1 Background Information

There are two different types of ice detection: indirect and direct. Typical methods for detecting ice in current wind turbine systems are indirect (passive) sensing. They use weather stations on the tower or nacelle of the turbine. Humidity and temperature measurements are combined with measured wind speeds to determine whether icing is likely to occur [29]. Another example of indirect ice sensing is monitoring the power output during the wind turbine operation to detect an icing event. However, on many occasions, indirect ice sensing methods are neither accurate nor have enough spatial resolution for active de-icing [43]. Furthermore, icing is most likely to occur on the far reach leading edges of the blades themselves, not on the tower, leading to inaccuracies when trying to correlate the weather station data on the tower or nacelle to the active portions of the blade. Wind velocity is another factor which affects ice formation and accumulation on the blade which is not taken into account in most existing indirect ice detection methods.

Direct ice sensing methods are more accurate for detection of ice on the blade with better spatial resolution. Indirect sensing methods are not capable of accurately predicting the location of ice formation which lead to high amount of de-icing energy consumption due to heating up a large area on the blade.

Combined Optical Ice/Temperature Sensors and Electro-thermal Resistors are Embedded on the Blades

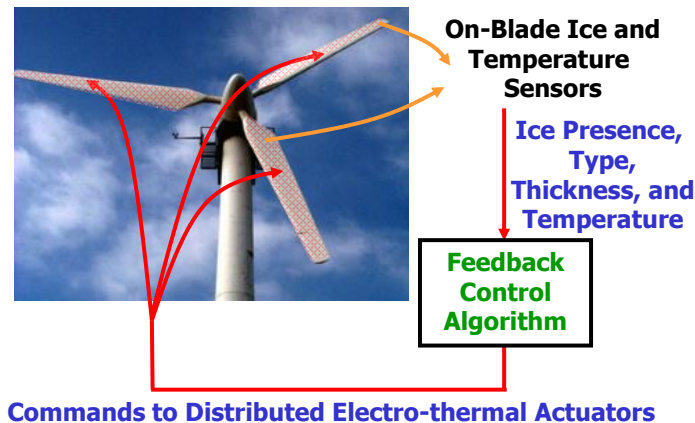


Figure 2.1: Schematic diagram showing thermal control system using direct optical sensing, temperature sensing and resistive heaters.

Some examples of direct ice sensing methods are resistance, impedance, and capacitance based methods, as well as optical techniques. In Ref. [19], capacitance, inductance, and impedance sensing are introduced as effective on-blade ice sensing methods for wind turbines. These sensors can detect ice formation within a localized area, and their thin sensing elements/electrodes can conform to blade surfaces [16, 19]. More information on these methods are available in [43] and [57].

In section 2.1.2, experimental results of the proposed optical ice sensing method for direct detection of ice existence, type and thickness is explained. Then, a de-icing method is demonstrated in chapter 5 using combined on-the-blade optical/temperature sensors and electro-thermal actuation, as shown in Figure 2.1.

2.1.2 Proposed Direct Optical Ice Sensing

Ice removal technology coupled with an early detection of ice formation on the blade for reducing aerodynamic degradation (shown in Figure 1.2) appears to be an essential feature for future generations of wind turbines in cold climates. There are currently no widely available and sufficiently reliable ice detection systems suitable for wind turbines [19, 61]. Indirect ice sensing methods do not have enough spatial resolution and accuracy for active localized de-icing. There are not yet implementations to directly

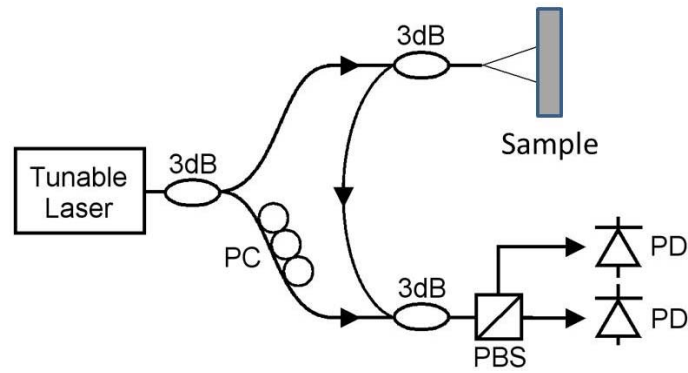


Figure 2.2: Layout of an optical frequency-domain reflectometer [34]. Light from the tunable laser is reflected from the sample and interfered with a reference arm. As the frequency of the laser is swept, interference fringes are detected that indicate the amplitude and round-trip delay of reflections from the sample. 3db = 50/50 fiber coupler, PC = polarization controller, PBS = polarization beam splitter, PD = photodiode.

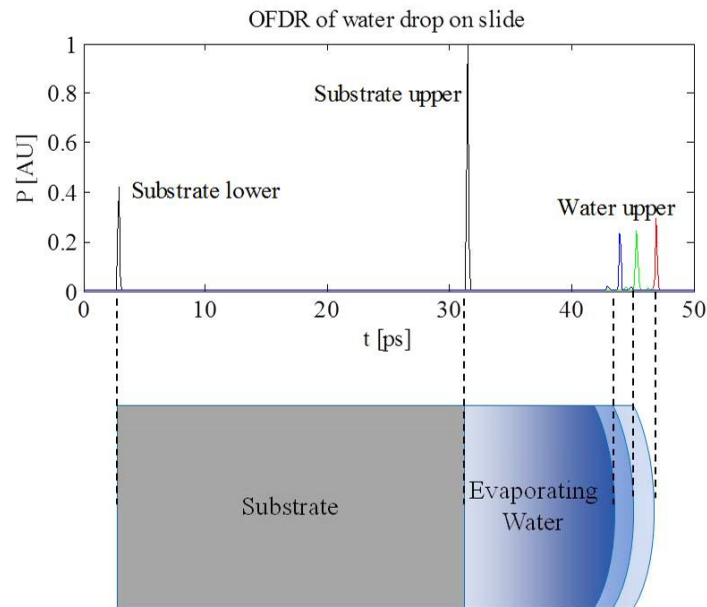


Figure 2.3: Optical frequency domain reflectometry of a variable thickness water layer deposited on a substrate. The water layer, which was allowed to evaporate over the course of approximately one hour, was measured at three times to have thickness 2.32, 2.08 and 1.86 mm with a transform-limited precision of 0.036 mm. The vertical axis is the amplitude of reflection. On the horizontal axis, 1 ps corresponds to a round-trip travel time for the laser in 112.5 μm of water [57].

measure the presence and type of ice accurately on the blade. Direct detection of ice on the blade, as opposed to estimating ice accumulation on the blades using sensors on the nacelle, provides a more robust method for

implementing thermal control for de-icing. This highlights the need for improved sensing methodologies.

In this section, experimental feasibility of a proposed direct on-the-blade optical sensing and distributed resistive heating will be explained with the goal of reducing the total power consumption of de-icing. At the end of this section, experimental results of ice existence, ice types, and ice thickness will be presented.

A newly developed optical sensing technique is applied to enable detecting early stages of ice formation, including both the type of ice and the thickness (to within 36 microns). Direct ice detection requires measurement of the region just outside the blade surface. To accomplish this thickness measurement, optical signals directed normal to the surface reflect from the upper surface of the ice to reveal its presence, thickness, and type. Thickness could be measured by time of flight of a short pulse, referred to as Time-Domain Reflectometry (TDR). TDR requires optical pulse length of $dt \leq \frac{dx}{c}$ where dx is the desired thickness resolution and c is the speed of light. For our optical ice sensing application, pulse lengths of approximately 100 femtosecond duration are required which are costly to generate and tend to disperse rapidly in solids. Conversely, optical frequency-domain reflectometry (OFDR), as shown in Figure 2.2, uses continuous laser light with a swept frequency which is easier to generate and can be directed through optical fiber [20, 34]. Fiber coupled sources allow for many sensors to be multiplexed on a single fiber running down the full length of the blade, greatly reducing complexity. Additionally, recent advances in all-fiber, rapidly-tuning laser sources [20] promise to reduce the cost and delicacy of the lasers while increasing the measurement speed. OFDR can measure multiple simultaneous returns in different time windows [15, 57]. The optical signal to each sensor is thus delayed by a unique delay such that the entire array can be measured in a single interrogation.

Moore and McLeod showed the use of phase information in the OFDR to simultaneously measure thickness to ± 61 nm precision and the index of refraction to $\pm 2 \times 10^{-6}$ [34]. Since variations in the ice type are reflected in their refractive index, this suggests that both type and thickness of ice can be detected.

To demonstrate the efficacy of OFDR for the detection of icing on a blade surface, the instrument whose schematic is shown in Figure 2.2 is used to monitor the thickness of an evaporating water film on a solid substrate, as shown in Figure 2.3. Gradient-index (GRIN) lenses with an anti-reflective coating are used as optical ice sensors in this research. The sensor area must be sufficiently large to average over ice

crystal size, entrapped air, and other spatial variations. The 10 μm diameter of a fiber core is thus too small and will not return a repeatable signal. Thus we employed a fiber collimator. The collimating lens has a circular detection diameter of 3 mm. The transform-limited time resolution of the measurement is $d\tau = 1/d\nu = 121$ fs which corresponds to a spatial resolution of 36 μm in air. As shown in Figure 2.3, top, the system can easily distinguish both the presence and thickness of the material on the surface.

Figure 2.4 presents experimental optical sensing results, demonstrating that the sensor can distinguish between air, water, glaze ice, and rime ice on the blade. For the case of air, the measured signal is symmetric with a small peak due to the existence of the anti-reflective coating (Figure 2.4a). In this case, there is no volume scatter and the peak of the signal corresponds to the airfoil-air boundary. For the case of liquid water, two smooth peaks are captured with no volume scatter (Figure 2.4b). For the case of glaze ice (Figure 2.4c), a smooth peak is captured followed by a small scattered signal. The first peak corresponds to the airfoil/ice boundary, and the small scattered signal corresponds to the rough ice/air interface. Rime ice (Figure 2.4d) has a highly non-symmetric shape and distinctive volume scatter due to the increased air volume within the ice and irregular shape of the ice crystals. These signals can be recognized and categorized in signal processing to identify type and thickness. The peak magnitudes and corresponding times where these peaks occur are numerically calculated. A magnitude filter is applied to reject noise while being able to capture the volume scatter due to rime ice. Different Matlab codes are developed that look at the number of captured peaks, peak magnitudes, magnitude of time integral of the signals and symmetrical/asymmetrical shape of the signals around their peaks in order to detect the type of ice. Time-of-flight is multiplied by the speed of light to translate to a distance measurement (optical path length). Optical path length is calculated as refractive index multiplied by path length.

In summary, demonstrated optical method in this thesis is capable of direct detection of ice existence, classification of ice type, and ice thickness measurement with 36 micrometer resolution. The ice sensors using OFDR are responsive (0.5 Hz response time) and accurate in measuring ice thickness (micrometer thickness resolution) and hence are able to detect ice in the very early stages of ice formation. In section 2.2, a background information of different Anti/De-icing actuation techniques will be provided and a performance comparison will be summarized at the end of this chapter.

2.2 Ice Mitigation

De-icing and anti-icing methods in the literature can be divided into active and passive methods. In the remainder of this section, these methods are explained. Further, different active de-icing techniques will be summarized at the end of this section.

2.2.1 Passive Ice Prevention

Passive ice prevention methods are applied before operations of a wind turbines/aircraft. In passive techniques, usually there is no sensing system involved and the entire process is normally applied manually such as covering a surface with ice-repellant coating or spraying anti-freezing liquids on the surface before the operation starts. Currently, wind turbines installed in cold regions use passive methods such as ice repellent (ice-phobic) coatings on the blades. However, these coatings are only effective for short-term operations in slight icing conditions and are not effective in harsh cold conditions with varying forms of ice. As an example, silicon paints exhibit promising ice repellent characteristics on soft rime under slight icing conditions; however, hard rime ice exhibits greater adhesion strength to silicon paint than an uncoated surface. In addition, these passive ice prevention techniques have been shown to have poor durability when tested on wind turbines [35, 61].

2.2.2 Active Thermal Actuation

Active de-icing methods are applied during the operation of a wind turbine/aircraft. Active de-icing can be implemented either through open-loop or closed loop actuation. In closed-loop active de-icing, an ice sensing is used in the loop. Then a thermal actuation command at each time-step is generated based on the output of the sensing system to mitigate turbine down time. Open-loop and closed-loop thermal actuation using distributed resistive heating will be discussed in further detail in chapters 6 and 7, respectively.

Active de-icing systems are more effective for ice prevention under medium to severe icing conditions when used with a reliable and accurate ice detection sensing system. However, the design, operational and maintenance costs of such a system are likely to be much higher which is beyond the scope of this thesis.

However, a profitability analysis of different active thermal de-icing techniques will be discussed in chapter 4 from energy consumption perspective based on the published data in the literature.

Table 2.1 shows a comparison of different active de-icing methods on wind turbines based on the limited technical data available in the literature. Among all of the mentioned active de-icing techniques, only thermal resistors and hot air techniques have been tested on wind turbines in cold climates with available commercial kits. Both hot air injection and resistive heaters can consume more than 10% of the generated power [6,43]. Figure 2.5 shows a summary of different approaches to ice sensing and anti-icing/de-icing [16, 43,57] including the proposed optical sensing technique.

2.2.3 Proposed Distributed Thermal Actuation

In this dissertation, a distributed resistive heating technique is proposed for active de-icing with the capability of local thermal flux adjustment. The main motivation of this technique is described in further detail in chapter 3. Experimental and computational results of de-icing using distributed resistive heating on a rotating wind turbine blade will be presented in chapters 5 to 7. The computational results discussed in this thesis only focus on ice melting before ice shedding. Full computational analysis of ice shedding can be very complex itself and is not the focus of this research.

Estimated cost of equipments including optical sensors, temperature sensors, laser source, optical fibers, and power electronic hardware for a 5 MW wind turbine will be explained in section 4.3.

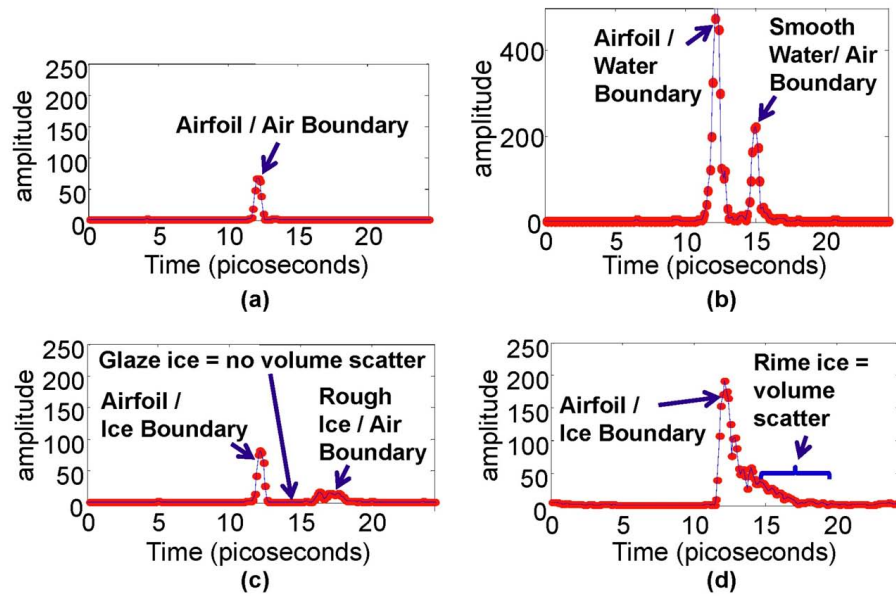


Figure 2.4: OFDR measurements yield distinct signals for different conditions: (a) No water/ice on the blade. (b) Liquid water on the blade. (c) Glaze ice on the blade. (d) Rime ice on the blade. Y-axis is arbitrary scale proportional to the amplitude of the reflected optical electric field. X-axis is round-trip optical time of flight from the fiber exit to the particular layer. 1 ps corresponds to a round-trip travel time for the laser in $112.5 \mu\text{m}$ of water [57]. For ice thickness calculation, the same index of refraction is assumed for ice and water.

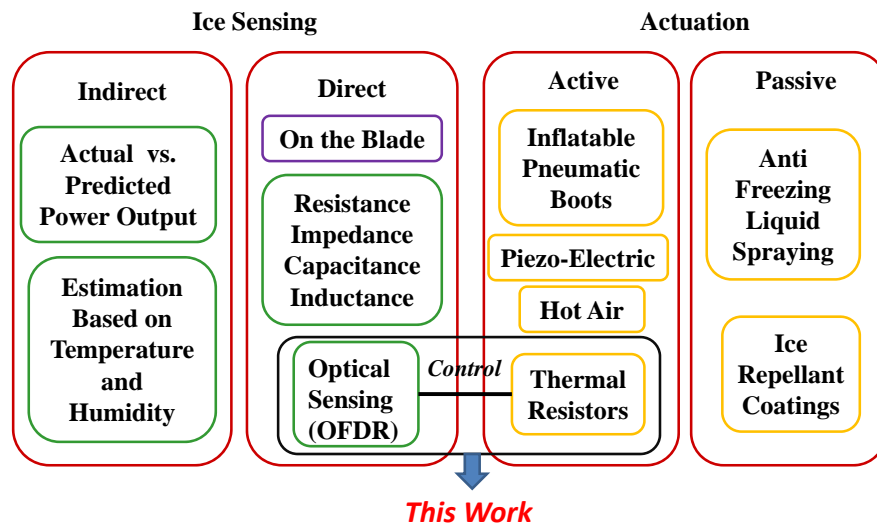


Figure 2.5: Summary of different approaches to ice sensing and anti-icing/de-icing [6, 43, 54, 57]. Among all of the direct ice sensing methods to date, the proposed optical ice sensing method in this thesis provides the most complete information (ice existence, type, and thickness) for local de-icing.

Table 2.1: Comparison of different methods for active de-icing of wind turbines [6, 43, 54, 57]

| Performance Categories | Active De-icing Method | | | | |
|--|--|--|---|---|--|
| | Thermal resistors | Hot air | Inflatable pneumatic boots | Liquid surface coatings | Microwave |
| Energy consumption (1 for smallest and 5 for highest) | 4 | 5 | 2 | 3 | 1 |
| Effect on aerodynamic efficiency of the turbine | (Good) Does not create negative aerodynamic effect on the blades | (Medium) Hot air layer under the ice does not create negative effects. Blowing external hot air may degrade aerodynamic efficiency. | (Poor) Temporarily disrupts the flow when actuating and therefore decreases aerodynamic efficiency | (Medium) Might slightly degrade the aerodynamic efficiency | (Good) Does not create negative aerodynamic effect on the blades |
| Operating cost | Moderate | Moderate | Moderate | High | Low |
| Maintenance cost | Moderate | Moderate | Moderate | High due to frequent clogging of membrane holes | Not known |
| Negatively affected by centrifugal force during blade rotation | No | No | Yes (inflates itself) | Yes (is quickly removed) | No |
| Environmentally harmful | No | No | No | Yes | yes |
| Noise creation | Low | Low | High | Low | Low |
| Effective for different types of icing | Effective from light to severe icing conditions | Effective from light to severe icing conditions | Effective from light to severe icing conditions | Only effective from light to moderate icing conditions | Only effective for light icing conditions |
| Capability of distributing thermal energy "optimally" from hub to tip of the blade | Moderate (depending on the number of resistors and distances between them) | Low (difficult to optimally control external hot air flow over the blade from hub to tip) | Low | Low | Not known |
| Modification of the blade | Few | Few | Much | Few | Few |
| Ice prevention durability | Long | Long | Long | Short | Not known |
| Successfully tested on wind turbines | Yes | Yes | No | No | Concept has been proven, no successful wind turbine application to our knowledge |
| Commercial kit for wind turbines | Available | Available | Not available to our knowledge | Not available | Not available |
| Advantages | Energy distribution, implementation, minimal blade modification | Direct deflection of cold water droplets | Fast reaction time for de-icing | Minimal system complexity | Very low thermal power |
| Disadvantages | Higher local thermal stress due to direct contact of resistors and blade structure | Poor optimal distribution of thermal energy | High noise, possible self inflation due to centrifugal force | Short durability, quickly removed by centrifugal force | Not effective for moderate and severe icing conditions |
| Current overall commercial ranking for wind turbines | 1 | 2 | 3 | 4 | 5 |

Chapter 3

Blade Thermodynamics

Development of an aero/thermodynamic model for wind turbines is an essential step before designing an active de-icing system. Different amounts of heat loss happen in various locations of a wind turbine blade due to many factors including blade rotation, variation of the blade pitch angle, variation of ambient temperature, wind speed, wind direction, and non-uniform ice accumulation. In this chapter, first an empirical blade thermodynamic model is explained based on previous experimental data in the literature [62] for better understanding of the nature of convective heat transfer on a rotating wind turbine blade. This thermodynamic model predicts the required amount of heat flux for de-icing as a function of blade size, wind speed, wind direction, and atmospheric conditions. Then, we discuss the variation of required convective heat flux for de-icing for different wind speeds, directions, blade pitch angles and other atmospheric conditions. At the end of this chapter, we explain the total required heating including sensible and convective heating on a rotating blade.

3.1 Calculation of Heat Flux Requirement for De-icing

Different areas on wind turbine blades need significantly different levels of thermal power and flux for de-icing. Thus, optimally distributing the required thermal energy across the blade can save a significant amount of energy in de-icing systems. The highest heat flux required is at the tip section of the blade. As such, a preliminary step in designing a suitable thermal actuation method for de-icing is calculating the heat flux requirement for this most critical region of the blade. This will be explained in further details in section 3.2.

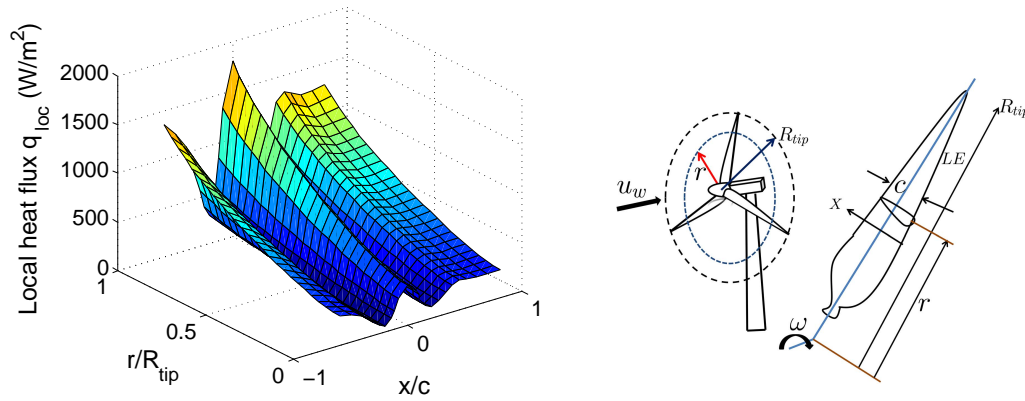


Figure 3.1: Simulated heat flux required (due to convection loss) for a rotating blade with a NACA 63421 airfoil in a uniform wind field versus non-dimensional chord position x/c (negative values are for the pressure side and positive values are for the suction side of the blade) and non-dimensional span-wise radius (distance from hub) r/R_{tip} [56, 57]. The heat flux plotted is the amount needed from a de-icing system to compensate for convection loss from the blade; $T_{amb} = -30\text{ }^{\circ}\text{C}$, $\omega = 20\text{ RPM}$, $u_w = 12\text{ m/s}$, $R_{tip} = 25\text{ m}$, $AoA = 0$, $Pr = 0.7211$, $P = 500\text{ KW}$, where T_{amb} is the ambient temperature, ω is the angular velocity of the blade, u_w is the wind speed, R_{tip} is the span-wise radius at the blade tip, AoA is angle of attack, and P is the wind turbine rated power.

Figure 3.1 shows the calculated heat flux requirement (due to convection loss) versus non-dimensional chord position x/c and non-dimensional span-wise radius r/R_{tip} at a given atmospheric condition. The required parameters are angle of attack AoA of the blade, blade geometry, angular velocity ω of the blade, and wind speed u_w . Figure 3.1 shows the characteristics and behavior of the convection loss for laminar flow over a 500 KW wind turbine blade rotating with a constant angular velocity and a uniform wind field at zero AoA . Negative values of x/c are for the lower blade surface, positive values of x/c are for the upper blade surface, and $x/c = 0$ is leading edge of the blade. The peak value of heat flux at the leading edge of the blade tip for this simulation is about 1800 Watt/m² for a 500 KW wind turbine. This calculation uses experimental local values of Nusselt numbers at different Reynolds numbers and Prandtl numbers for a NACA 63421 airfoil using experimental convective heat correlations [62]. This airfoil has a non-symmetrical profile which creates different trends below and above the stagnation point for Nusselt numbers and the convective heat transfer coefficient [62].

The convective coefficient of heat transfer (h) at each point is calculated as

$$h = \frac{Nu_x k_{air}}{c} \quad (3.1)$$

where Nu_x is the local Nusselt number on the airfoil, k_{air} is the thermal conductivity of air, and c is the chord length of the blade.

The convective loss heat flux (q_{conv}) is calculated as

$$q_{conv} = h(T_0 - T_{amb}) \quad (3.2)$$

where T_0 is the desired outer blade surface temperature and T_{amb} is the ambient temperature.

Figure 3.1 shows the noticeable variation of required heat power for different locations (2000 Watt/m² average flux at the blade tip versus approximately 500 Watt/m² at the blade hub) for the analyzed 500 KW wind turbine, with the highest value at the leading edge of the tip of the blade. These calculations show that heating the entire blade using this locally adjusted heat flux consumes approximately 7-10% of the rated power of the wind turbine [57]. Equally heating the entire blade, such as using a hot air technique, consumes even more power (about 15% of the rated power) as reported in Refs. [6] and [26].

3.2 Variation of Convective Heat Flux for Different Wind Turbine Operating Conditions

Wang showed the experimental results of the variation of average Nusselt number \bar{Nu} as well as local Nusselt number Nu_x around NACA 63241 airfoil for a rotating wind turbine blade at different blade angle of attacks AoA , local Reynolds number Re_c , and Prandtl number Pr [62]:

$$\bar{Nu} = 0.0943(0.75 + 0.017\alpha)(Re_c)^{0.636}Pr^{\frac{1}{3}} \text{ for } Re_c > 5 \times 10^5 \quad (3.3)$$

$$\bar{Nu} = 2.483(0.75 + 0.013\alpha)(Re_c)^{0.389}Pr^{\frac{1}{3}} \text{ for } Re_c \leq 5 \times 10^5 \quad (3.4)$$

Local Reynolds number at each element on the blade is calculated as:

$$Re_c = \frac{\rho u_{rel} c}{\mu} \quad (3.5)$$

where ρ is air density, c is the blade chord length at each cross section, u_{rel} is relative wind velocity at each blade cross section, and μ is dynamic viscosity of air. u_{rel} is calculated as:

$$u_{rel} = u_w^2 + u_r^2 \quad (3.6)$$

where $u_r = r \cdot \omega$ is radial velocity of the blade section.

Local blade angle of attack α is calculated as:

$$\alpha = \arctan\left(\frac{u_w}{u_r}\right). \quad (3.7)$$

In the simulation result shown in Figure 3.1, average Nusselt number \bar{Nu} across each blade section was calculated based on equations 3.3 and local Nusselt number Nu_x was calculated based on the experimental results discussed in [62] as a function of Re_c and Pr . Then, convective coefficient of heat transfer h was calculated based on equation 3.1 and required convective heat flux at different locations of the blade was calculated based on equation 3.2. If the geometry of the wind turbine blade changes, values of local Nusselt number Nu_x need to be updated for the new geometry. To calculate required convective heat flux at a different blade pitch angle, equations 3.3 can be used for each blade cross section along the blade span.

The total convective thermal power P_{conv} required for de-icing for each blade using distributed heat flux can be calculated as:

$$P_{conv} = \int_A q_{conv} dA \quad (3.8)$$

where A is the total outer surface of the blade exposed to convection with q_{conv} calculated using equation 3.2. Using the calculated convective heat flux q_{conv} shown in Figure 3.1 and equation 3.8 for the calculation of convective heat flux P_{conv} shows that only 0.95% of the rated power is required for compensation of convective heat loss on each blade of the modeled 500 KW wind turbine. This leads to approximately using less than 3% of the rated power for de-icing to compensate convection loss for a three-bladed 500 KW wind turbine. This calculation shows that using a distributed resistive heating thermal actuation with the capability of accurate local thermal control can significantly save energy consumption for de-icing compared to non-localized thermal actuation techniques such as hot-air.

The thermodynamic behavior of convection loss changes once the flow becomes turbulent over the blade. This was investigated in [30] where it was shown that the effect of a transition to turbulent flow at the leading edge is to increase the required heat transfer by an average factor of 2.5. Therefore, laminar and

turbulent flow conditions need to be detected throughout the blade for different turbine operating conditions for active de-icing.

3.3 Total Required Heat Flux for De-icing

Conduction, convection, evaporation, and radiation are sources of heat loss from the blades. Among these different types of losses, convection results in the most heat loss; and in most cases the other losses can be neglected. For de-icing systems, we need to provide enough thermal energy to compensate for these heat losses, sufficient heat for increasing the solid ice temperature from below zero up to the melting temperature (sensible heat) and also the required thermal energy to cause the phase change of a relatively thin layer of accumulated ice on the blade from solid to liquid (latent heat).

A de-icing system must provide enough thermal energy to compensate for convection heat loss, sensible heat to increase the initial temperature of ice to its melting temperature, and latent heat for the phase change from solid ice to liquid water. The latent heat flux required for the phase change of ice is dominant compared to the sensible heat flux even when the initial ice temperature is significantly below zero. Calculations show that for ice with an initial temperature of $-30\text{ }^{\circ}\text{C}$, the amount of heat required to change its temperature to zero degree Celsius is only 18% of the heat required for the phase change. Since the phase change of ice requires much higher thermal flux than sensible heat flux, it is not profitable to melt the entire ice layer formed on the blade. Thus, one strategy for reducing thermal energy expenditure is to only melt a thin layer of ice and then shed off the remaining ice by using centrifugal force from the blade rotation [6].

Figure 3.2 shows a plot of the summation of sensible and latent heat flux of ice required for de-icing versus melting time for a 1-mm soft rime ice at two different initial ice temperatures. It is seen that this heat flux decreases as melting time increases. Power decreases proportional to $\frac{1}{t}$, in other words the total energy requirement is approximately conserved, as expected. Assuming thermal resistive heating with a maximum heat flux generation capability of 2000 Watt/m^2 (approximately 500 Watt/m^2 for the summation of latent and sensible heat fluxes and 1500 Watt/m^2 to compensate for the convection loss at the leading edge), this calculation shows that 7-8 minutes is a reasonable melting time for a 500 KW wind turbine.

It is shown in Figure 3.1 that the required heat flux for de-icing significantly decreases from the blade

tip to the blade root. Experimental data is reported in the literature on the required heat flux for de-icing at different blade regions, as tested by VTT (The Technical Research Center of Finland) and Kemijoki Ltd. in 1993. They tested a de-icing system using a thermal resistor on a 450 KW turbine in extreme conditions in Finnish Lapland in order to keep the rotors free of ice. This is the world's first documented test of a heat-based de-icing system for commercial wind turbines [28, 61]. The data shows de-icing power consumption of 5% of the 450 KW turbine's rated power with peak heating power of 4500 W/m^2 at the blade tip versus 350 Watt/m^2 at the blade root (13/1 ratio). Heating elements covered only a maximum of 15 cm from the leading edge. Heating power was sufficient in most cases to keep off rime ice in the winter; however, this system was unable to prevent icing in the (rare) cases of freezing rain.

In summary, the thermodynamic analysis presented in this chapter shows the benefits of active distributed de-icing with local heat flux control in different regions over other non-localized de-icing strategies. Localized distributed active de-icing can also be used in parallel with a passive hydrophobic coating to even further reduce energy consumption of de-icing. Direct ice sensing, blade temperature sensing, and distributed thermal actuation has not yet been tested on wind turbines. In the following chapters of this thesis, the development of our experimental and computational frameworks will be explained for active de-icing using distributed resistive heating and sensing.

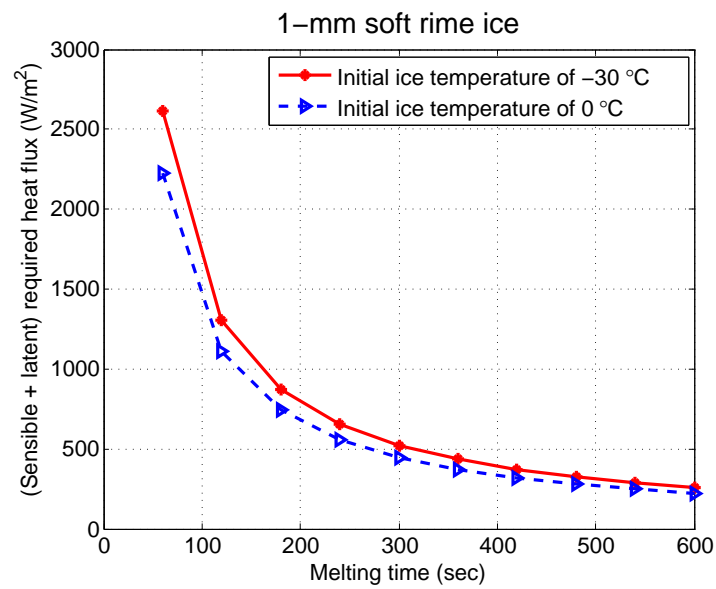


Figure 3.2: Total (sensible + latent) heat flux vs. melting time for a 1-mm soft rime ice layer ($\rho = 400 \text{ kg/m}^3$) at different initial ice temperatures on a non-rotating rectangular shape surface with no convection. Codes for detail calculations are in Appendix A.

Chapter 4

De-icing Profitability Analysis

The effectiveness of an Anti/De-Icing System (ADIS) can be evaluated by an analysis of system profitability as judged by the net energy production relative to an unprotected system. In this chapter, the profitability calculations are presented using a de-icing system in terms of net energy production for different sizes of wind turbines (200 KW to 5 MW), using either electro-thermal resistors or hot air systems. The assumption here is that there is no downtime on the wind turbine operation due to icing. As such, this calculation establishes a lower bound (worst case) of the profitability of utilizing de-icing systems since in reality wind turbine net energy is zero during the wind turbine downtime.

Using Seifert and Richert results (Figure 1.2), the average aerodynamic power loss ratio is obtained due to icing ($\eta_{P_{ice}}$) for a wind speed range of 5-20 m/s. Table 4.1 shows the ratios of power consumption of each de-icing heating system (electrical resistors and hot air) to the nominal output power for different size wind turbines from simulations [7, 26]. After interpolating for different P_{out} values, these ratios are used in ADIS energy profitability calculations in this chapter.

Table 4.1: Average values for the ratio of power consumed by ADIS to the nominal power of the wind turbine for two different types of ADIS systems [7, 26]

| Ratio of power consumed by de-icing system to the average power produced by the wind turbine ($N_{P_{heat}} = \dot{Q}_t/P_{out}$) | | |
|---|---------------------------------|---------------------|
| Turbine nominal power output (P_{out}) | Electrical Resistor power ratio | Hot Air power ratio |
| 200 KW | 0.10 | 0.13 |
| 600 KW | 0.09 | 0.12 |
| 2 MW | 0.06 | 0.08 |
| 5 MW | 0.045 | 0.06 |

4.1 Aerodynamic Power Loss Data for Different Ice Accumulations

The wind turbine average power loss ratio is approximated due to icing (averaged over wind speeds between 5-20 m/sec based on Figure 1.2). The average power loss ratio between wind speeds of 5-20 m/sec is approximated as:

- 3%-6% of ice accretion (percentage of chord length) at the leading edge of the tip: $\eta_{ice} = P_{ice}/P_{no-ice} \approx 0.92$
- 22% of ice accretion at the leading edge of the tip: $\eta_{ice} = P_{ice}/P_{no-ice} \approx 0.78$
- 44% of ice accretion at the leading edge of the tip: $\eta_{ice} = P_{ice}/P_{no-ice} \approx 0.62$

In the following wind turbine ADIS profitability analysis, the total energy consumption by ADIS and the total energy saved by activating ADIS are calculated depending on the type of ADIS, icing severity of the operating site, and the percentage of ice accretion on the leading edge at the tip of the blade.

4.2 Profitability Derivations

The total thermal energy consumed by an ADIS system is

$$Q_{th} = N_{P_{heat}} P_{out} t_{Heat-on} \quad (4.1)$$

Defining the heating-time ratio $\tau_{de-ice} = t_{Heat-on}/t$ (also as the ratio of the number of the days within a year that icing happens on the blades to the total number of days in a year), we have

$$Q_{th} = N_{P_{heat}} P_{out} \tau_{de-ice} t. \quad (4.2)$$

The net energy produced by the wind turbine using an ADIS system is

$$Q_{net,ADIS} = Q_{out} - Q_{th} = P_{out} t (1 - N_{P_{heat}} \tau_{de-ice}). \quad (4.3)$$

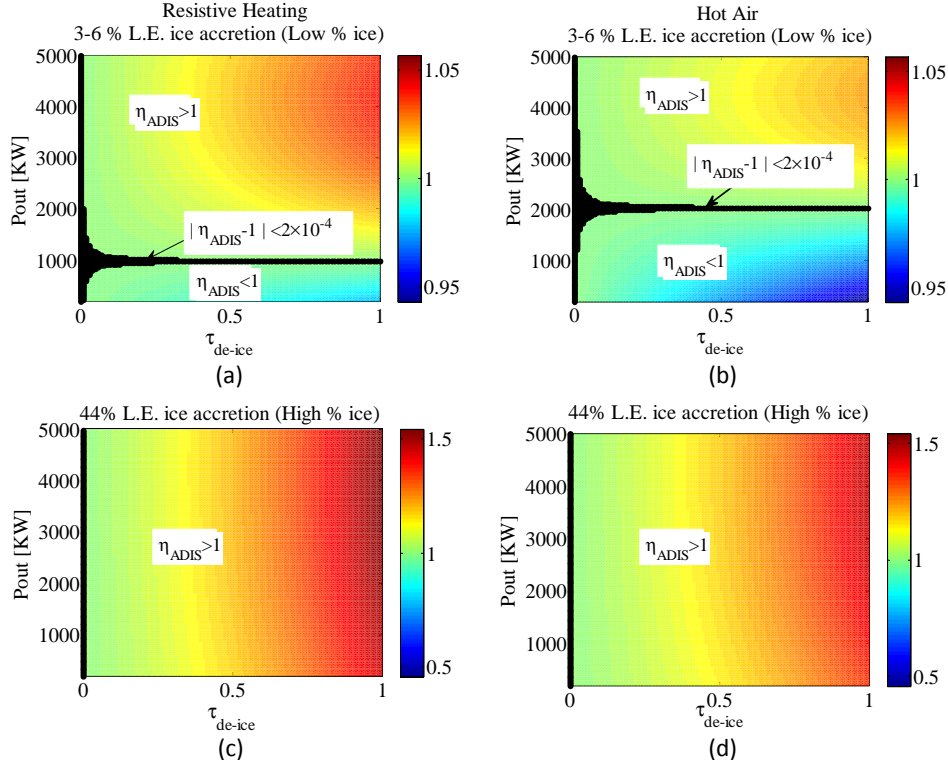


Figure 4.1: Anti/De-icing efficiency factor vs. wind turbine rated power in different site icing conditions for electrothermal resistor and hot air ADIS systems. (a) Resistive heating and low ice accretion. (b) Hot-air and low ice accretion. (c) Resistive heating and high ice accretion. (d) Hot-air and high ice accretion. $\tau_{de-ice} = 0$ corresponds to no-icing event and is treated as a singularity. In (a) and (b), black line shows the regions of $\eta_{ADIS} = 1$ (margin of profitability) within the error bound of 2×10^{-4} .

If no ADIS system is used, we have a power loss due to less efficient operation as a result of ice accumulation. The total time (t_{ice}) that ice is formed on the blades when there is no heating system is a function of the total operational time t and the heating-time ratio τ_{de-ice} as $t_{ice} = \tau_{de-ice}t$.

The time that the blades are free of ice without turning on an ADIS system is $t_{ice-free} = t - t_{ice} = t(1 - \tau_{de-ice})$.

The energy loss during the total operational time due to ice formation can be calculated as

$$Q_{loss,no-ADIS} = (1 - \eta_{ice})P_{out}t_{ice}. \quad (4.4)$$

The net energy produced in this case during the turbine operational time t is calculated as

$$Q_{net,no-ADIS} = Q_{out} - Q_{loss,no-ADIS} = P_{out}t - (1 - \eta_{ice})P_{out}\tau_{de-ice}t = P_{out}t(1 - \tau_{de-ice} + \eta_{ice}\tau_{de-ice}). \quad (4.5)$$

The ADIS efficiency factor η_{ADIS} is defined as the ratio of the net energy $Q_{net,ADIS}$ produced by the wind turbine when an ADIS system is used, and the net energy $Q_{net,no-ADIS}$ produced by the wind turbine without using the ADIS system:

$$\eta_{ADIS} = \frac{Q_{net,ADIS}}{Q_{net,no-ADIS}} = \frac{1 - N_{P_{heat}}\tau_{de-ice}}{1 - (1 - \eta_{ice})\tau_{de-ice}}. \quad (4.6)$$

$\eta_{ADIS} = 1$ means it does not matter if we use ADIS during the operational time t , and the amount of net energy produced will be the same for both ADIS and no-ADIS cases. For $\eta_{ADIS} > 1$, using ADIS system is beneficial in the amount of net energy produced by the wind turbine. η_{ADIS} obviously depends on the time $t_{Heat-on}$ that the heating system is turned on and therefore on τ . Equation (4.6) shows that η_{ADIS} increases with a higher heating-time ratio τ_{de-ice} . In order to prevent decreasing of the aerodynamic efficiency of the turbine during icing days, the heating system should be active at least during this time period.

Figure 4.1 shows colored-map simulations of the ADIS efficiency factor η_{ADIS} as a function of wind turbine size (P_{out}), icing severity conditions (τ_{de-ice}), and ice accretion amounts at the blade leading edge for electrothermal resistor and hot air ADIS systems. The calculations in terms of energy consumption show that using de-icing systems is more beneficial in harsher cold environments (with larger heating-time ratio τ_{de-ice}), for larger ice accumulations on the blade, and for larger size wind turbines; and that the electrothermal resistor ADIS system is more effective than the hot air ADIS system. Figure 4.1a shows that using an electrothermal resistor de-icing system in a site with low ice accretion is only beneficial for wind turbines with rated powers larger than 1 MW while for a site with severe ice accretion, having an active electrothermal resistor de-icing system is beneficial for a larger range of wind turbine sizes in terms of net energy production. Figure 4.1b shows that using a hot-air de-icing system in a site with low ice accretion is only beneficial for wind turbines with rated powers larger than 2 MW and heating-time ratios larger than 0.3. A larger profitable region is seen in Figure 4.1a than Figure 4.1b due to higher efficiency of resistive heating than hot air de-icing method. Figure 4.1c and Figure 4.1d show the simulations of the ADIS efficiency fac-

tor for large ice accretion amounts (44% of the chord of the blade) for resistive heating and hot-air de-icing systems. It is seen that under severe ice conditions, using a de-icing is always profitable for all wind turbine sizes and heating-time ratios. These figures show similar de-icing efficiency with slightly lower efficiency for the hot-air system under severe ice accumulation conditions. These predictions agree with published literature on payback time and profitability analysis of Finnish Lapland [28]. Again, the profitability calculations shown here are without considering the wind turbine downtime under cold conditions. If this downtime effect is taken into account, ADIS efficiency factor (η_{ADIS}) will be even higher compared to the values shown in Figure 4.1, further reinforcing the necessity of de-icing systems in cold climates.

4.3 Estimated Equipment Cost and Payback Time for the Proposed Active Distributed De-icing

The cost of equipment and installation for the proposed de-icing technique based on the current demonstrated lab technology on a typical horizontal-axis, three-bladed 5 MW wind turbine is estimated to about 100000 dollars with the assumption of using optical ice sensors and distributed resistive heaters that cover 30% of blade tip area (within 30% of the blade span from the tip) and 30% of the blade leading edge area (within 30% of the blade mean chord from leading edge). The itemized cost breakdown of the proposed system is summarized as:

- Cost of the used laser source: 40000 dollars
- Cost of the optical sensors: 20000 dollars
- Cost of the temperature sensors: 5000 dollars
- Cost of the thin resistive heaters: 10000 dollars
- Cost of the designed power electronic system for power amplification of the signals to heaters: 5000 dollars
- Cost of remaining hardware including data acquisition boards and optical fibers: 5000 dollars

- Deployment and install cost of optical sensors: 15000 dollars
- Total equipment and deployment cost of about 100000 dollars

Assuming a 0.3 fractional operational time for a 5 MW wind turbine, total annual energy production for this wind turbine facing no icing conditions is 13140 Mega-Watt hours. Assuming the average price of each Mega-Watt hour energy including production tax credit to be 90 dollars, equivalent dollar production for this wind turbine is about 1.18 million dollars. For a 5 MW wind turbine with 1 month of medium icing condition, and losing 30% of aerodynamic power production, and de-icing power consumption of below 1% of the rated power during icing conditions (compared to 10-15 % of rated power consumption for de-icing reported in the literature), the calculated pay-back time based on total cost of the system will be lower than 4 years. The estimated pay-back time of this system can be even reduced further by either improving de-icing efficiency by means of a closed-loop thermal actuation (discussed in chapter 7) or additional cost reduction by improving the proposed de-icing technique.

Chapter 5

Experimental Setup and Closed-Loop Experiments

In the first part of this chapter, different components of the fabricated experimental setup will be explained for closed-loop de-icing on a small-scale wind turbine blade. This custom experimental setup provides the capability of investigating more advanced types of controllers in order to achieve optimal thermal actuation in a distributed network of heaters and sensors. In the second part of this chapter, experimental results of de-icing will be shown for two types of Proportional, Integral and Derivative (PID) controllers and their de-icing performance will be compared. Conclusions and experimental observations will be summarized at the end of this chapter.

5.1 Experimental Setup Description

At ice temperatures below 0°C , before any melting occurs, optical ice sensors cannot provide enough information for control gain calculation since the ice thickness and type does not change by heating. Therefore, combined temperature and optical ice sensors are used for closed-loop thermal control before any phase change of ice. Below the melting temperature, optical ice sensors determine which actuator should be active while temperature information is used to calculate the controller gains. Alternatively, ice thickness information provided by the ice sensors can be used to calculate control gains during ice thickness variation.

An experimental setup has been built to create different types of ice on a blade and to implement active de-icing using combined optical ice/temperature sensors and distributed resistive heating with adjustable heat flux in different blade locations using feedback control. This section describes the components of the experimental setup, including resistive heaters, optical ice sensors, custom fabricated icing chamber, and

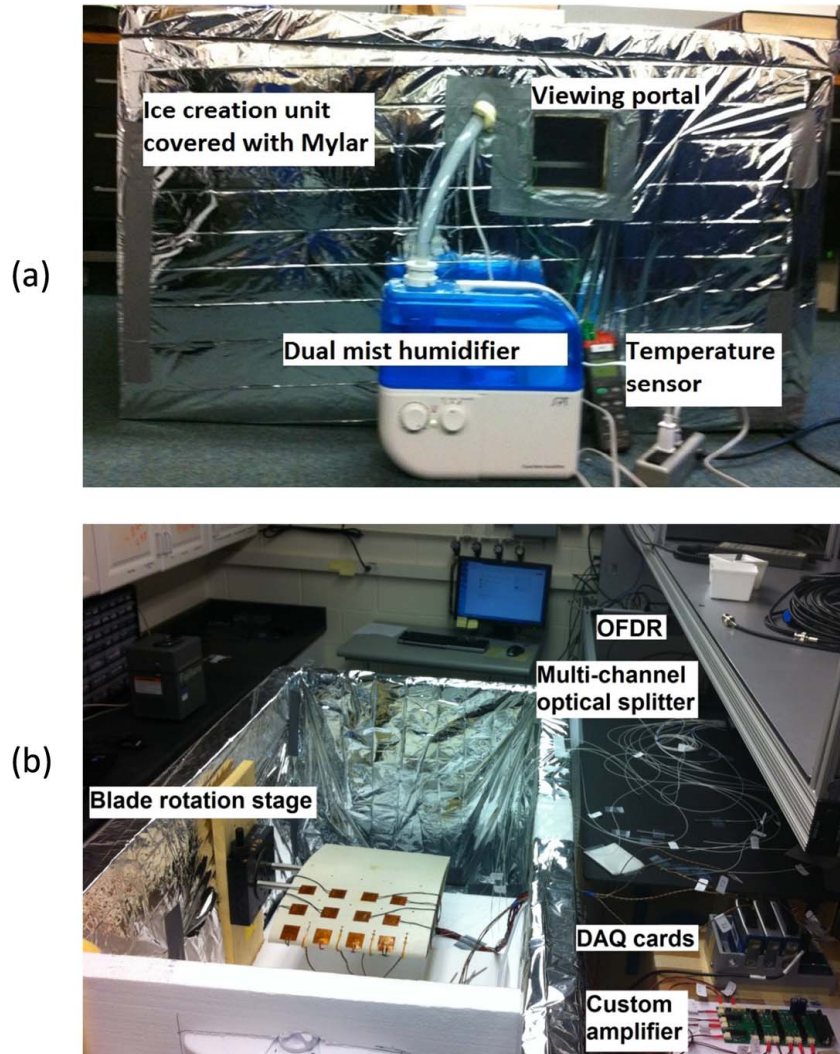


Figure 5.1: (a) Cooling chamber for ice creation on the blade surface. (b) Different components of our test setup at a glance.

amplifier circuit board.

De-icing is investigated under a fixed blade pitch angle for a non-rotating blade inside a thermally-insulated custom cooling chamber (Figure 5.1a). Different types of ice can be created by controlling temperature, humidity, and wind speed inside the chamber. This custom cooling chamber is less expensive to operate than an icing wind tunnel. However, there are some limitations such as stationary blade installation and longer time for ice creation inside the chamber compared to an icing wind tunnel. The experimental results of de-icing for a stationary blade can be extended to a rotating blade using further computational simulations. Wind is

generated by a box fan installed inside the test section. Blade pitch angle can be changed between tests by a rotation stage inside the chamber which affects pressure distribution and convection heat loss at different blade locations. This allows us to investigate de-icing performance under different aerodynamic and heat loss conditions. Thin flexible electro-thermal heaters [40] with 5-watt and 10-watt power ratings are used in different regions of the blade for thermal actuation. Twelve resistive heaters (ten 5-watt and two 10-Watt) are mounted from the leading edge up to $1/3$ of the chord length of our blade with higher power resistors placed at the leading edge. The ice/water dynamics including melting and refreezing are potentially quite complex. In chapter 6, the optimization of the layout of heaters will be studied in greater detail. Because of lower relative wind speed, Reynolds number, convective heat loss, and contribution to power production, the first two-thirds of the blade (towards the blade root) is less important to be de-iced. Installing distributed heating elements only on the last third outboard section of the blade enables decreasing equipment costs and de-icing power consumption while maintaining 90% of the aerodynamic performance of the clean blade with only 30% of the length de-iced [18].

In a distributed resistive heating network, given the boundary conditions (ice geometry, convection, and temperature here), the optimal distance between heaters varies as a function of de-icing time and blade conductivity. The heaters distance needs to be accurately selected to minimize the area of the regions on the blade that heat flux never reach during de-icing. A finite difference code is developed to determine the transient heat conduction on the blade for computing the optimal distance between heaters. This calculation satisfies de-icing controllability on different regions (by sending required heat flux to different blade regions) within a reasonable amount of de-icing time (20 minutes to 1 hour) given the conductivity of the blade. More detail calculations of heater's distance will be discussed in section 6.2.2 of chapter 6. The local required heat flux is a function of blade location, pitch angle, and environmental conditions (altitude, ambient temperature, wind speed, and direction). Optical ice sensors are distributed on the blade such that each thermal actuator is surrounded by four sensors. Optical fibers terminate in GRIN lenses mounted flush with the surface of the blade. Ice sensors (3 mm in diameter and 6 mm in height) are installed in drilled holes of the same size and attached with water resistant glues for environmental stability (Figure 5.1b). Four thermocouples [40] are placed close to the leading edge ice sensors for gain calculation of the PID control

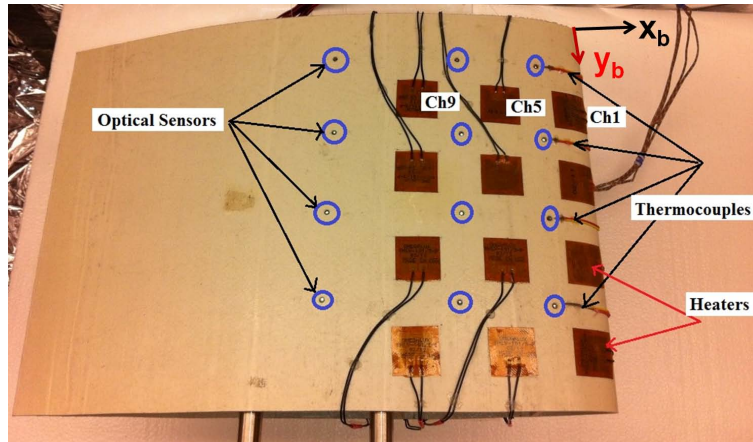


Figure 5.2: Distributed optical ice sensors, leading edge temperature sensors, and resistive heaters on a blade segment. Resistor rows are along y_b axis, and resistor columns are along x_b axis. The optical sensor and the resistor in the top column closer to the blade leading edge are both labeled as channel 1.

that is a function of the difference between desired temperature (slightly above 0°C) and instantaneous local temperature. It is economically preferable to use fewer temperature sensors on the blade. Hence, distributed temperature sensors are only installed on the leading edge area. Thin temperature sensors are used to prevent aerodynamic degradation.

Figure 5.2 shows distributed optical sensors and resistive heaters on the blade. Ultimately for active de-icing implementation on a full-scale wind turbine, it is necessary to have distributed resistors embedded inside the composite blade to lower the risk of damage by lightning. As mentioned earlier, distributed resistive heating provides an efficient local control of heat flux on the blade. However, due to a large number of actuators and sensors in this method, the possibility of a fault in the network should be considered in the design as an area of future work.

Under some very cold conditions, instant freezing of the run-back water might occur at the edges of the heating elements or on some cold blade areas that are not covered by heating elements. This could form a barrier at the edges of the heating element. The edge barriers may tend to grow towards the leading edge as “horns” without a contact with the heating element. Those horns that happen to grow on the optical sensors could immediately be detected and de-iced by locally increasing thermal flux using the surrounding heating elements. Intuitively, using a staggered array configuration of heaters instead of an aligned array can

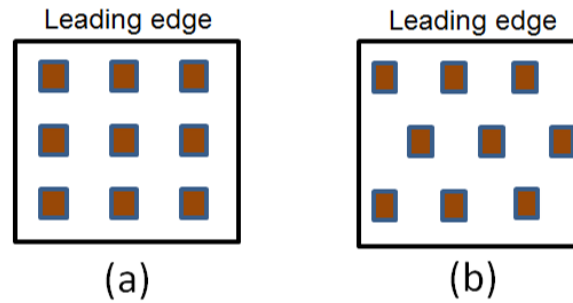


Figure 5.3: Heating elements in: (a) aligned array and (b) Staggered array.

be more efficient (Figure 5.3) for preventing these local horns to grow all the way toward the leading edge where icing leads to large aerodynamic losses. In addition, placing resistive heaters in both upper and lower surfaces of the blade close to the leading edge area can be considered to even further reduce the potential threat of ice horn residues in this region.

Figure 5.4 shows a schematic diagram of the closed-loop control. Numerical signal processing [32] detects the ice existence, type, and thickness by each optical ice sensor based on the magnitude of the peak, the signal asymmetry, and backscatter level. Each optical scan (for all the channels) including numerical detection takes less than 2 seconds in the loop. As such, we use a closed-loop control update rate of 0.5 Hz. This is sufficiently fast for the desired thermal response bandwidth of 0.001 to 0.01 Hz for the actuation network. Both the control system software and OFDR software have been developed in LabVIEW [38].

The result of the numerical ice detection algorithm is sent to the closed-loop control system at 0.5 Hz. The command voltage output of the control software is amplified through a custom fabricated multi-channel op-amp circuit and fed to the distributed resistors on the blade.

5.2 Computational Model Validation with Experiments

Accurate prediction of the aero/thermodynamic response of a rotating blade covered with ice/snow and distributed electrothermal resistors is complex due to the coupled nonlinear dynamics of turbulent wind, the ice/water phase change, and multiple distributed heat sources on the blade. Experimental validation is required to achieve a reasonably accurate computational prediction for the behavior of such a complex

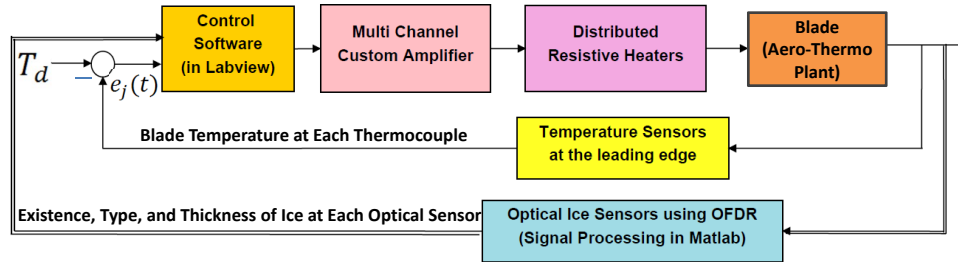


Figure 5.4: Closed-loop control schematic diagram. $T_d = 2^\circ\text{C}$ is the desired blade surface temperature and $e_j(t)$ is the error signal between the desired blade temperature T_d and the actual blade temperature at the j^{th} thermocouple.

system. In this section, transient thermal response of a composite blade undergoing distributed thermal actuation is compared between the developed computational model in ANSYS [3] and an experimental result performed using the test setup. The geometry of the hollow blade with distributed resistors is modeled in SolidWorks [10]. This geometry is imported into the ANSYS Workbench environment for computational simulations (Figure 5.5). The transient thermal module in ANSYS is used to compute the temperature variation as a function of time on the blade for different heater layouts. In the simulations explained in Section 6.1.2 of chapter 6, a variable time step is implemented with a minimum time step of 0.05 seconds and maximum time step of 0.5 seconds. In the ANSYS analysis setting, heat and temperature convergence modes are activated for achieving better stability and convergence of the numerical simulations.

A temperature sensor is placed between two of the middle resistors in the second and third row to record the variation of the temperature (Figure 5.6). Figure 5.7 shows the experimentally applied input voltage to all of the resistors as a function of time created by a PID control to increase the initial temperature of the blade from 24.9°C to about 30°C . Then, a fifth-order polynomial curve, shown in Figure 5.7, was fit to the input voltage using a least squares curve fitting method. Using this fitted input voltage, the generated heat flux from each resistor (q (Watt/m²)) is calculated as

$$q = q_{max} \cdot \left(\frac{v}{v_{max}} \right)^2 \quad (5.1)$$

where q_{max} is the maximum resistor heat flux (Watt/m²) at maximum applied voltage, v is the input voltage

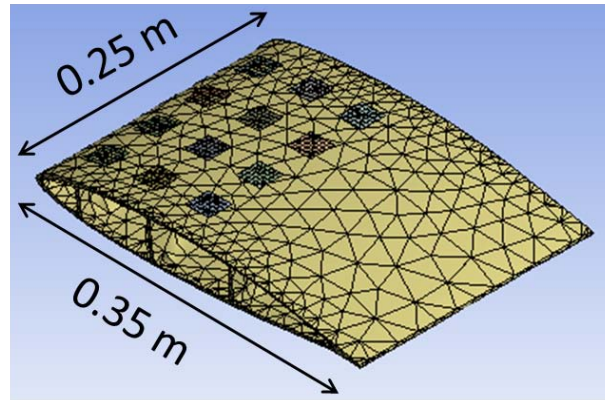


Figure 5.5: Created blade geometry in SolidWorks for computational analysis with the volume of $5.33 \times 10^{-4}(\text{m}^3)$.

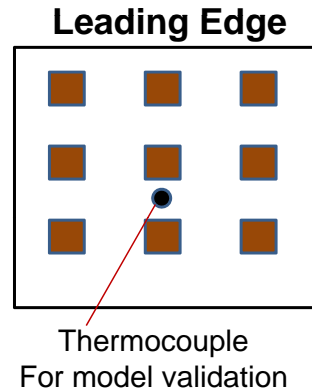


Figure 5.6: Location of a temperature sensor installed for experimental validation of the computational ANSYS model in an aligned heater layout.

to the resistors (volts), and v_{max} is the DC input voltage to the resistor at maximum power (volts).

For validating the developed computational framework in ANSYS with the experiments, experimental results of temperature variation using PID control are compared with the results generated by the computational framework. The calculated input heat flux from experimental input voltage is applied to the heater network in ANSYS computational model under a natural air convection condition, with no forced wind velocity for a stationary blade. Later, the values of convective coefficient of heat transfer for the experiments h and the blade thermal conductivity K are calculated for the best matching between experimental and computational temperature for the distributed thermal resistors. The natural convective heat transfer coefficient

of air is in the range $h = 5$ to $25 \text{ Watt}/(\text{m}^2 \cdot ^\circ\text{C})$, and the range of the thermal conductivity for a typical composite material is $K = 0.2$ to $1 \text{ Watt}/(\text{m} \cdot ^\circ\text{C})$. Assuming natural convection on the upper and lower surfaces of the blade, the temperature variation on the blade is calculated at the location of the temperature sensor for both $h = 6 \text{ Watt}/(\text{m}^2 \cdot ^\circ\text{C})$ and $h = 7 \text{ Watt}/(\text{m}^2 \cdot ^\circ\text{C})$, and with a composite blade thermal conductivity of $K = 0.3 \text{ Watt}/(\text{m} \cdot ^\circ\text{C})$. Figure 5.8 shows the temperature comparison between our recorded experimental data and the simulated values in ANSYS, showing the best matching results between the computational and experimental results using least square curve fitting approximation. It is seen that the computational framework accurately predicts the experimental behavior of dynamic variation of temperature for a distributed network of heaters on a stationary blade. This computational framework further provides the capability of de-icing simulations for rotating blades which is not available in the current experimental setup used for this research. The closed-loop results of distributed de-icing on a rotating blade will be further discussed in chapter 7 using the validated computational framework.

5.3 Closed-Loop De-icing Experimental Results

In the first part of this section, closed-loop experimental results of active de-icing on a stationary blade are described using an initial distributed PID controller with combined ice and temperature sensing. Further, the total amount of consumed energy relative to the size of the blade will be discussed. In Section 5.3.2, experimental results of this PID controller are compared with a higher intensity pulse amplitude modulation (PAM) actuation that uses the same amount of electrical energy. The magnitude and duty cycle of the PAM signal is updated at each time step based on the magnitude of the continuous PID signal to match the consumed energy over one signal period.

For the results described in this section, each heater receives information from the two adjacent optical ice sensors, and the heater stays on only if both of the adjacent ice sensors detect ice. Ultimately information from all of the four optical ice sensors adjacent to each resistor can be used if necessary; however, this makes the closed-loop controller slower. The initial control systems discussed here only use ice existence information. Further experimental investigation is needed for a characterization of the thermodynamic characteristics of different types of ice.

The control gains for each heater at the leading edge are calculated based on the temperature information from the adjacent temperature sensors. For the initial closed-loop test of de-icing, since there is only one temperature sensor for each “column” of thermal resistors in the chordwise direction of the blade, the same voltage was applied for each column of resistors. Figure 5.9 shows different stages of ice formation on the blade before the active de-icing control system was switched on in the icing chamber. Figure 5.9a shows rime and glaze ice formed on the blade in the icing chamber. Figures 5.9b and 5.9c show further accumulation of rime and glaze ice on the blade after 17 min and 90 min from the early ice formation shown in Figure 5.9a. Glaze ice was created in the chamber by directly pumping humidity to the blade surface under the condition of no wind. Uniform rime ice is created on the blade when there is non-zero wind velocity in the icing chamber (from a fan).

5.3.1 Low Intensity Continuous PID Controller

A PID control has been implemented to each column of resistors in the network. The applied voltage to resistor j is:

$$v_j = K_g \left[K_p e_j(t) + K_i \int_0^t e_j(\tau) d\tau + K_d \frac{d}{dt} e_j(t) \right] \quad (5.2)$$

where K_g is the gain of the op-amp circuit, $e_j(t)$ is the error between the desired temperature (T_d) and current temperature ($T_{a_j}(t)$) on the blade for channel j at time t , K_p is the proportional gain, K_i is the integral gain, and K_d is the derivative gain.

Figure 5.10 shows the time history of the voltage and temperature for channel 1 (see Figure 5.2) from the beginning to the end of the activated PID control for de-icing using distributed resistors, optical ice sensors, and temperature sensors, where the maximum voltage indicates that approximately half of the maximum power capability of the individual kapton resistor has been used. Similar behavior has been captured with the remaining resistors. It takes approximately 3 minutes until the resistive heaters start to increase the local temperature at the leading edge, two centimeters away from the edge of the boundary of the leading edge resistors. Then the voltage on the resistor decreases as the temperature increases toward

the desired temperature (+2 °C). After de-icing and satisfying a no-ice condition on both of the optical channels 1 and 2, the control system automatically shuts down the corresponding resistor 1. This de-icing took about 30 minutes in ambient temperature of approximately -10 °C inside the icing chamber while the outer blade surface temperature reached the desired temperature (T_d) at the corresponding channel 1 thermocouple. Ice melting started to happen approximately 17 minutes after switching on the controller.

The total average power consumption from time 0 to t for the distributed resistor network is calculated as

$$P_{total} = \sum_{j=1}^{n=12} \frac{1}{R_j t} \int_0^t v_j^2(\tau) d\tau. \quad (5.3)$$

where n is the total number of resistors in the network, R_j is the resistance of heater element j , and v_j is the applied voltage to element j . The total power consumption for the network of 12 resistors using distributed PID control in our test was about 4 Watts. Our blade dimension is approximately 1/100 of a blade on a 500 KW wind turbine. Simply scaling up, a similar PID controller and de-icing network on a three-bladed 500 KW wind turbine needs about 1200 Watts of de-icing power which is only about 0.24% of the rated power, which is similar but somewhat less than the experimental study in [11]. This is a very small power consumption for an active de-icing system which could improve the net average annual power capture significantly by improving aerodynamic efficiency and reducing wind turbine downtime under icing conditions [43, 56]. The fractional power consumption for this localized heating is only about 10% of uniformly heating the entire blade.

5.3.2 High Intensity Pulse Amplitude Modulation (PAM)

A number of tests have been performed to compare de-icing performance between the low intensity continuous PID actuation described in Section 5.3.1 and a higher intensity PAM actuation. PAM actuation is preferable and more efficient compared to duty-cycle modulation with constant amplitude as long as we ensure that the amount of thermal power does not cause large local thermal stresses that can hurt the blade structure. Much higher signal amplitudes for de-icing are initially required when the outer blade surface temperature may be much lower than the desired blade outer surface temperature. In PAM, the signal amplitude goes to zero as the desired blade outer surface temperature is reached.

Figure 5.11 shows pictures of de-icing results for these two actuation methods over time. Ice is first “grown” on the blade to approximately 5 mm thickness across both resistive heaters. Then the two different control strategies are turned on simultaneously on the two different resistive heaters with an update rate of 10 Hz. For this experiment, optical ice sensors were switched off from the closed-loop controller since we started with the known initial ice condition on the blade. Therefore, a faster update rate of 10 Hz was implemented compared to the results shown in Figure 5.10, where an update rate of 0.5 Hz was used with active optical ice sensors in the closed-loop. In Figure 5.11, both of the resistors use the same amount of electrical energy. It is shown visually that PAM provides better de-icing results and faster thermal energy propagation through the composite blade.

Figure 5.12 shows the applied voltage and temperature variation for these two different actuation techniques. It is seen that PAM actuation has a better de-icing performance than continuous PID control when using the same amount of electrical energy by yielding a higher temperature at the closest thermocouple at all times. These two temperature sensors are mounted diagonally from the corner of each resistive heater with the same distance. The improved performance of the PAM controller is due to a high thermal inertia of the resistive heaters that can hold the required heat for a while (more than 15 seconds) even after switching off before the generated thermal energy is fully dissipated by convection loss. Further investigations are needed for different wind speeds and blade pitch angles. These test results are for no-wind condition (natural convection) and a non-rotating (stationary) blade where convection loss is normally less compared to a rotating wind turbine under similar environmental conditions.

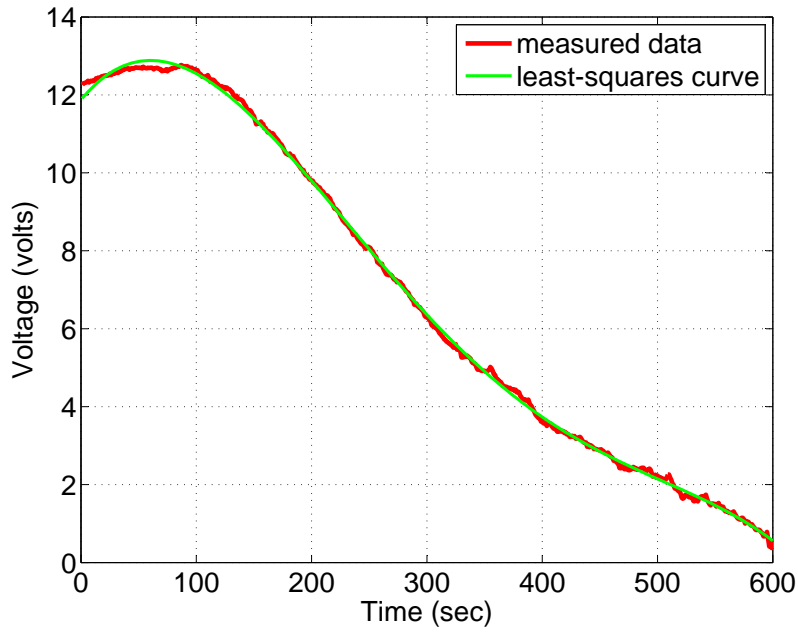


Figure 5.7: Experimental input voltage to the resistive heaters.

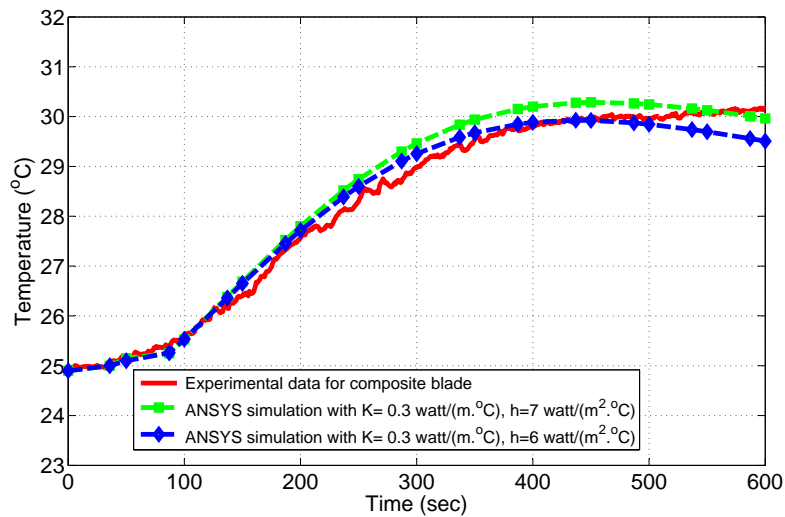


Figure 5.8: Validation of the computational model developed in ANSYS with the experiments for a stationary small-scale blade segment.

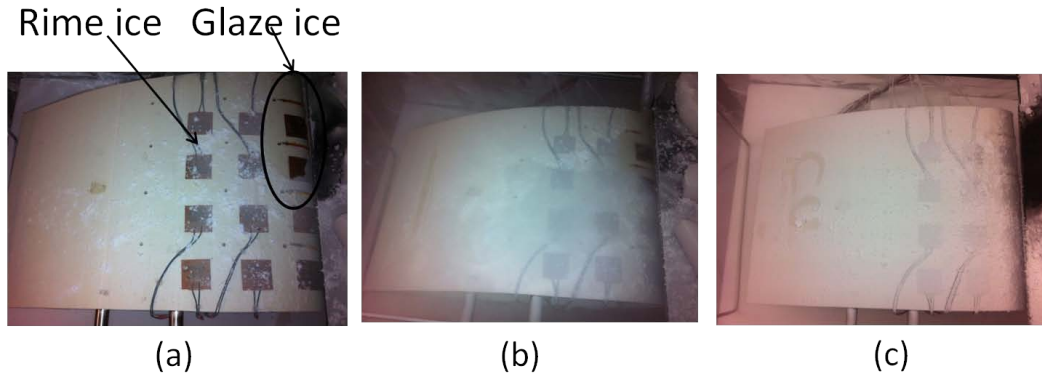


Figure 5.9: Different stages of ice formation on the blade before switching the controller on. (a) Rime and glaze ice started to form on the blade at $t = 0$. (b) Blade slightly covered with rime ice at $t = 17$ min. (c) Blade covered with 5 mm-thick rime ice at $t = 90$ min.

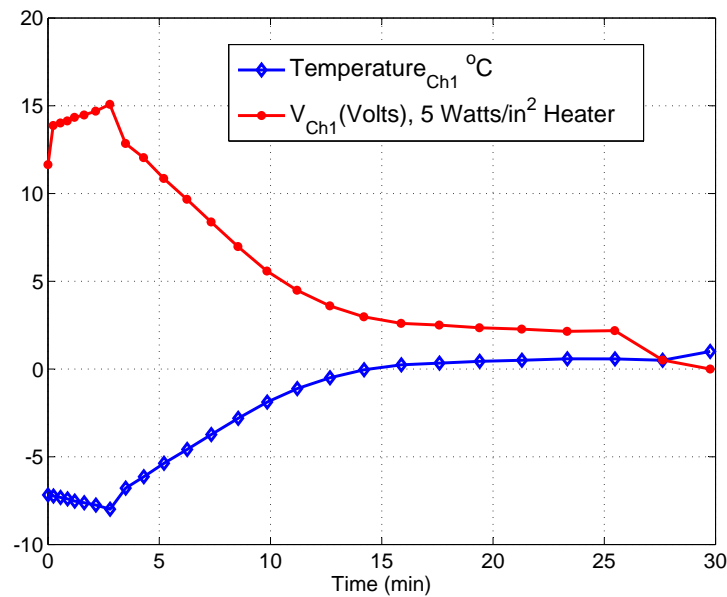


Figure 5.10: Time history of voltage and temperature for a selected channel when using distributed PID control for de-icing, using approximately half of the maximum power capability of the actuation system with empirically tuned PID gains of $K_p = -0.5$ v/(°C), $K_d = -0.01$ v/(°C/s), $K_i = -0.001$ v/(°C·s), and closed-loop update rate of 0.5 Hz.

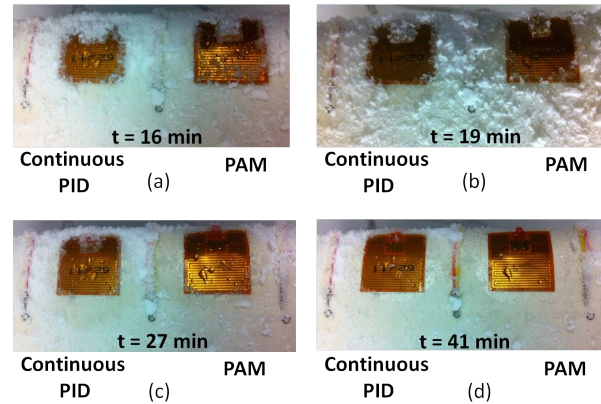


Figure 5.11: Visual comparison of low intensity continuous PID actuation versus higher intensity PAM actuation with the same amount of electrical energy expenditure. The PAM frequency is 0.1 Hz. Over each period, the PAM actuation has a 40% duty cycle, and a pulse magnitude that is 1.581 times larger than the continuous PID signal. The icing chamber temperature is slightly higher than -10°C throughout the test. More rime ice residue can be seen on the heater for the lower intensity continuous PID control compared to the PAM control at all times. (a) $t = 16$ min. (b) $t = 19$ min. (c) $t = 27$ min. (d) $t = 41$ min.

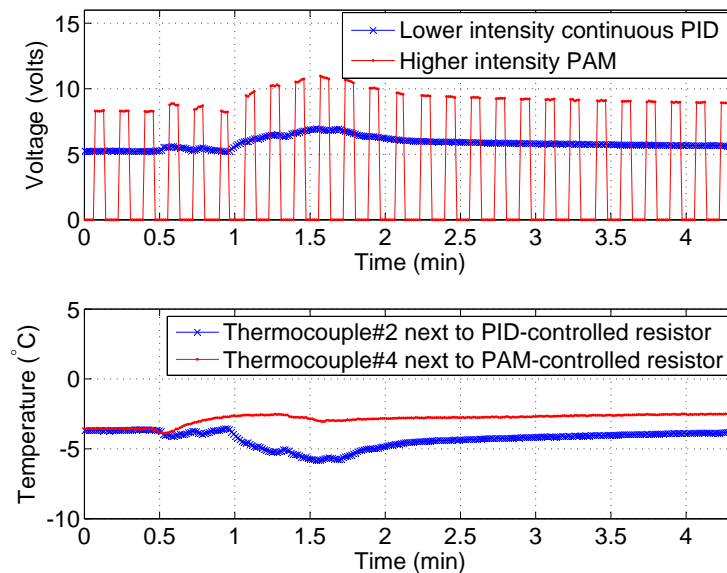


Figure 5.12: (a) Lower intensity continuous PID controller applied voltage (resistor channel 2) with the gains $K_p = -0.25 \text{ v}/(^{\circ}\text{C})$, $K_d = -0.005 \text{ v}/(^{\circ}\text{C}/\text{s})$, $K_i = -0.0005 \text{ v}/(^{\circ}\text{C}\cdot\text{s})$, and PAM applied voltage (resistor channel 3) with the same electrical energy over one signal period. Both are 10-Watt resistors. Lower PID gains are selected compared to the previous subsection (shown in Figure 5.10) to assure that the higher intensity PAM signal is amplified within the operational linear range of our custom amplifier, before reaching the nonlinear saturation limit, and to prevent causing large thermal stresses in the blade structure. (b) Temperature variation at thermocouple 2 adjacent to resistor channel 2 with lower intensity continuous PID signal and thermocouple 4 adjacent to resistor channel 3 with higher intensity PAM signal with the same amount of electrical energy expenditure. The time axis denotes the time after both PID and PAM controllers are simultaneously turned on.

Chapter 6

Evaluating Different Heater Layouts for De-icing Using Constant Heat Flux

The most simple thermal actuation strategy for a distributed network of heaters is an open-loop constant heat flux actuation without any closed-loop control and temperature sensing. In this chapter, we investigate de-icing performance for different layouts and geometries of distributed heaters under the assumption of open-loop constant heat flux using the developed and validated computational method in ANSYS. A time-variant de-icing performance cost function is defined as a function of volume of ice residue, volume of higher-temperature blade regions, and maximum applied temperature to the blade structure for quantitative evaluation of de-icing for different heater layouts. A number of computational modules have been developed in ANSYS-APDL (attached in appendix B) for calculations of different terms inside the defined de-icing performance cost function. These computational modules will be used again for quantitative evaluation of performance of closed-loop de-icing in chapter 7.

In the first part of this chapter, the de-icing performance of different layout of heaters is computationally investigated on the small-scale blade segment used in the experiments (explained in chapter 5). In the second part of this chapter, the de-icing performance of open-loop constant heat flux actuation is analyzed for different layout of heaters on a 1.5 MW wind turbine blade tip segment with a more complex ice geometry modeled at the leading edge area.

6.1 Simulations of Different Heater Layouts for a Small-Scale Blade

In this section, several heater geometries and layouts are explored (Figure 6.1) on a stationary small-scale blade. All of the results for the small-blade discussed in this section are based on low convection boundary

conditions for a stationary blade with $h = 5 - 7 \text{ Watt}/(\text{m}^2 \cdot ^\circ\text{C})$ similar to the experimental results for the stationary experimental small-scale blade segment discussed in chapter 5. It is shown that there are de-icing efficiency advantages to circular heaters in a staggered layout. Circular heaters generate uniform heat flux in all radial directions, and square heaters generate uniform heat flux along their two axes of symmetry. Figure 6.1 shows different heater layouts modeled for ANSYS computational analysis. For the created staggered layouts, only heaters in the second row are shifted in the y_b direction shown in Figure 5.2. For the staggered alignments, in order to keep the geometry symmetric about the axis that connects the mid-point leading edge to the mid-point trailing edge, two half-area resistors are used at each end in the second row of resistors (Figure 6.1b and Figure 6.1d). The total heating area and total input heat flux (therefore total energy) are equal for all of the resistor shapes and layouts considered in Figure 6.1 and in the results that will be discussed in Section 6.1.2. In addition, chord-wise distance (in x_b direction) between the leading edge of the heaters in the front row and the leading edge of the blade are assumed equal for these simulations.

Other heater geometries with isotropic (invariant with respect to direction) thermal energy generation in chord-wise and span wise directions were also investigated as boundary cases. It was observed that the de-icing performance of other regular polygon-shaped heaters (pentagon, hexagon, etc.) is between square and circular heaters. Therefore, the performance of only square and circular heaters will be discussed in Section 6.1.2 as the lower and upper bound of the de-icing performance.

A uniform 3-mm glaze ice layer on the blade from the leading edge to 1/3 of the chord length is incorporated into the numerical model, as shown in Figure 6.2. The ice layer covers all of the distributed resistors mounted on the blade. This uniform ice thickness model is assumed for the purpose of optimizing the heater layout. However, a non-uniform ice layer based on experimental field data is needed for the purpose of investigating aerodynamic efficiency degradation and calculating lift and drag coefficients for an icy airfoil, which is not the focus of this dissertation. The physical properties of the glaze ice layer and the composite blade were carefully modeled in ANSYS, including the melting point, density as a function of temperature, specific heat as a function of temperature, and thermal conductivity. The heater material was assumed to be “structural steel” from the ANSYS material library in creating the models.

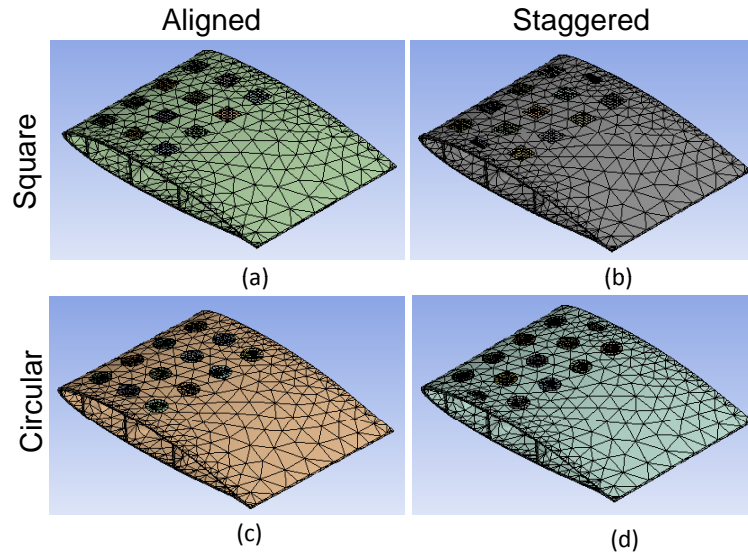


Figure 6.1: Different heater layouts. (a) Aligned square layout. (b) Staggered square layout. (c) Aligned circular layout. (d) Staggered circular layout.

6.1.1 De-icing Performance Metric for Heater Layout Evaluation

In order to quantitatively evaluate the de-icing performance of distributed thermal actuation, a performance metric is needed. This performance cost function should consider the de-icing time (t_{di} [sec]), maximum global temperature to the blade structure during de-icing (T_{max_b} [$^{\circ}$ C]), the volume on the blade experiencing higher than a certain temperature (30° C here as $V_{T>30}$ [m^3]), and thermal power consumption. Both T_{max_b} and $V_{T>30}$ give indications of the level of thermal stress on the blade due to the localized heating. A more advanced metric may also consider additional parameters such as setting priority for de-icing in those regions on the blade with higher contributions to the aerodynamic torque production (regions close to the leading edge and the blade tip), cost of the heaters, etc. In general, the total cost of a heater network is a function of wind turbine size, blade dimension, and total number of heaters on a full-scale blade. This financial cost has not been included in the performance cost function in this chapter and is an area of future work.

In order to compare de-icing performance between different heater layouts, assuming the same amount of thermal power consumption, a quadratic performance cost function J is defined as

$$J = X^T W_m X \quad (6.1)$$

where $X = [t_{di}, V_{T>30}, T_{max_b}]^T$ is the de-icing performance state vector, and W_m is a diagonal weighting matrix

$$W_m = \begin{bmatrix} \frac{1}{1350^2} & 0 & 0 \\ 0 & \frac{1}{(3.48 \times 10^{-5})^2} & 0 \\ 0 & 0 & \frac{1}{56.31^2} \end{bmatrix}. \quad (6.2)$$

This weighting matrix W_m was chosen such that, for the aligned square heater layout, the three performance variables inside the de-icing performance state vector X contribute equally to the cost, resulting in a total cost of $J = 3$. The inverse square root of the diagonal elements of W_m are equal to t_{di} , $V_{T>30}$, and T_{max_b} values for the aligned square heater layout shown in the first row of Table 6.1. A smaller value of J is desirable. For the analysis discussed in Section 6.1.2, ice residues in different areas on the blade are assumed to have equal weighting in the de-icing performance. The de-icing end time is defined as the time when the total volume of the ice residue becomes smaller than 10^{-7} m^3 . In Section 6.1.2, the performance cost function J will be calculated for the other heater geometries and layouts to quantitatively compare de-icing performance.

6.1.2 De-icing Performance Comparison for Different Heater Layouts

In this section, the computational modeling of ice melting and de-icing performance comparison is investigated for the different heater shapes and layouts explained in Section 6.2.2. In the following simulations, distributed heaters are placed on both upper and lower surfaces of the blade region starting from the leading edge for the first 1/3 chord length. By investigating different geometries in ANSYS, it is noticeable that placing heaters on both sides of the blade, while using the same amount of total thermal power (meaning using half of the heat flux for each individual resistor) provides a more uniform de-icing especially for those blade geometries that have smaller material cavities, or are less thermally conductive. Intuitively, placing resistors on both upper and lower sides of the blade also provides a more effective de-icing when ice

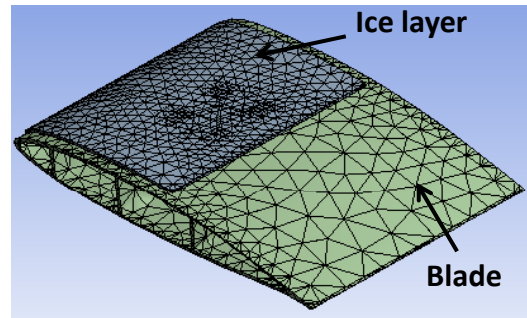


Figure 6.2: ANSYS model of accumulated ice with a uniform thickness of 3 mm with initial volume $V_{ice} = 1.17 \times 10^{-4} \text{ m}^3$, covering the upper surface of the blade from the leading edge to about 1/3 of the blade chord length.

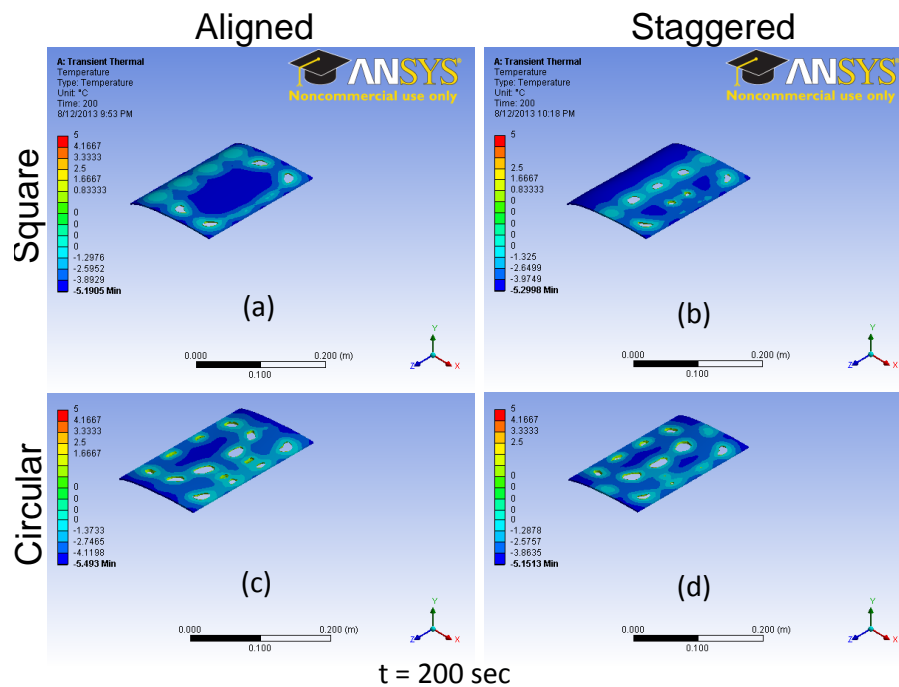


Figure 6.3: Ice residue for different layouts at $t = 200$ seconds after switching on the resistors with an input heat flux of $q = 400 \text{ Watt/m}^2$. (a) Aligned square layout with $V_{ice} = 1.145 \times 10^{-4} \text{ m}^3$. (b) Staggered square layout with $V_{ice} = 1.15 \times 10^{-4} \text{ m}^3$. (c) Aligned circular layout with $V_{ice} = 9.95 \times 10^{-5} \text{ m}^3$. (d) Staggered circular layout with $V_{ice} = 9.78 \times 10^{-5} \text{ m}^3$.

accumulates on both sides of the blade.

For the following simulations in this section, the thickness of the resistors is 0.5 mm. Resistors are modeled as a volume, where each face has the heat flux magnitude of 400 Watt/m^2 . No convection is assumed in the boundary conditions for these simulations. By performing several simulations in ANSYS, it is

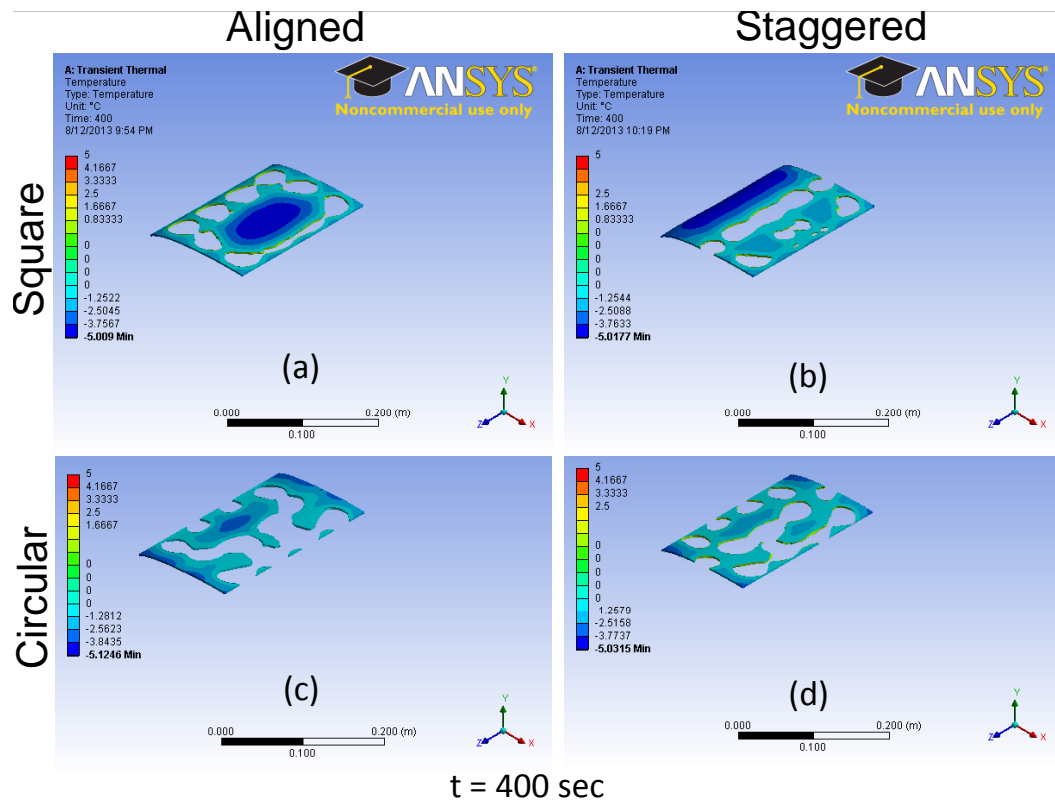


Figure 6.4: Ice residue for different layouts at $t = 400$ seconds after switching on the resistors with an input heat flux of $q = 400 \text{ Watt/m}^2$. (a) Aligned square layout with $V_{ice} = 7.64 \times 10^{-5} \text{ m}^3$. (b) Staggered square layout with $V_{ice} = 8.72 \times 10^{-5} \text{ m}^3$. (c) Aligned circular layout with $V_{ice} = 4.97 \times 10^{-5} \text{ m}^3$. (d) Staggered circular layout with $V_{ice} = 5.58 \times 10^{-5} \text{ m}^3$.

observed that these modifications expedite the simulation time while not fundamentally changing the outcome of the de-icing performance comparison between different heater layouts and the layout optimization. In Figs. 6.3-6.6, the ice layer residue is shown for different heater layouts. For all of these simulations, the ice thickness is divided into four layers (in the mesh setting) in order to accurately capture the ice thickness variation during the melting process. Figure 6.3 shows the ice residue at $t = 200$ seconds after switching on the resistor network. It is seen that ice melting starts faster for circular heaters than square heaters, especially in the areas close to the leading edge due to faster diffusion of the heat flux in those regions. The circular heaters also diffuse the flux more uniformly throughout the ice layer. The staggered circular layout is slightly faster than the aligned circular layout in melting the ice in the middle area of the modeled ice layer. The staggered square configuration does a relatively poor job compared to the other configurations in

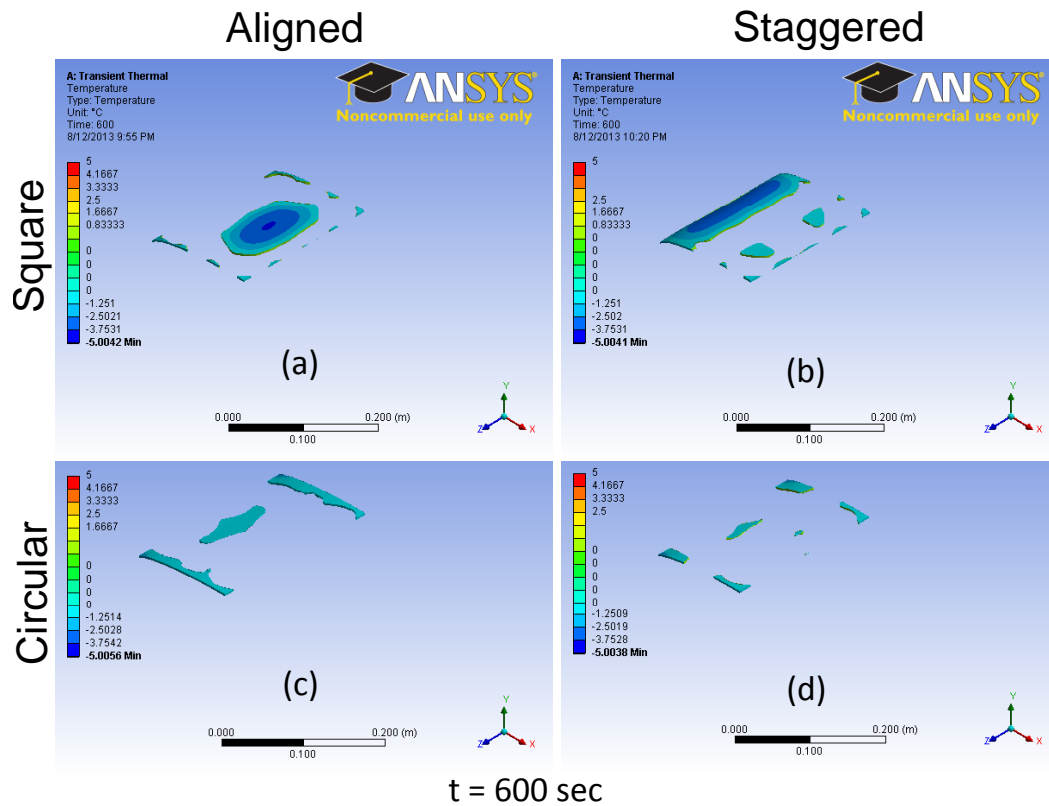


Figure 6.5: Ice residue for different layouts at $t = 600$ seconds after switching on the resistors with an input heat flux of $q = 400 \text{ Watt/m}^2$. (a) Aligned square layout with $V_{ice} = 3.46 \times 10^{-5} \text{ m}^3$. (b) Staggered square layout with $V_{ice} = 4.57 \times 10^{-5} \text{ m}^3$. (c) Aligned circular layout with $V_{ice} = 1.58 \times 10^{-5} \text{ m}^3$. (d) Staggered circular layout with $V_{ice} = 8.1 \times 10^{-6} \text{ m}^3$.

de-icing the areas close to the leading edge.

Figure 6.4 shows ice residue at $t = 400$ seconds after switching on the resistor network. It is observed that the square staggered layout does not effectively provide the required heat flux for melting the ice at the leading edge area, but instead transports higher heat flux at the second row of the heaters. This is aerodynamically less efficient compared to the other layouts. The aligned square layout results in a more effective ice melting close to the leading edge but it can not effectively de-ice the region in the middle of the ice layer. However, de-icing at the middle region is not as crucial as the leading edge area in terms of recovering the aerodynamic efficiency of the blade. Similar behavior is seen in the different layouts after this time until de-icing is completed for the accessible regions to the heat flux diffusion (Figures 6.5-6.6).

Figure 6.6 shows ice residue on the blade at $t = 800$ seconds for the different heater layouts. Among

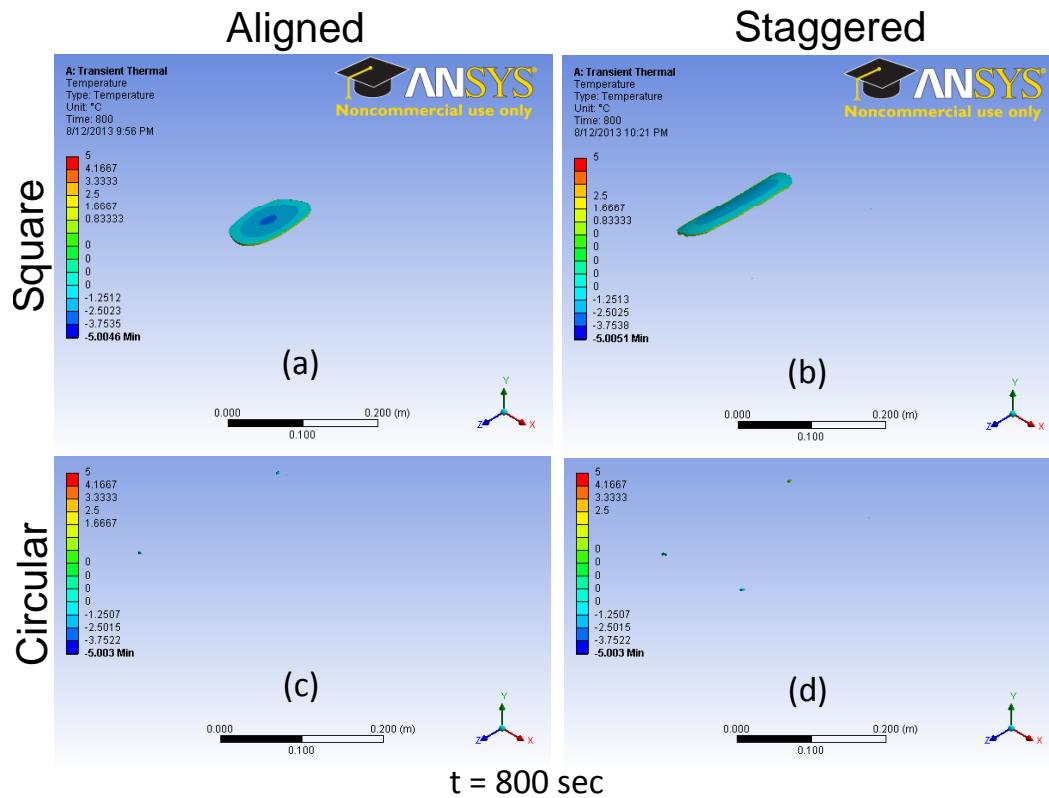


Figure 6.6: Ice residue for different layouts at $t = 800$ seconds after switching on the resistors with an input heat flux of $q = 400 \text{ Watt/m}^2$. (a) Aligned square layout with $V_{ice} = 2.1 \times 10^{-5} \text{ m}^3$. (b) Staggered square layout with $V_{ice} = 2.48 \times 10^{-5} \text{ m}^3$. (c) Aligned circular layout with $V_{ice} = 1.55 \times 10^{-8} \text{ m}^3$. (d) Staggered circular layout with $V_{ice} = 9.63 \times 10^{-8} \text{ m}^3$.

the four compared cases, the circular heaters provide the fastest de-icing time of about 800 seconds assuming that there is no convection loss on the blade surface. Adding equal forced convection loss does not change the outcome of layout performance comparison. Furthermore, the ANSYS simulation results show that the de-icing times for melting the entire ice layer for aligned square and staggered square layouts are 1350 seconds and 1116 seconds, respectively. Although the staggered square layout melts the ice layer faster than the aligned square layout, it is not capable of removing ice from the leading edge area for a long time. Therefore, the aligned square layout is preferable to the staggered square layout for localized active de-icing because it removes the ice first from the leading edge area.

The values of the performance cost function J based on (6.4) for different heater layouts and geometries are shown in Table 6.1. These results show that staggered circular heaters achieve the best per-

Table 6.1: Quantitative performance cost comparison (Percentage reductions for each parameter relative to aligned square layout is written in the parenthesis).

| Heater layouts | t_{di} (sec) | T_{max_b} ($^{\circ}\text{C}$) | $V_{T>30}$ m^3 | J |
|--------------------|----------------|------------------------------------|---------------------------------|----------------|
| Aligned square | 1350 | 56.31 | 3.48×10^{-5} | 3 |
| Staggered square | 1116 (-17.33%) | 41.59 (-26.14%) | 1.73×10^{-5} (-50.29%) | 1.48 (-50.66%) |
| Aligned circular | 813 (-39.78%) | 39.70 (-29.50%) | 6.02×10^{-6} (-82.70%) | 0.89 (-70.33%) |
| Staggered circular | 798 (-40.89%) | 34.18 (-39.30%) | 2.85×10^{-6} (-91.81%) | 0.72 (-76.00%) |

formance with 40% faster de-icing and 39.3% smaller maximum blade temperature compared to aligned square heaters. Furthermore, $V_{T>30}$ is reduced from 6.5% to 0.5% of the blade volume using staggered circular heaters compared to aligned square heaters. Comparing aligned circular heaters to aligned square heaters shows 39.8% faster de-icing, 29.5% reduction in T_{max_b} , and reduction of $V_{T>30}$ from 6.5% to 1.15% of the blade volume for aligned circular heaters. Other polygon heaters (pentagonal and hexagonal) were investigated and it was observed that their de-icing performance cost value J is between square and circular heaters in Table 6.1.

Besides minimizing the total de-icing time and improving ice melting efficiency in the leading edge area, decreasing the amount of applied thermal stress is another important factor to be considered in the design of distributed active de-icing systems. Our calculations show that aligned layouts induce higher thermal stress than staggered layouts, which result in higher maximum temperatures and larger areas with higher temperature on the blade. This observation is more subtle due to the partial absorption of the generated heat flux in the upper surface of the blade by the ice layer. In summary, in the case of using aligned heaters for de-icing, more careful considerations are needed in the selection of closed-loop control gains to avoid high thermal stress induction to the blade structure. Clearly, having reliable and accurate on-the-blade optical sensing prevents this high thermal stress induction by switching off those resistors near the regions where ice does not exist.

6.2 Simulations of Different Heater Layouts for a 1.5 MW Blade Tip Segment

All of the results discussed in Section 6.2.1 are for a rotating 1.5 MW blade tip segment, medium convection and linear variation of convection across the span, no sunshine input heat flux to the ice outer

surface, and with the following operating conditions: tip speed ratio of 6.8, $u_w=12$ m/sec, $\omega = 22.2$ rpm, blade radius of 35.25 m and ambient temperature of -5 °C. The validated computational approach is used to investigate the layout design of rectangular heaters for different numbers of heaters and layouts. A de-icing performance cost function is defined that penalizes the volume of ice residue at different blade regions, the applied thermal stress to the blade structure, and the total cost of heaters in the network. This analysis provides insight for the optimal layout design of distributed heaters using the same amount of total energy consumption for de-icing. Under real conditions, de-icing boundary conditions such as ice geometry, sunshine conditions, ambient temperature, and blade convection loss are generally different from the simulations discussed in this dissertation. Therefore, a sensitivity study with different boundary conditions will be discussed too.

The remainder of this chapter is organized as follows. In Section 6.2.1, the geometry of the modeled ice layer is described. In Section 6.2.2, different heater layouts for computational modeling are explained. In Section 6.2.3, the de-icing performance metric will be discussed. In Section 6.2.4, the computational results will be presented comparing different heater layouts. In Section 6.2.5, a sensitivity study of a few other boundary conditions will be presented.

6.2.1 Non-Uniform Ice Geometry and Boundary Conditions

In cold regions, ice accumulates on the aerodynamic surfaces due to the collision of supercooled water droplets. It forms in different types with different adhesion strengths on the surface. Irregular shapes of ice with non-uniform thickness can be formed across the blade.

A non-uniform glaze ice layer is modeled on the outer segment of a 1.5 MW wind turbine blade. Each blade has a span length of 35 m (R_{tip}), with a chord length of 0.961 m at the blade tip (c_{tip}). Since it is computationally expensive to do the simulations on the full-size blade, the full blade is divided into 20 segments with a span of 1.75 m each (Figure 6.8), and computational simulations are only investigated for blade tip segment, the furthest segment from the blade root shown in Figure 6.7. All of the simulations for different layouts of heaters are implemented on the blade tip segment. The ice layer thickness at the blade tip is 14 mm and linearly decreases along the span toward the blade root. The modeled ice thickness at the root

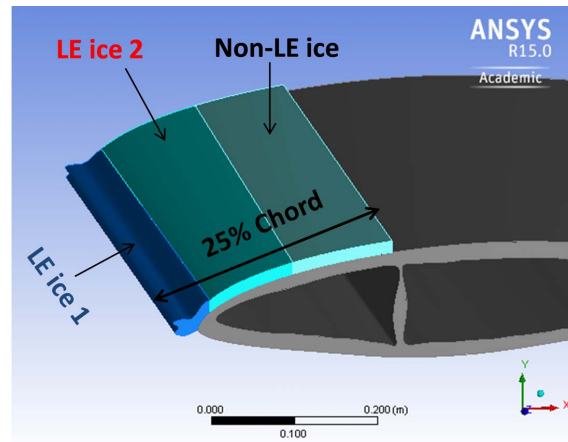


Figure 6.7: Modeled glaze ice layer on the tip segment of a 1.5 MW wind turbine blade covering 25% of the mean chord from the leading edge with a medium size tooth-shape at the leading edge and non-uniform thickness across the blade outer segment, with the thickness of 14 mm at the blade tip and thickness of 8 mm toward the root of the blade tip segment 1.75 m away from the blade tip.

side of the blade tip segment is 8 mm, 1.75 m away from the blade tip. The modeled ice layer covers only 25% of the blade chord from the leading edge due to much higher aerodynamic power loss contribution of ice in the leading edge area. The created ice layer is divided into three volumes all shown in Figure 6.7: “LE ice 1” is the hanging ice attached to the leading edge with an initial volume of 0.0012 m^3 and an initial area of 0.2440 m^2 . The middle section is named “LE ice 2” with an initial volume of 0.0017 m^3 and an initial area of 0.4482 m^2 , and the ice volume furthest from the blade leading edge is named “Non-LE ice” with an initial volume of 0.0015 m^3 and an initial area of 0.4363 m^2 . The blade tip segment shown in Figure 6.7 has a volume of 0.0642 m^3 and an area of 6.9020 m^2 .

Figure 6.9 shows the generated mesh on different ice layers and the blade structure for computational analysis in ANSYS using lower order solid elements with a linear interpolation function (SOLID70) with temperature degree of freedom to solve a transient heat transfer differential equation. The Hexahedral element has eight nodes with single degrees of freedom for temperature in each node [2]. The material properties including the specific heat and enthalpy are calculated at each integration point to allow for abrupt changes (such as melting). Contact elements are used (between contact surfaces with direct heat transfer such as heaters and ice) and modeled through TARGE170 elements in ANSYS based on their temperature and CONTA174 elements in ANSYS to represent other surfaces to improve the accuracy of numerical results

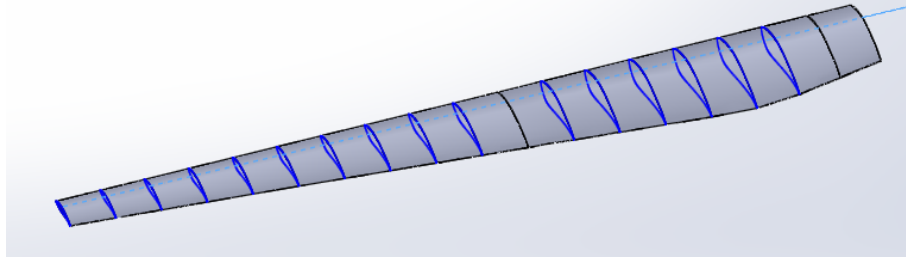


Figure 6.8: A modeled 1.5 MW wind turbine blade divided into different blade segments.

for this transient heat transfer problem. For all of the simulations discussed in this dissertation, no heat loss between internal surface contacts of the ice and blade is assumed and the temperature on the target and contact faces are equal. The heat flux on the heaters have been applied through surface effect elements SURF152 overlaid onto the area faces of 3-D solid elements representing the heaters.

Figure 6.10 shows the modeled convective coefficient of heat transfer on the blade tip segment of the 1.5 MW blade for a medium convection intensity used for the computational simulations. This linear model is accurate enough for the purpose of the closed-loop framework development and de-icing performance evaluation. The heat loss due to convection in this model is assumed to be linearly decreasing from the tip toward the root of the blade for the blade outer segment with the highest value at the blade tip. Values of h were calculated at the tip and root of the blade segment for a medium convection and a linear curve between these two points is used for other span-wise radius values r/R_{tip} .

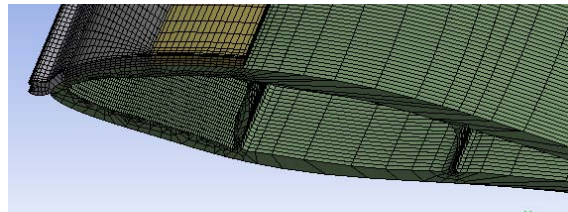


Figure 6.9: Generated mesh for the ice layer and the tip segment of a 1.5 MW wind turbine blade with higher mesh quality closer to the leading edge area modeled in ANSYS using SOLID70 elements with linear shape function (low-order).

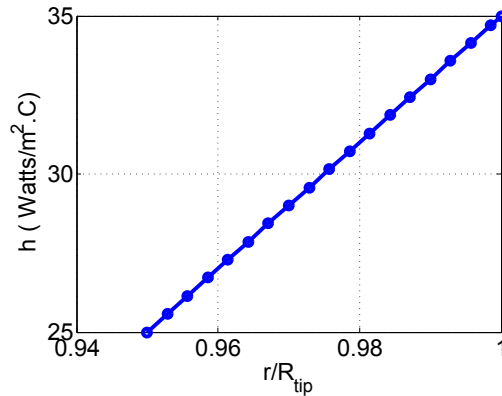


Figure 6.10: Convective coefficient of heat transfer h versus spanwise radius normalized by the radius of the tip (r/R_{tip}). This convective heat transfer on the blade is assumed constant for each blade cross section and linearly increases from the root end to the tip end of the blade segment.

6.2.2 Distributed Heater Layout Configurations

In this section, several rectangular heater layouts (Figure 6.11) are investigated. Rectangular heaters with variable length and width are much easier to fit on the blade inside a rectangular domain compared to other shapes such as circular heaters. Therefore, this dissertation only focuses on rectangular heater layouts. The total heating area and total input heat flux are equal for all of the layouts considered in Figure 6.11. The distance between the heaters are designed for the maximum reachability of the thermal flux to the blade regions between the heaters for a blade thermal conductivity of $K = 1$ Watt/(m·°C). This value is higher than the blade thermal conductivity used in our experimental test setup. Newer generations of the wind turbine blades tend to have higher thermal conductivity due to higher usage of carbon fibers inside the composite blade structure. The distance between edges of the heaters d_H is modeled as

$$d_H = \beta \frac{A_H}{n_H} K^{0.5} \quad (6.3)$$

where A_H is the total area of resistive heaters in the network, n_H is the number of resistive heaters, K is the blade thermal conductivity, and β is a constant tuned to provide highest flux reachability between the heaters for a de-icing time of 1 hour. For the simulations that will be discussed later in this paper, the β value is tuned to 2.75 for a blade thermal conductivity of $K = 1$ Watt/(m·°C).

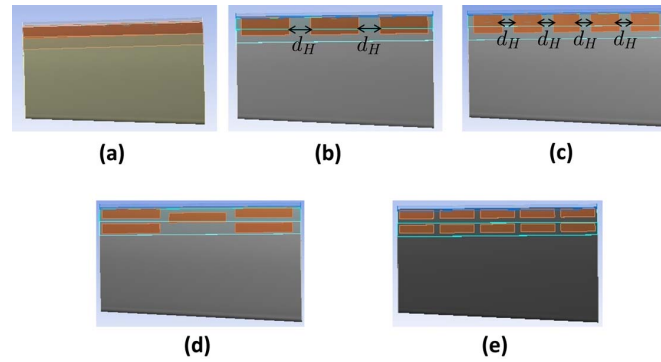


Figure 6.11: Different layout of heaters: (a) 1-piece heater layout, (b) 3-piece heater layout, (c) 5-piece heater layout in a one-row configuration, (d) 5-piece heater layout in a dice-shape configuration, and (e) 10-piece heater layout in a two-row configuration.

In this chapter, the numerical results of de-icing are shown on a tip segment of a 1.5 MW wind turbine blade for different heater layouts shown in Figure 6.11. The first row of the heaters is placed close to the leading edge (only 1 cm away) in order to provide a quick thermal response to the accumulated “LE ice 1” through a low thermally conductive blade composite material. In this study, the heaters are 1 mm thick and mounted on the outer surface of the blade. Placing the heaters at the leading edge could disturb the flow stream, increase the chance of flow separation on the blade, and therefore increase the drag. Instead, if heaters are embedded inside the blade structure, they can be placed at the leading edge area without directly disturbing the flow and creating negative aerodynamic effects; this is an area for future investigation.

6.2.3 De-Icing Performance Metric for Heater Layout Evaluation

In order to quantitatively evaluate the de-icing performance of a distributed thermal actuation, a performance metric is needed. For the purpose of optimizing the layout of heaters in this paper, a performance cost function is defined as a function of total volume of ice residue [V_{ice}], volume of ice residue for “LE ice 1” [V_{LE1}], volume of ice residue for “LE ice 2” [V_{LE2}], volume of ice residue for “Non-LE ice” [V_{NonLE}], maximum global temperature to the blade structure during de-icing [T_{max_b}], volume of the blade experiencing higher than a certain temperature [30°C here as $V_{T>30}$], and the number of heaters [n_H] representing the cost of the heater network. A simpler analysis has been done for optimizing the layout of a fixed number of

distributed heaters on a small scale blade in Ref. [55]. The cost of the heaters and the ice accumulation in different areas of the blade were not considered in Ref. [55].

In order to compare de-icing performance between different heater layouts, assuming the same amount of thermal power consumption, a quadratic performance cost function J is defined as

$$J = a_1 \left(\frac{V_{ice}}{b_1 V_{ice_i}} \right)^2 + a_2 \left(\frac{V_{LE1}}{b_2 V_{LE1_i}} \right)^2 + a_3 \left(\frac{V_{LE2}}{b_3 V_{LE2_i}} \right)^2 + a_4 \left(\frac{V_{NonLE}}{b_4 V_{NonLE_i}} \right)^2 + a_5 \left(\frac{V_{T>30}}{b_5 V_b} \right)^2 + a_6 \left(\frac{T_{max_b} + 5}{b_6} \right)^2 + a_7 \left(\frac{n_H}{b_7} \right)^2 \quad (6.4)$$

where $X = [V_{ice} \ V_{LE1} \ V_{LE2} \ V_{NonLE} \ V_{T>30} \ T_{max_b} \ n_H]^T$ is the de-icing performance state vector, V_{ice_i} is the initial volume of the ice layer (0.00442 m³), V_{LE1_i} is the initial volume of “LE ice 1” (0.00119 m³), V_{LE2_i} is the initial volume of “LE ice 2” (0.00173 m³), V_{NonLE_i} is the initial volume of “Non-LE ice” (0.00149 m³), and V_b is the volume of the blade segment (0.06422 m³) shown in Figure 6.11. The weighting coefficients a_i and b_i in J are selected as: $a_1 = a_2 = a_6 = 2$, $a_3 = a_4 = 1.5$, $a_5 = 3$, $a_7 = 1$, $b_1 = b_2 = b_3 = b_4 = 0.5$, $b_5 = 0.05$, $b_6 = 40$, and $b_7 = 5$. The volume of “LE ice 1” residue is set to have a higher penalty coefficient than the other ice layers inside the cost function J due to having a higher aerodynamic contribution ($a_2 > a_3$ and $a_2 > a_4$). In the next section, the performance cost function J will be calculated for several heater layouts during one hour of de-icing to quantitatively compare their performances.

6.2.4 De-Icing Performance Comparison for Different Heater Layouts

In this section, the computational modeling of ice melting and de-icing performance comparison is investigated for the different heater layouts described in Section 6.2.2.

A uniform heat flux of $q = 3000$ Watt/m² is applied to the outer surface of the heaters in direct contact with the ice layer. A medium variable air convection is modeled on the blade ($h = 35$ to 25 Watt/(m²·°C)) linearly decreasing from the tip to the root of the blade. Figure 6.12 shows the comparison of J as a function of time for the input heat flux range of 2000 to 5000 Watt/m² applied to a 5-piece heater network in the dice configuration shown in Figure 6.11d. Results show that an input heat flux of $q = 3000$ Watt/m² provides a better de-icing performance for the heat flux range of 2000-5000 Watt/m². Providing more heat is not

necessarily better since it increases the applied thermal stress to the blade structure which results in a higher de-icing cost function J . Similar behavior is also observed for all of the other heater layouts shown in Figure 6.11.

The values of the performance cost function J for different heater layouts at $q = 3000 \text{ Watt/m}^2$ are shown in Figure 6.13 based on Equation (6.4) during one hour of de-icing. These results show that the 5-piece heater in the dice configuration achieves the best overall performance. This is mainly due to providing a more uniform de-icing through out the entire ice layer and applying less thermal stress to the blade structure which will be discussed in the following results of this section.

Figure 6.14 shows the de-icing performance comparison of melting for the total volume of ice residue V_{ice} as percentage of the initial total ice volume V_{ice_i} for different heater layouts using the same amount of thermal power consumption and total heater area A_H during one hour of de-icing. The 5-piece heater in the dice configuration has 13.7% smaller total volume of ice residue on the blade after one hour of de-icing compared to the 1-piece heater layout. Among all of the investigated layouts, 10-piece heater does the best job in de-icing of the total ice volume but it obviously has the highest cost of heaters.

Figure 6.15 shows the volume of “LE ice 1” residue V_{LE_1} as a percentage of the initial volume of “LE ice 1” $V_{LE_{1i}}$ during one hour of de-icing for different heater layouts. The 1-piece heater provides the best de-icing in the “LE ice 1” layer due to having a larger heat source area closer to this region.

Figure 6.16 shows the volume of “LE ice 2” residue V_{LE_2} as a percentage of the initial “LE ice 2” volume $V_{LE_{2i}}$ during one hour of de-icing for different heater layouts. The 1-piece heater also provides the best de-icing performance in this region, fully melting the ice in about 200 seconds after switching on the heater network.

Figure 6.17 shows the volume of “Non-LE ice” residue V_{NonLE} as a percentage of the initial “Non-LE ice” volume V_{NonLE_i} during one hour of de-icing for different heater layouts. The 10-piece heater layout and the 5-piece heater layout in the dice configuration provide a significantly better result in de-icing of this region compared to the other heater layouts. They also provide a more uniform de-icing across the entire ice layer.

Besides minimizing the volume of ice residues in different areas, decreasing the amount of applied

Table 6.2: Quantitative performance cost comparison after one hour of heating at $q = 3000 \text{ Watt/m}^2$ (Percentage reductions for the cost J relative to the 1-piece heater layout is written in the parentheses).

| Heater layout | $V_{ice}(\times 10^{-3} \text{ m}^3)$ | $V_{LE_1}(\times 10^{-4} \text{ m}^3)$ | $V_{LE_2}(\times 10^{-4} \text{ m}^3)$ | $V_{NonLE}(\times 10^{-3} \text{ m}^3)$ |
|----------------------|--|--|--|---|
| 1-piece | 1.46 | 2.80 | 0 | 1.18 |
| 3-piece in one row | 1.71 | 5.25 | 2.45 | 0.94 |
| 5-piece in one row | 1.89 | 4.81 | 1.53 | 1.25 |
| 5-piece in dice | 1.26 | 6.81 | 0.90 | 0.45 |
| 10-piece in two rows | 0.75 | 4.63 | 0.91 | 0.20 |
| Heater layout | $V_{T>30}(\times 10^{-3} \text{ m}^3)$ | $T_{max_b}(\text{°C})$ | J | |
| 1-piece | 1.50 | 35.66 | 7.83 | |
| 3-piece in one row | 1.71 | 48.45 | 10.00 (27.71%) | |
| 5-piece in one row | 1.89 | 74.37 | 16.97 (116.73%) | |
| 5-piece in dice | 0.59 | 42.94 | 7.25 (-7.41%) | |
| 10-piece in two rows | 0.52 | 43.45 | 8.56 (9.32%) | |

thermal stress is another important factor to be considered in the design of distributed active de-icing systems. Figure 6.18 and Figure 6.19 show the time history of the volume of the blade experiencing higher than 30°C , $V_{T>30}$, and the maximum global temperature to the blade structure T_{max_b} for different heater layouts during one hour of de-icing. It is observed that placing more heaters in a single row configuration significantly increases the volume of high-thermal stress regions on the blade structure. Figure 6.19 shows similar behavior, where more heaters in a single row results in a higher maximum global temperature to the blade structure. Hence, a design in which the heaters are distributed in multiple rows instead of a single row reduces the applied thermal stress.

Table 6.2 shows the summary of final-time results for each element of the de-icing performance state vector X as well as the de-icing performance cost function J after one hour of heating for the different layouts. This analysis shows that the best performance is achieved by the 5-piece heater in the dice configuration with 7.41% reduction in the value of J compared to the 1-piece heater layout. However, the 1-piece heater layout provides with the lowest value of T_{max_b} . It is also observed that heaters in multiple-row configurations lead to a lower applied thermal stress and smaller values for $V_{T>30}$.

6.2.5 Sensitivity Study of Other Boundary Conditions

Under real operating conditions, ice geometry and boundary conditions frequently change. In this section, a number of extreme boundary conditions are introduced such as ice covering all around the blade, sunshine input flux to the ice outer surface, no blade surface heating, stationary blade conditions with no convection loss or free convection, and different ambient temperatures. The developed computational method in ANSYS provides the capability of simulating open-loop and closed-loop de-icing under different boundary conditions. In the following examples presented here, top surface of the blade (suction side) is fully covered with glaze ice shown in Figure 6.20, with the same blade thermal conductivity of $K = 1 \text{ Watt}/(\text{m}\cdot^\circ\text{C})$. Figure 6.21 shows the leading edge heater under the ice layer for the 1.5 MW blade tip segment.

Boundary condition 1

A continuous 5-mm film of glaze ice is modeled covering the top surface of the blade tip segment with low heat transfer to represent free convection ($5 \text{ Watt}/\text{m}^2$) in a non-rotating blade, blade surface heating of $3000 \text{ Watt}/\text{m}^2$, and ambient temperature of -5°C . Figure 6.22 shows the ice residue on the blade tip segment at $t = 800 \text{ sec}$. Due to low thermal conductivity of the composite blade, the leading edge heater ($A_H = 0.135 \text{ m}^2$) only melts a portion of ice close to this area. If using this heater across the entire span of the blade (20 segments), total input thermal power on a three bladed wind turbine at constant heat flux of $3000 \text{ Watt}/\text{m}^2$ is approximately 1.6% of the turbine rated power while only melting 20.1% of the total initial volume of ice within 1800 seconds of de-icing. Covering all around the 1.5 MW blade on a three bladed turbine consumes about 19.8% of the rated power, which is very high and not economical to apply. Therefore, localized de-icing on a smaller blade region with accurate ice sensing was recommended in order to significantly reduce the amount of de-icing power consumption.

Boundary condition 2

This Boundary condition is the same as the boundary condition 1 but with the ambient temperature of -30°C . Under this condition, only about 4.8% of the initial volume of ice layer melts at the leading edge area above the leading edge heater after 1800 sec of de-icing.

Boundary condition 3

A continuous 20-mm ice deposit is modeled covering the top surface of the blade with uniform, incoming heat flux of 350 Watt/m^2 to represent sunshine heat flux on a sunny day, no blade rotation, no blade surface heating, and ambient temperature of $-5 \text{ }^\circ\text{C}$. Figure 6.23 shows the modeled sunshine input heat flux into the ice outer surface at all times assumed for boundary conditions 3 and 4 in this section. Figure 6.24 shows the situation of ice melting at different times for this boundary condition.

Boundary condition 4

This boundary condition is the same as the boundary condition 3 but with the ambient temperature of $-30 \text{ }^\circ\text{C}$. Figure 6.25 shows the the volume of ice residue (in percentage of initial ice volume) on the blade tip segment at different times for boundary conditions 3 and 4. It is seen that the sunshine heat flux melts more than 98% of the modeled 20-mm ice layer within half an hour for a stationary blade with no convection loss and blade surface heating for both of these boundary conditions. Figure 6.25 shows the volume of ice residue (in percentage of initial volume of ice) at different times for modeled boundary conditions 3 and 4.

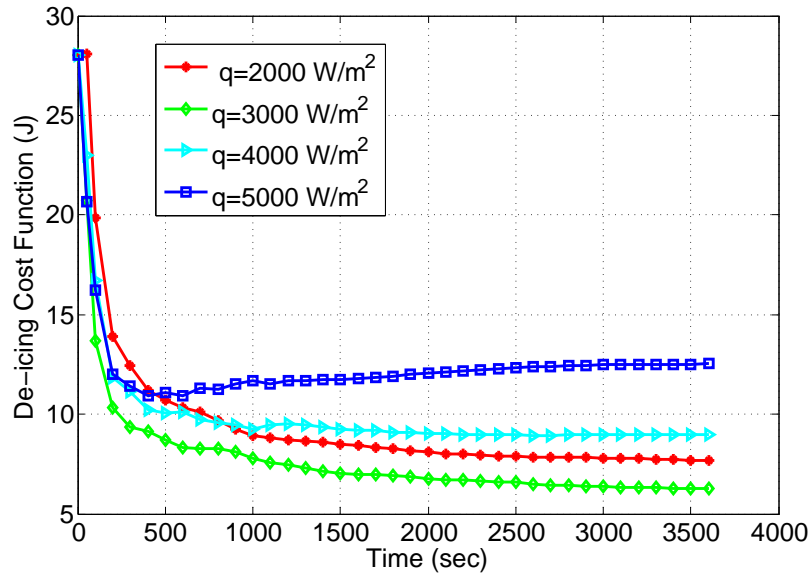


Figure 6.12: Optimizing the magnitude of the uniform heat flux for the 5-piece heater network in the dice configuration. The best de-icing performance is achieved for an input heat flux of $q = 3000 \text{ Watt/m}^2$ assuming a blade conductivity of $K = 1 \text{ Watt/(m}\cdot\text{°C)}$ and linear variation of the convective coefficient of heat transfer from the tip to the root of the modeled blade segment ($h = 25 \text{ Watt/(m}^2\cdot\text{°C)}$ at the root and $h = 35 \text{ Watt/(m}^2\cdot\text{°C)}$ at the tip of the blade segment).

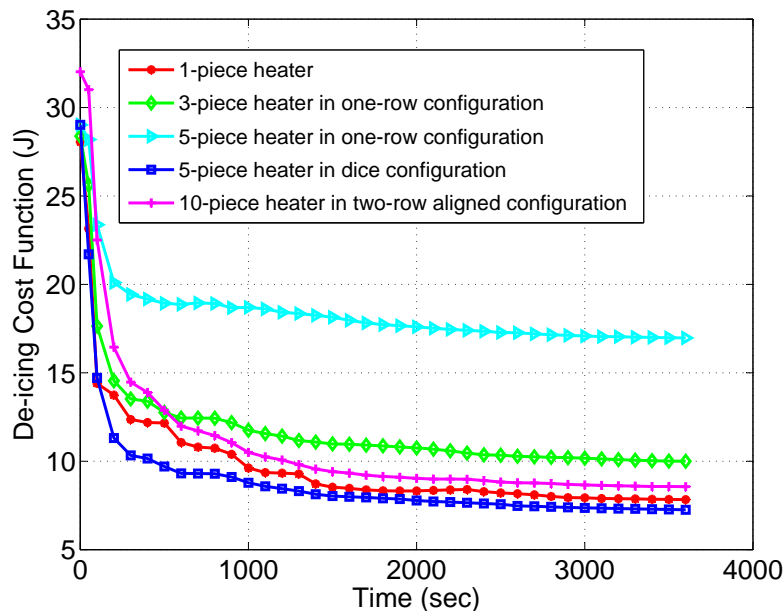


Figure 6.13: De-icing performance cost function vs. time for different heater layouts for $K = 1 \text{ Watt/(m}\cdot\text{°C)}$, $h = 25 - 35 \text{ Watt/(m}^2\cdot\text{°C)}$ from the root to the tip of the blade segment, and $q = 3000 \text{ Watt/m}^2$.

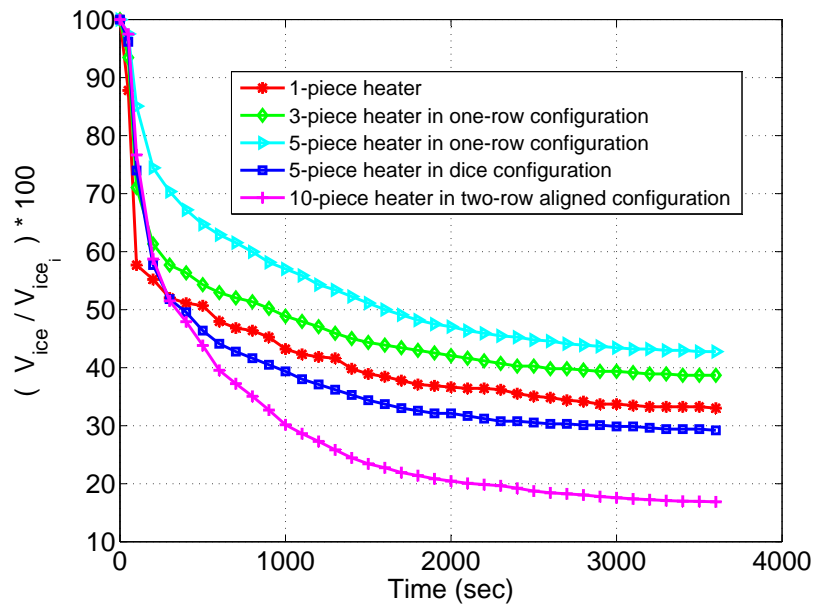


Figure 6.14: Percentage of total volume of ice residue vs. time for different heater layouts for $K = 1 \text{ Watt}/(\text{m}\cdot^{\circ}\text{C})$, $h = 25 - 35 \text{ Watt}/(\text{m}^2\cdot^{\circ}\text{C})$ from the root to the tip of the blade segment, and $q = 3000 \text{ Watt}/\text{m}^2$.

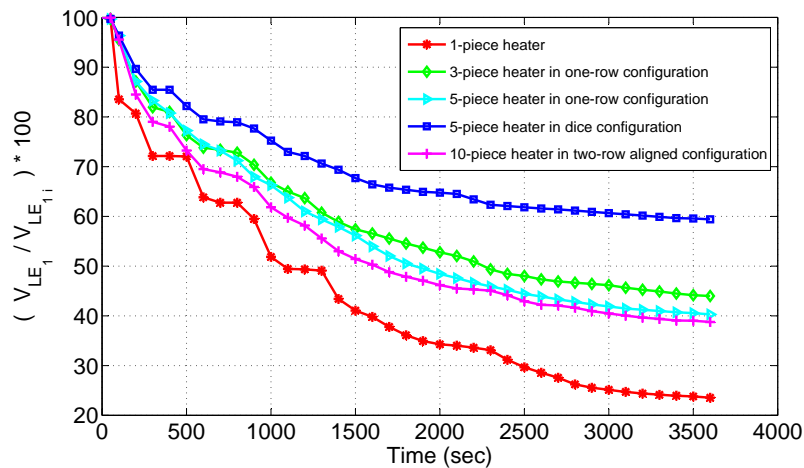


Figure 6.15: Percentage of volume of "LE ice 1" residue vs. time for different heater layouts for $K = 1 \text{ Watt}/(\text{m}\cdot^{\circ}\text{C})$, $h = 25 - 35 \text{ Watt}/(\text{m}^2\cdot^{\circ}\text{C})$ from the root to the tip of the blade segment, and $q = 3000 \text{ Watt}/\text{m}^2$.

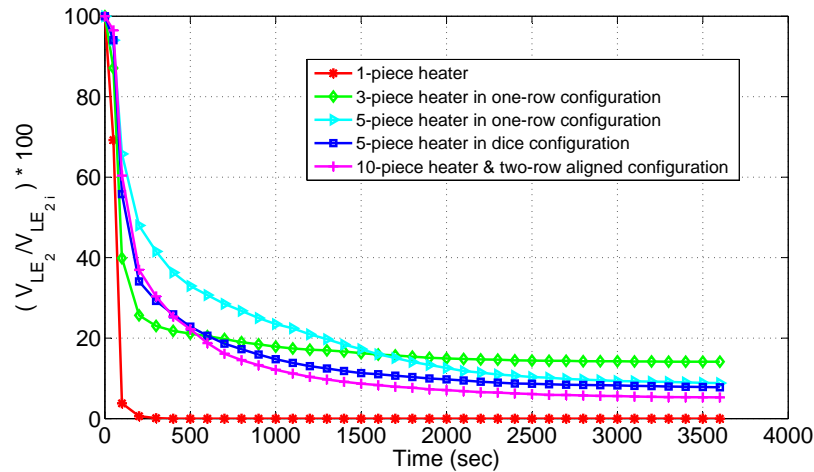


Figure 6.16: Percentage of volume of “LE ice 2” residue vs. time for different heater layouts for $K = 1 \text{ Watt}/(\text{m}\cdot^{\circ}\text{C})$, $h = 25 - 35 \text{ Watt}/(\text{m}^2\cdot^{\circ}\text{C})$ from the root to the tip of the blade segment, and $q = 3000 \text{ Watt}/\text{m}^2$.

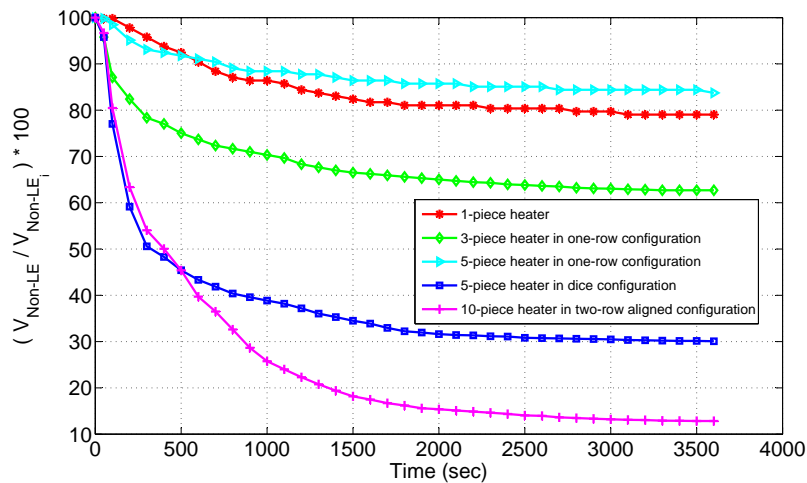


Figure 6.17: Percentage of volume of “Non-LE ice” residue vs. time for different heater layouts for $K = 1 \text{ Watt}/(\text{m}\cdot^{\circ}\text{C})$, $h = 25 - 35 \text{ Watt}/(\text{m}^2\cdot^{\circ}\text{C})$ from the root to the tip of the blade segment, and $q = 3000 \text{ Watt}/\text{m}^2$.

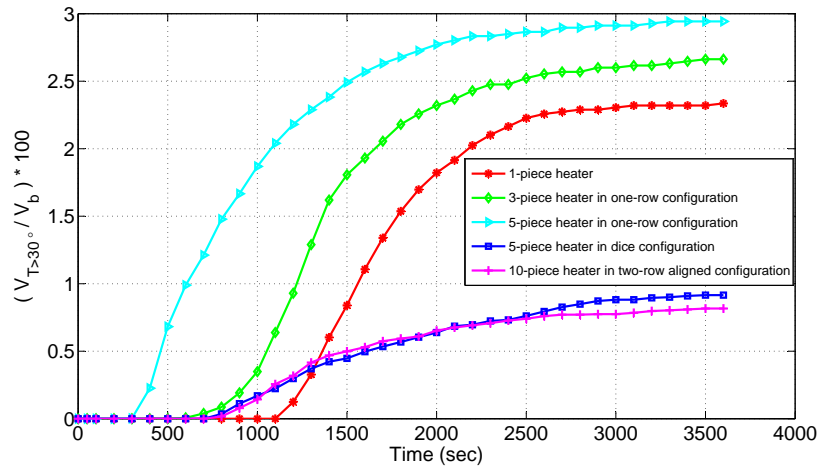


Figure 6.18: Percentage of $V_{T>30}$ vs. time for different heater layouts for $K = 1 \text{ Watt}/(\text{m} \cdot ^\circ\text{C})$, $h = 25 - 35 \text{ Watt}/(\text{m}^2 \cdot ^\circ\text{C})$ from the root to the tip of the blade segment, and $q = 3000 \text{ Watt}/\text{m}^2$.

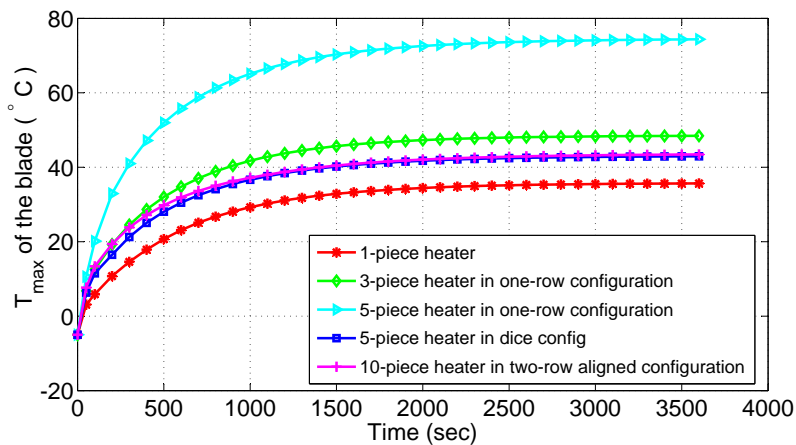


Figure 6.19: T_{max} on the blade vs. time for different heater layouts for $K = 1 \text{ Watt}/(\text{m} \cdot ^\circ\text{C})$, $h = 25 - 35 \text{ Watt}/(\text{m}^2 \cdot ^\circ\text{C})$ from the root to the tip of the blade segment, and $q = 3000 \text{ Watt}/\text{m}^2$.

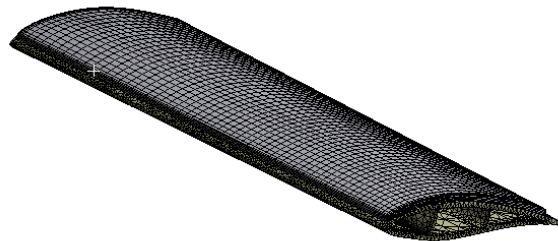


Figure 6.20: Blade tip segment of a 1.5 MW wind turbine blade with 20 mm of uniform glaze ice covering the suction surface of the blade segment.

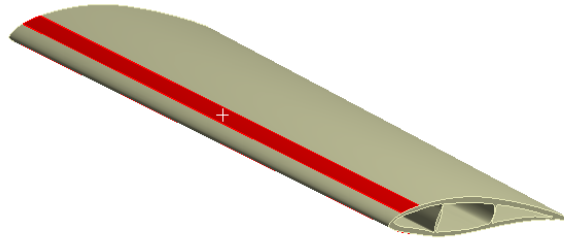


Figure 6.21: A leading edge heater on a 1.5 MW blade tip segment.

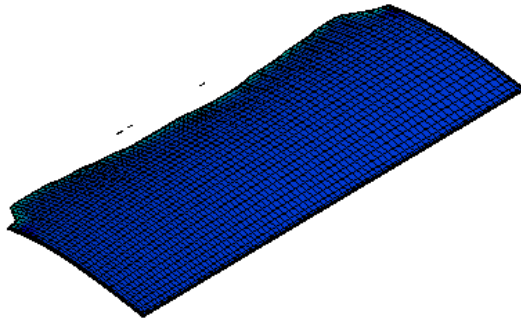


Figure 6.22: Ice residue on the suction surface of the blade tip segment (5-mm uniform glaze ice) for boundary condition 1 after 800 seconds.

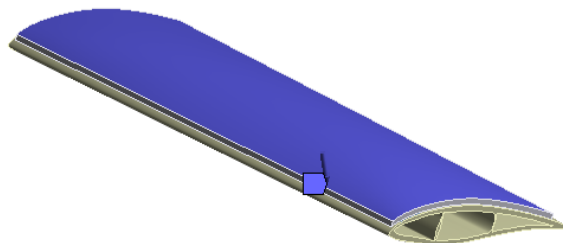


Figure 6.23: Sunshine input heat flux boundary condition applied to the outer surface of the ice.

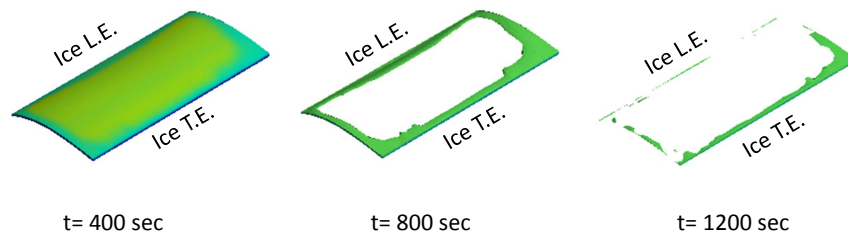


Figure 6.24: Ice residue on the suction surface of the blade tip segment (20-mm uniform glaze ice) for boundary condition 3 representing sunshine with uniform incoming heat flux of 350 Watt/m^2 , no blade rotation, no blade surface heating, and ambient temperature of -5°C .

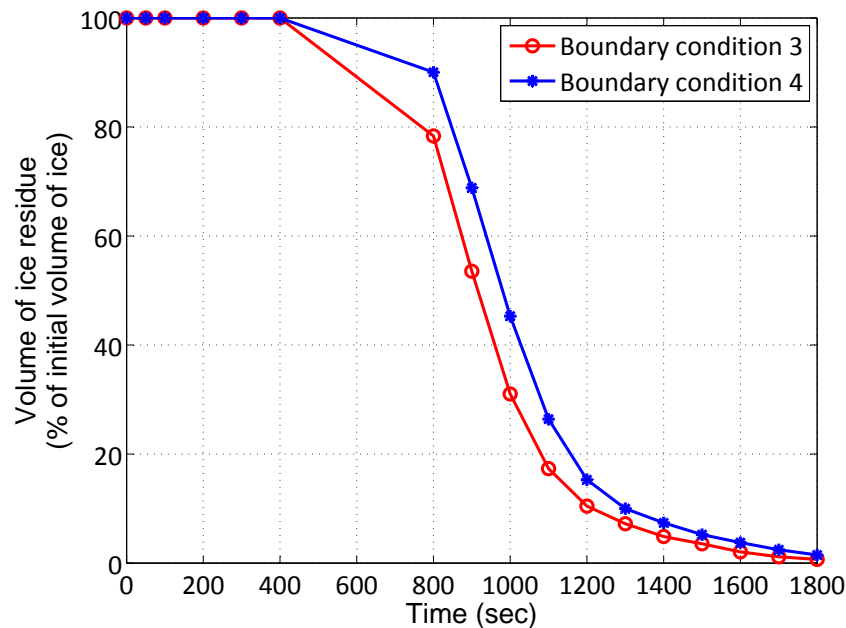


Figure 6.25: Volume of ice residue at different times (20-mm uniform glaze ice) for boundary conditions 3 and 4, representing sunshine with uniform incoming heat flux of 350 Watt/m^2 , no blade rotation, no blade surface heating, and two ambient temperatures of -5°C and -30°C .

Chapter 7

Computational Closed-Loop Controller Design for De-icing Using Distributed Resistive Heaters and Temperature Sensors

This chapter explains the development of an approach for the computational implementation of closed-loop active de-icing on a 1.5 MW rotating blade tip segment using distributed resistive heating and temperature sensing. Optical ice sensing is not simulated here and the computational results presented in this chapter are based on the assumption of known ice location information provided by distributed optical sensors. The presented framework can be used for the simulation of closed-loop de-icing on wind turbines and aerial vehicles. A script-based module was developed in ANSYS-APDL software for implementation of different closed-loop thermal controllers. This module enables the capability of closed-loop de-icing simulations using different distributed thermal actuation scenarios for any number and layout of heaters and temperature sensors. The results are presented for a continuous proportional controller and a pulsed proportional controller. The results show that despite the simplicity of the controller scheme, its de-icing time is about 4 times faster than a constant heat flux thermal actuation with the same amount of total energy consumption. In addition, the closed-loop controllers reduce the maximum temperature and the volume of high-temperature regions on the blade structure. Further, the computational model was employed to optimize the de-icing response based on surrogate modeling (a computational model for engineering design). De-icing response is quantitatively characterized by calculating a de-icing performance cost function for different values of controller gains. The Multi-Objective Genetic Algorithm (MOGA) optimization tool is used in ANSYS for calculation of the optimal values of controller parameters for a network of distributed resistive heaters on the blade. Different surrogate models are used to enhance the computational efficiency

of this approach. The results showed that larger controller gains need to be selected for those heaters that are closer to the blade leading edge due to larger amount of convective heat loss in that region. Furthermore, analysis of existence of a faulty temperature sensor in a distributed network of heaters and temperature sensors showed that closed-loop de-icing is robust to a limited number of known faulty sensors.

The remainder of this chapter is organized as follows. In Section 7.2, the geometry of the modeled ice layer is described. In Section 7.3, implementation of the closed-loop thermal actuation for de-icing is explained. De-icing performance metric for closed-loop is explained in Section 6.2.3. In Section 7.3.2, the comparison of computational results is presented between a closed-loop proportional controller and a constant heat flux actuation for 1-heater configuration installed close to the blade leading edge area. In Section 7.4, the results of gain optimization are shown for a 5-piece heater configuration with a proportional controller. In Section 7.5, computational simulation results of a known faulty sensor in a distributed network of heaters and sensors are discussed.

7.1 Model Assumptions

In the computational results discussed in this dissertation, ice and water shed-off models are not included in the computational model due to extreme complexity and it is assumed that water stays on the blade after ice melting. The computational model considers phase change from ice to water on all of the elements in the model. The computational model switches to the physical properties of ice elements to water at 0°C including density, thermal conductivity, and specific heat according to Figure 1.5. Since ice melting starts from the inner ice surface (surface in direct contact with blade surface) toward outer ice surface (surface in contact with air), removing the water elements after melting (between blade surface and ice) blocks the heat transfer from heaters to the outer surface of ice that happens in the process of ice melting. Therefore water element removing is not a correct modeling approach unless water shedding is modeled meaning that the remaining ice finite elements need to be geometrically shifted to the surface of the blade after each time-step to remain physical element contact between blade surface and remaining ice layer. This can add an extreme amount of complexity and computational time to the model, if possible at all and therefore is not considered in the model discussed in this chapter.

7.2 Non-Uniform Ice Geometry and Boundary Conditions

For the following analysis of computational closed-loop de-icing in this chapter, same ice geometry and boundary conditions are used for a rotating blade segment of a 1.5 MW wind turbine as the model described in section 6.2.1 in chapter 6 with tip speed ratio of 6.8, $u_w=12$ m/sec, $\omega = 22.2$ rpm, blade radius of 35.25 m and ambient temperature of -5 °C.

7.3 Closed-Loop Simulations of De-icing

In this section, computational simulations of de-icing in ANSYS are explained for a 1-piece heater layout using different constant and closed-loop de-icing based on a point temperature measurement located at the tip of the blade for the modeled geometry discussed in section 7.2. A script-based module is developed in ANSYS-APDL for computational closed-loop simulations. This controller module communicates with the finite-element solver in ANSYS. The temperature distribution on the blade structure at each time step depends on the input heat flux at the previous time step. The heat flux is updated with sensing frequency f and then the finite element solver restarts by using the degree of freedom (DOF) information and the state variable in the previous time step as initial conditions for subsequent computations at the next time step. The model is fully parameterized to be used in post-processing for further optimization studies used to find the best candidates for the controller gains required for each heater. We utilized ANSYS programming design language (APDL) for calculating the volume of ice residue, maximum blade temperature, and volume of high temperature regions as a function of time. In these modules, these parameters are calculated first for each element and later are integrated for the volume of interest during the closed-loop simulations. Figure 7.1 shows a schematic block diagram of the computational closed-loop de-icing simulation based on temperature measurement in ANSYS. In section 7.3.2, this closed-loop frame work is applied for the computational simulations of de-icing using proportional control and its performance will be compared with constant heat flux thermal actuation.

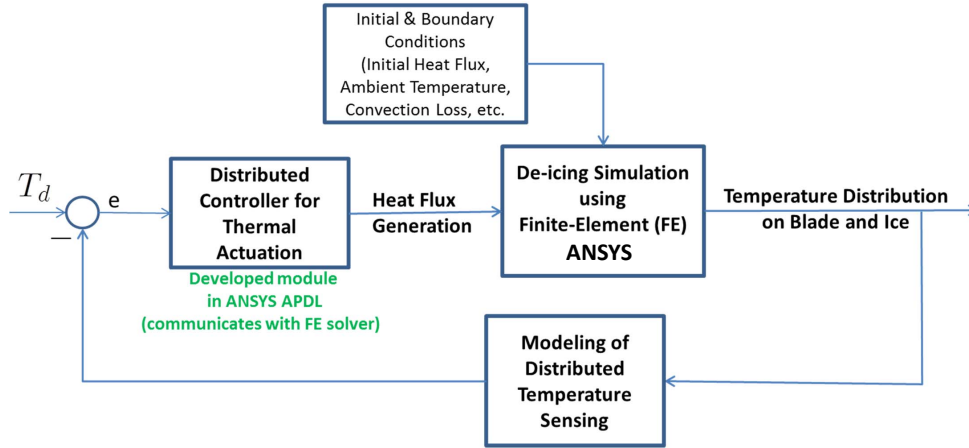


Figure 7.1: Block diagram of closed-loop de-icing simulations in ANSYS.

7.3.1 De-icing Performance Metric for Controller Optimization

In order to quantitatively evaluate the de-icing performance of distributed thermal actuation, we determine a performance cost as a function of total volume of ice residue $[V_{ice}]$, volume of ice residue for “LE ice 1” $[V_{LE_1}]$, volume of ice residue for “LE ice 2” $[V_{LE_2}]$, volume of ice residue for “Non-LE ice” $[V_{NonLE}]$, maximum global temperature to the blade structure during de-icing $[T_{max_b}]$, and volume of the blade experiencing higher than a certain temperature $[5^\circ\text{C}$ here as $V_{T>5}]$. A simpler analysis has been done for optimizing the layout of a fixed number of distributed heaters on a small scale blade using constant heat flux [55]. The cost of the heaters and the ice accumulation in different areas of the blade were not considered in [55].

In order to compare de-icing performance, a quadratic performance cost function J is defined as

$$J = a_1 \left(\frac{V_{ice}}{b_1 V_{ice_i}} \right)^2 + a_2 \left(\frac{V_{LE_1}}{b_2 V_{LE_{1i}}} \right)^2 + a_3 \left(\frac{V_{LE_2}}{b_3 V_{LE_{2i}}} \right)^2 + a_4 \left(\frac{V_{NonLE}}{b_4 V_{NonLE_i}} \right)^2 + a_5 \left(\frac{V_{T>T_0}}{b_5 V_b} \right)^2 + a_6 \left(\frac{T_{max_b} - T_d}{b_6} \right)^2 \quad (7.1)$$

where $X = [V_{ice} \ V_{LE_1} \ V_{LE_2} \ V_{NonLE} \ V_{T>T_0} \ T_{max_b}]^T$ is the de-icing performance state vector and J and each of these 6 values vary with time. V_{ice_i} is the initial volume of the ice layer, $V_{LE_{1i}}$ is the initial volume of “LE ice 1”, $V_{LE_{2i}}$ is the initial volume of “LE ice 2”, V_{NonLE_i} is the initial volume of “Non-LE ice”, and V_b is

the volume of the blade segment shown in Figure 6.7. In (7.1), power consumption is implicitly included in the cost function J (function of input heat flux) to avoid zero input power solution while minimizing J for the optimization. In addition, including power consumption in J could decrease and slow down the process of de-icing on the blade when solving the computational optimization by minimizing thermal energy consumption and hence input heat energy into the heaters. However, enforcing an upper-bound for the initial magnitude of heat flux can keep the total energy consumption bounded within a reasonable range in closed-loop thermal actuation.

The weighting coefficients a_j and b_j in J are selected as $a_1 = a_2 = a_5 = 2$, $a_3 = 1.5$, $a_4 = 1$, $a_6 = 4$, $b_1 = b_2 = b_3 = b_4 = 0.5$, $b_5 = 0.05$, and $b_6 = 10$. Weighting coefficients of performance cost function J for the closed-loop de-icing in this section are tuned based on closed-loop de-icing response and are different than the weighting coefficients defined in section 6.2.3 of chapter 6 for constant thermal actuation. For example, thermal stress to the blade structure in closed-loop is much smaller compared to constant actuation explained in chapter 6. The volume of “LE ice 1” residue is set to have a higher penalty coefficient than the other ice layers in the cost function J due to having a higher aerodynamic contribution ($a_2 > a_3$ and $a_2 > a_4$). b_j coefficients normalize each term inside the performance cost function J in order to create a similar order of magnitude for different terms in J . For instance, in this defined cost function, if no ice melts during the process ($V_{ice} = V_{ice_i}$), the first quadratic term in the cost function J without a_1 coefficient $\left(\frac{V_{ice}}{b_1 V_{ice_i}}\right)^2$ equals to 4. Similarly, if T_{max_b} is 20 °C larger than the desired blade temperature (T_d) during de-icing, the sixth quadratic term without a_6 coefficient, $\left(\frac{T_{max_b} - T_d}{b_6}\right)^2$, also equals to 4. Thus, the a_j coefficients can be separately tuned to change the penalty of each term in J . For example, increasing the a_1 coefficient leads to a higher value of J due to the volume of ice residue on the blade while increasing a_6 creates a higher penalty for the maximum applied temperature to the blade structure during de-icing. In the next section, the performance cost function J is calculated for different constant and closed loop thermal actuation strategies for a 1-piece heater layout close to the leading edge area of the blade, and de-icing performance will be compared quantitatively.

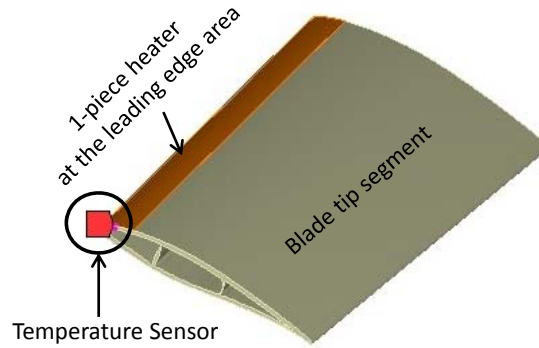


Figure 7.2: 1-piece heater configuration with an area of 0.205 m^2 with an installed temperature sensor at the tip of the blade under the middle of “LE ice 2”.

7.3.2 Proportional Closed-Loop versus Constant Flux De-icing

In this section, de-icing performance of two proportional closed-loop controllers versus constant heat flux is investigated for a 1-piece heater layout attached near to the leading edge area of the blade and their performance will be compared.

Figure 7.2 shows a 1-piece heater attached on the blade suction side close to the leading edge area with an installed temperature sensor attached to the tip of blade outer segment. This temperature sensor directly contacts the suction surface of the blade structure in order to achieve the desired temperature through closed-loop thermal actuation. The blade tip section has the highest rotational speed, largest value of convective coefficient of heat transfer (Figure 6.10), and highest probability of ice accumulation compared to other regions. The performance of closed-loop thermal actuation also depends on the location of temperature sensors, their distance from resistive heaters, and the blade thermal conductivity. Heat flux transport from heat sources through the blade structure happens faster for higher values of blade thermal conductivity. Placing temperature sensors in areas where heat flux does not reach very well can significantly degrade the efficiency of closed-loop de-icing. Therefore the location of sensors needs to be appropriately selected based on the type of heater layout used for de-icing.

Two different types of proportional controllers are applied: Low Intensity Continuous Proportional

Controller (LICPC) and high intensity pulsed proportional controller (HIPPC).

The applied input heat flux for the LICPC scheme based on temperature measurement at the blade tip is

$$q = k_{pc} (T_d - T_1) \quad (7.2)$$

where q is the input heat flux to the heater in Watt/m^2 , k_{pc} is gain of the proportional controller, T_d is desired temperature of melting, and T_1 is the measured temperature at the tip of the blade from temperature sensor 1.

The applied input heat flux for the HIPPC scheme based on temperature measurement at the blade tip is calculated as

$$q = i_c k_{pp} (T_d - T_1) \quad (7.3)$$

where i_c is the controller switching index which switches between 0 and 1 with a frequency equal to the frequency of actuation, and $k_{pp} = \alpha k_{pc}$ ($\alpha = 2$ in Figures 7.3-7.7).

A code written in ANSYS is used for implementation of closed-loop controllers. In addition to closed-loop control, for a comparative study, open-loop control with two constant heat fluxes are investigated: 3000 Watt/m^2 (selected as a suitable initial flux value estimation at the tip of a 1.5 MW wind turbine) and 763 Watt/m^2 which is equal to the average input heat flux of the LICPC applied using $k_{pc} \text{ Watt/(m}^2 \cdot \text{°C)}$ and $T_d = 3^\circ\text{C}$.

Figure 7.3 shows four different applied input heat fluxes to the 1-piece heater layout. Figure 7.4 shows temperature sensor outputs for the continuous and the pulsed proportional controllers applied to the 1-piece heater. Unlike constant actuation, closed-loop actuation ultimately provides a balance between input thermal energy and energy loss due to convection, and the temperature ultimately reaches a steady-state value.

Figure 7.5 shows the maximum temperature on the blade (T_{max_b}) versus time for the different applied heat flux signals. The initial ambient temperature before switching on the thermal actuation for all cases is defined as $T_0 = -5^\circ\text{C}$. It is seen in Figure 7.3 that the constant heat flux of 3000 Watt/m^2 overheats the blade and increases T_{max_b} rapidly as a function of time and therefore is a poor thermal actuation strategy

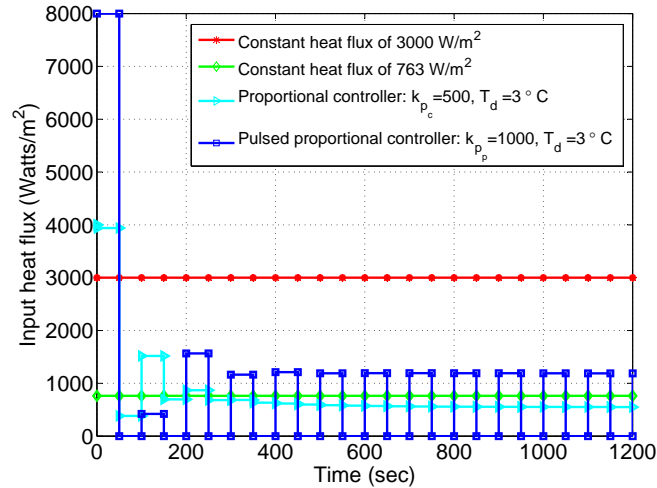


Figure 7.3: Input heat flux of different open-loop and closed-loop thermal controllers for a 1-piece heater installed close to the leading edge area of a 1.5 MW wind turbine blade.

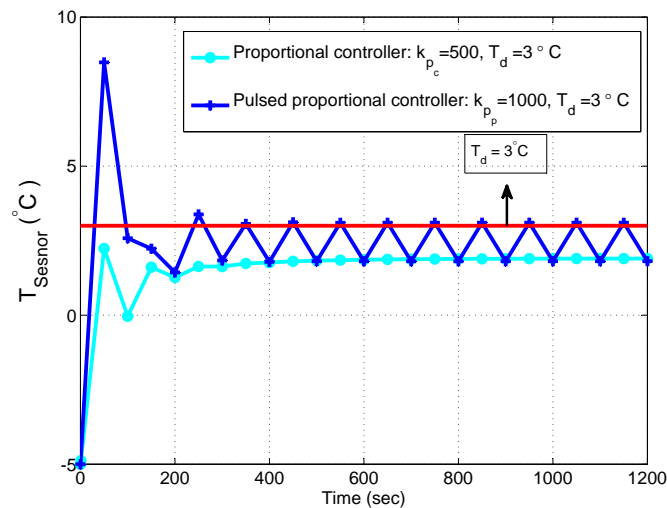


Figure 7.4: Temperature sensor output when using the same thermal controllers as in Figure 7.3, for a 1-piece heater installed close to the leading edge area of a 1.5 MW wind turbine blade.

because it consumes much more energy than required and monotonically increases the maximum applied temperature to the blade structure. The continuous proportional controller quickly approaches the desired temperature $T_d = 3\text{ }^{\circ}\text{C}$ in about 200 seconds and keeps the temperature of the blade within $0.15\text{ }^{\circ}\text{C}$ of T_d after 200 seconds. Similarly, the pulsed proportional controller quickly approaches the desired temperature of melting within 200 seconds and also switches on and off with the update frequency of 0.02 Hz. The

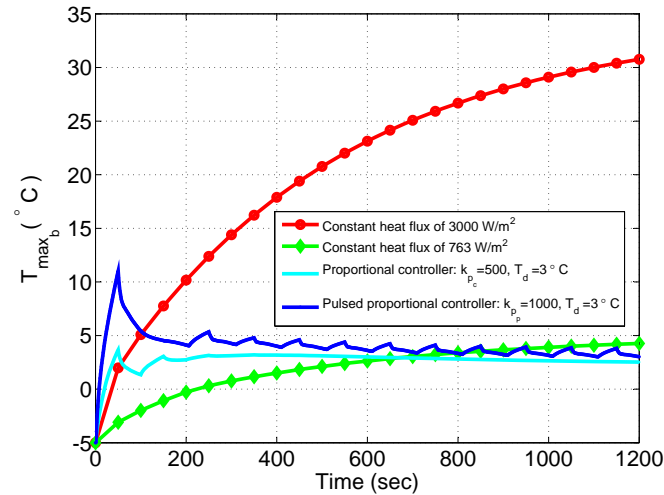


Figure 7.5: Maximum blade temperature T_{max_b} when using the same thermal controllers as in Figure 7.3, for a 1-piece heater installed close to the leading edge area of a 1.5 MW wind turbine blade.

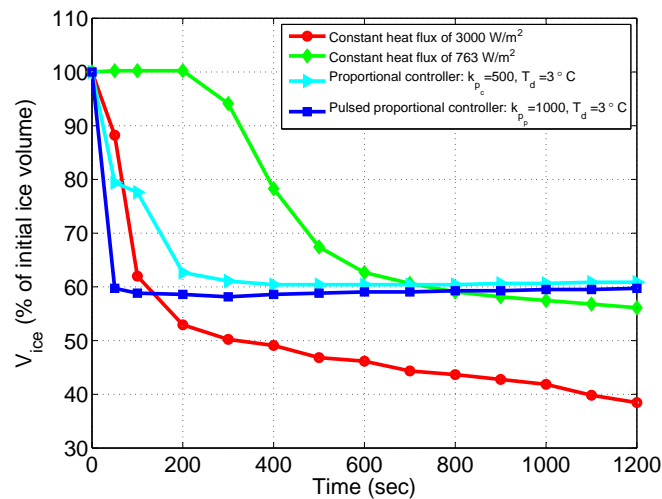


Figure 7.6: Volume of ice/water residue when using the same thermal controllers as in Figure 7.3, for a 1-piece heater installed close to the leading edge area of a 1.5 MW wind turbine blade.

periodic temperature response of this controller can be seen in Figure 7.5 which is because of periodic heating and cooling of the blade structure produced by the periodic actuation after reaching the energy balance between input thermal energy and heat loss due to convection. The magnitude of the temperature peak during the first 50 seconds of the simulation for the pulsed controller is about twice that of the peak for the continuous proportional controller, because the k_{pp} gain for the pulsed controller is two times the k_{pc}

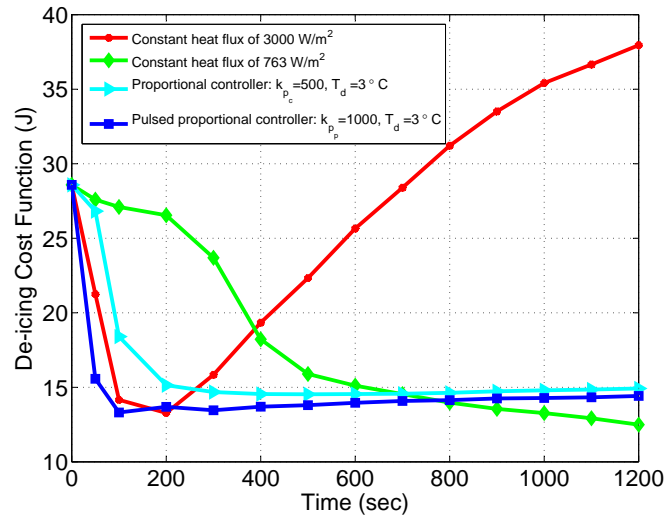


Figure 7.7: De-icing performance cost function for the same thermal controllers as in Figure 7.3, for a 1-piece heater installed close to the leading edge area of a 1.5 MW wind turbine blade.

gain of the continuous controller.

Figure 7.6 shows the total volume of ice residue (V_{ice}) as a percentage of initial volume of ice on the blade segment versus time for different actuation strategies. Although a constant input heat flux of 3000 Watt/m² melts a larger volume of ice (melting 60% of the volume after 1200 seconds, it consumes about 4 times more energy and applies much higher thermal stress to the blade. In general, a constant actuation with similar de-icing time as a proportional controller consumes much larger power without the capability of reducing the temperature error between actual and desired temperatures. It is also observed in Figure 7.6 that constant heat flux actuation with the same energy consumption as the proportional controller ultimately achieves the same amount of ice melting, but at a much slower rate. The slower rate of ice melting for this constant heat flux causes a larger loss of aerodynamic power generation over time and therefore is not as effective. The major drawback of open-loop constant heat flux actuation is the inability to adjust the input thermal energy for de-icing under variable conditions in wind speed, blade angular velocity, and ambient temperature.

Figure 7.7 shows the values of de-icing cost function J defined in (7.1) for the different actuation strategies. It is seen that the value of J using open-loop control with a constant heat flux of 3000 Watt/m²

significantly increases after $t = 200$ seconds due to an increasing in T_{max} . High intensity pulsed thermal actuation slightly improves ice melting but relatively increases the amount of applied thermal stress to the blade structure during de-icing.

Figure 7.8 shows the solution of temperature distribution in the ice/water layer at different times after switching on the applied thermal actuation for the closed-loop continuous proportional controller with $K_p = 500 \text{ Watt}/(\text{m}^2 \cdot ^\circ\text{C})$, and Figure 7.9 shows the solution for the constant heat flux of $763 \text{ Watt}/\text{m}^2$. Those regions with higher than 0°C show that the ice has been melted and physical characteristics of glaze ice (thermal capacity and thermal conductivity) in those regions have been substituted with water. For both cases of constant and closed-loop simulation at all times, it is seen that ice at the tip of the blade experiences slightly lower temperatures due to existence of higher amount of convection. The results of ice temperature

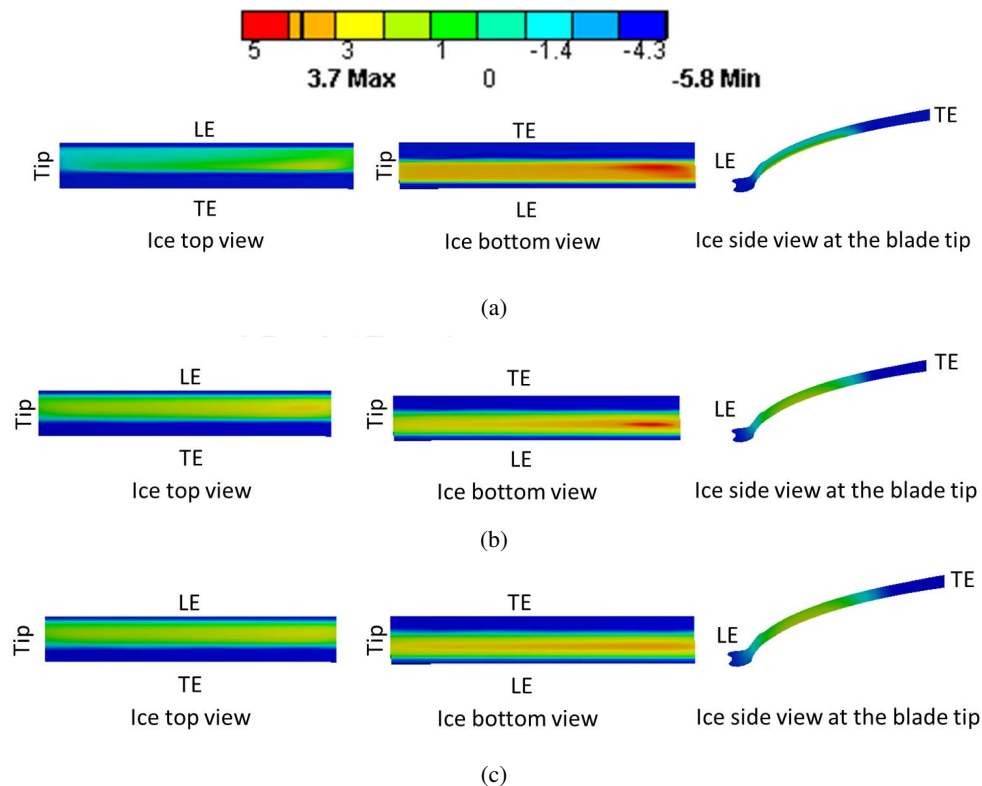


Figure 7.8: Different views of ice temperature distribution for 1-piece heater using proportional closed-loop thermal actuation with $K_p = 500 \text{ Watt}/(\text{m}^2 \cdot ^\circ\text{C})$, $T_d = 3^\circ\text{C}$, and $f = 0.02 \text{ Hz}$. “LE” represents the leading edge of the ice layer and “TE” is the trailing edge of the ice layer shown in different views. (a) $t = 50$ seconds. (b) $t = 500$ seconds. (c) $t = 1200$ seconds.

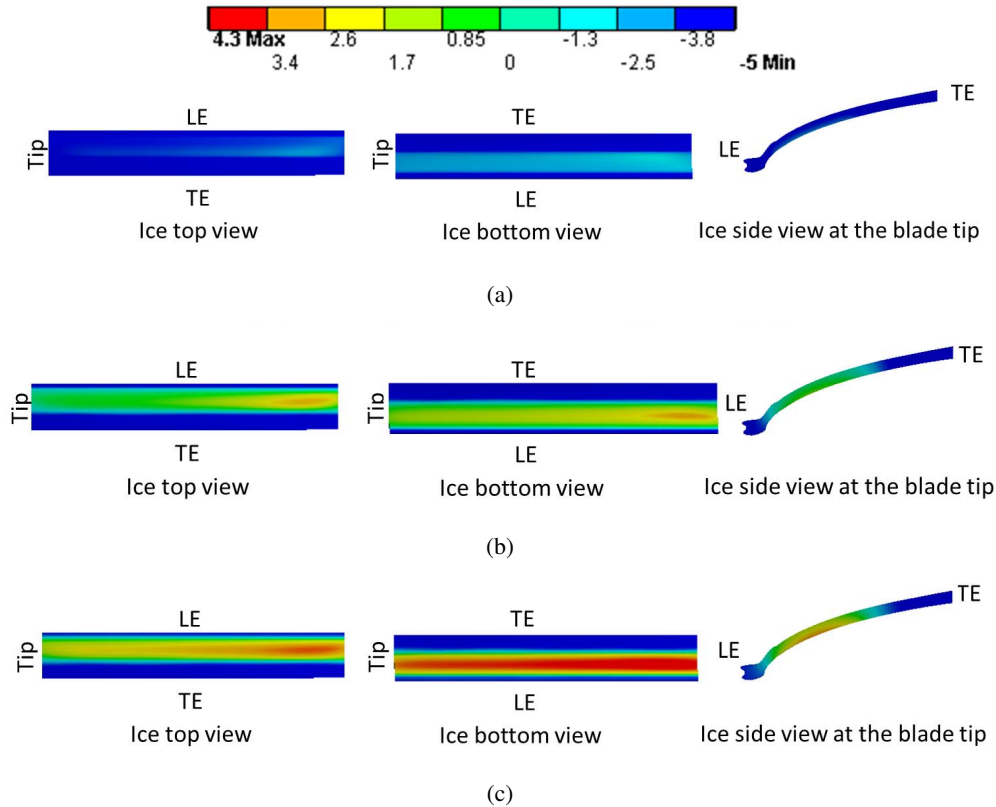


Figure 7.9: Different views of ice/water temperature distribution for 1-piece heater using constant heat flux of $q = 763 \text{ Watt/m}^2$. “LE” represents the leading edge of the ice layer and “TE” is the trailing edge of the ice layer shown in different views. (a) $t = 50$ seconds. (b) $t = 500$ seconds. (c) $t = 1200$ seconds.

distribution using the applied proportional continuous controller (Figure 7.8) confirms successful control of applied heat flux in order to maintain the temperature close to the desired temperature. It is seen in Figure 7.8 that a higher temperature region on the ice layer is observed toward the root of the blade segment at $t = 500$ seconds which has been mitigated at a later time of 1200 seconds by means of the closed-loop thermal controller, while constant thermal actuation monotonically increases the temperature on the ice layer (Figure 7.9) since there is no mechanism of reducing the input heat flux as temperature increases.

In the next section, de-icing closed-loop simulations will be shown for a distributed network of heaters and temperature sensors and the optimization of the controller gains of each individual heaters will be discussed for a 5-piece heater layout.

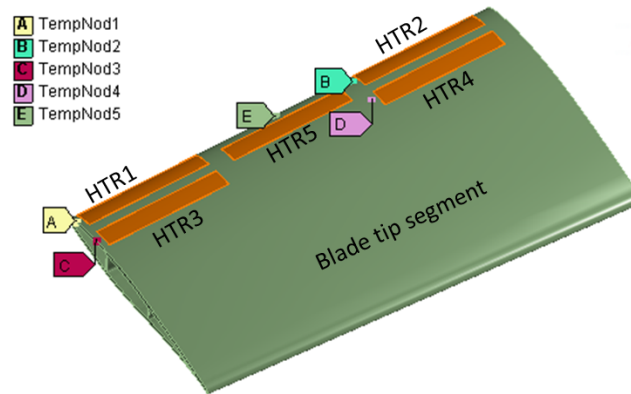


Figure 7.10: 5-piece heater configuration with installed temperature sensors at different locations on the blade outer segment.

7.4 Controller Gain Optimization for a Distributed Network of Heaters

On larger wind turbines, ice accumulation is usually more distributed on the blade structure. In this situation, it is beneficial to use distributed resistive heaters to target a larger spatial region for de-icing. However, using the same controller gains for different heaters is not always optimal in a distributed network. Optimal gain values depend on the amount of convection heat loss (a function of location on the blade), heater layout, ice geometry, blade thermal conductivity, and type of the controller scheme. In this section, optimization of the controller gains is investigated for a 5-piece heater network in the configuration shown in Figure 7.10. It is assumed that each heater has its own independent actuation signal by using the information from one adjacent temperature sensor. It is also assumed that there is no communication between heaters, and the only information accessible to all of the heaters is the temperature measurement of surrounding sensors at each time step, which can be used in the case of a known faulty sensor in the network.

Different methods of “response surface optimization” in ANSYS are used in order to optimize the individual gains of the proportional controllers k_{p_1} through k_{p_5} as well as a unified T_d for the entire network (6 parameters in total for continuous proportional controller in the 5-piece heater layout).

The main objective is to minimize the de-icing performance cost function at different times (or the integral of the cost function over time) subjected to controller gains as design variables. “ANSYS Design Exploration Module” is used to solve the optimization problem.

The mathematical constrained optimization formulation is

$$\begin{aligned}
 & \underset{T_d, k_{p_i}, i=1, \dots, 5}{\text{minimize}} && \int_0^{t_f} J dt \\
 & \text{subject to} && 1000 \leq q_{i_0} \leq 5000 \\
 & && 100 \leq k_{p_i} \leq 750, i = 1, \dots, 5 \\
 & && 0 \leq T_d \leq 15
 \end{aligned} \tag{7.4}$$

where $q_{i_0} = k_{p_i}(T_d - T_{amb})$, k_{p_i} is the proportional gain of the controller for i^{th} heater in the network, T_d is the desired temperature of melting, $T_{amb} = -5^\circ\text{C}$ is the ambient temperature of the atmosphere, and $t_f = 1200$ sec. The initial value of the input heat flux q_{i_0} is constrained on each thermal resistor in the network is to be between 1000 to 5000 Watt/m².

In order to solve the optimization problem described above, the Genetic Algorithm (GA) tool in ANSYS is used, which is considered a heuristic approach that does not require calculation of gradients and therefore has fewer convergence issues. Moreover, GA provides the global optimal solution and the optimization appears to be insensitive to the assumed initial conditions. However, GA requires large number of function evaluations of the objective function which amounts to a finite element simulation for each function evaluation. Typical GA optimization requires 10^3 to 10^9 simulations which is computationally very expensive. Surrogate modeling or meta-modeling was found to be very effective in simulation based optimization [44] as it replaces the computationally complex finite element analysis with a low-cost analytical approximation known as response surface approximation. In this analysis, the Multi-Objective Genetic Algorithm (MOGA) module is used in ANSYS which supports multiple objectives and constraints and aims at finding the global optimum [1].

In order to incorporate the response surface approximation, first the function is trained using computational experiments and then the appropriate “response surface” approximation is fitted to train the function. Selecting the training points is critical in the accuracy of the results and should be done with attention.

Methods of “Design of Experiments” (DOE) in ANSYS use mathematical procedures to find and select the training points. The Latin Hypercube Sampling (LHS) technique is an automated and robust way

to distribute the training points throughout the design space effectively. “LHS is a Monte Carlo simulation method that is more advanced and efficient than the Monte Carlo sampling technique. LHS has a ‘sampling memory’, meaning it avoids repeating samples. It also forces the tails of a distribution to participate in the sampling process” [1]. DOE is the most time consuming step in the process of computational optimization, where 45 simulations are performed based on the input generated by LHS to provide the desired output associated with each gain factor combination. Then, different methods of response surface approximation are used in the optimization. For this problem, the computational training took about 48-hours on a Pentium computer with an Intel Core i-5 2400 CPU at 3.1 GHz.

After computational training, different methods of curve fitting in ANSYS based on the sampled design points, were used including standard response surface-full second order polynomial, neural network, Non-Parametric Regression (NPR), and kriging. “Standard response surface using a second order polynomial is a statistical methodology that utilizes the relationship between two or more quantitative variables so that one dependent variable can be estimated from the others. Neural network is a mathematical technique based on the natural neural network in the human brain. It generally works better when number of design points and samples are higher [1].” The Kriging method passes through all the design points and therefore it shows strong “Goodness of Fit”. NPR algorithm is a type of regression analysis and uses a narrow envelope around the true output surface to capture all the possible training points and therefore it is recommended for highly noisy responses.

Table 7.1 shows the summary of the computed optimal value of the gains of the proportional controller for the 5-piece heater configuration and the modeled ice geometry shown in Figure 7.10 using the different response surface optimization techniques. These results are based on minimization of the cost function in (6.4) and (7.4).

It is seen in Table 7.1 that the neural network method leads to the lowest value of the cost function $\int_0^{t_f} J dt$ and standard 2nd order polynomial achieves the second best value. These results confirm that higher proportional gain values need to be selected for “HTR1” and “HTR3” (Figure 7.10) close to the tip of the blade due to higher blade angular velocity and higher convective heat loss in that region.

Table 7.1: Optimal values of proportional controller parameters for distributed heaters in 5-piece configuration calculated using different “response surface” curve-fitting methods in ANSYS.

| Method | k_{p_1} | k_{p_2} | k_{p_3} | k_{p_4} | k_{p_5} | $T_d(^{\circ}\text{C})$ | $V_{ice}(t_f)(\text{m}^3)$ | $T_{max_b}(^{\circ}\text{C})$ | $\frac{\int_0^{t_f} J dt}{t_f}$ |
|----------------|-----------|-----------|-----------|-----------|-----------|-------------------------|----------------------------|-------------------------------|---------------------------------|
| Polynomial | 540.56 | 352.78 | 410.56 | 367.22 | 237.22 | 3.63 | 1.55×10^{-3} | 10.12 | 35.15 |
| Neural network | 387.63 | 337.73 | 355.33 | 351.85 | 197.24 | 3.50 | 1.73×10^{-3} | 9.41 | 35.02 |
| NPR | 551.49 | 447.69 | 452.63 | 405.65 | 386.75 | 4.76 | 1.60×10^{-3} | 14.42 | 38.63 |
| Kriging | 615.78 | 488.17 | 574.77 | 357.41 | 303.64 | 2.18 | 1.70×10^{-3} | 9.73 | 36.53 |

Overall, different curve-fitting techniques provide similar results in optimizing the controller parameters in a distributed network of 5 heaters.

7.5 Analysis of a Known Faulty Temperature Sensor in the Network

As mentioned earlier, one of the main benefits of distributed heaters for de-icing is that a larger area of de-icing on the blade is covered. However, a distributed network of heaters for de-icing has the potential capability of reducing the total amount of energy consumption by dedicating a smaller blade region to each heater and therefore faster diffusion of the generated heat flux into the blade and ice structures especially for a blade with lower thermal conductivity. In a distributed network of sensors and actuators, unlike a single sensor and actuator, the entire effectiveness of the system does not fully shut down by occurring a single fault in the network, because of the existence of the other redundant players in the network. However, naturally the possibility of fault occurrence becomes higher as the number of sensors and actuators increases. Therefore, it is important to investigate the performance of the distributed network and to evaluate its effectiveness under different faulty scenarios. Before dealing with faults in the network, faulty agents should be accurately detected. The focus of this section is not on fault detection; however the performance of the closed-loop controller will be investigated under existence of a known and pre-detected faulty temperature sensor for 5-piece heater configuration.

Figure 7.11 shows the output of the temperature sensors with no faults while a proportional controller with $k_p = 500 \text{ Watt}/(\text{m}^2 \cdot ^{\circ}\text{C})$ and $T_d = 3^{\circ}\text{C}$ is applied to all of the heaters in 5-piece heater layout shown in Figure 7.10.

A faulty scenario is created in temperature sensor 5 to investigate the effect of this fault on the overall

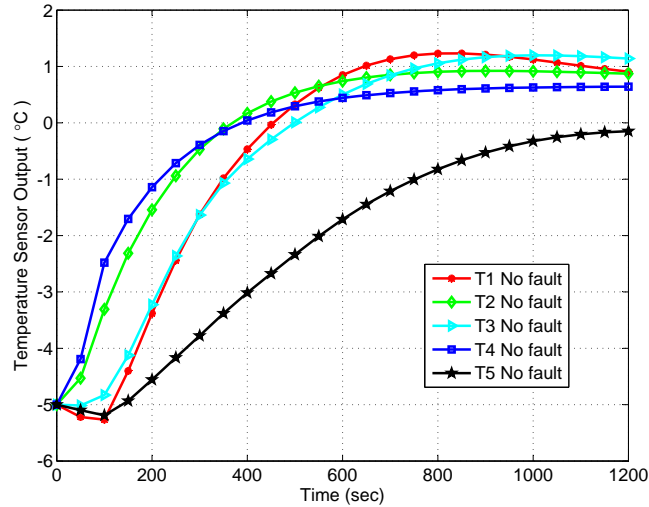


Figure 7.11: Temperature sensor outputs with no faulty sensors in the network and a proportional controller with $k_p = 500 \text{ Watt}/(\text{m}^2 \cdot ^\circ\text{C})$ and $T_d = 3^\circ\text{C}$ for all of the heaters in 5-piece configuration (Figure 7.10).

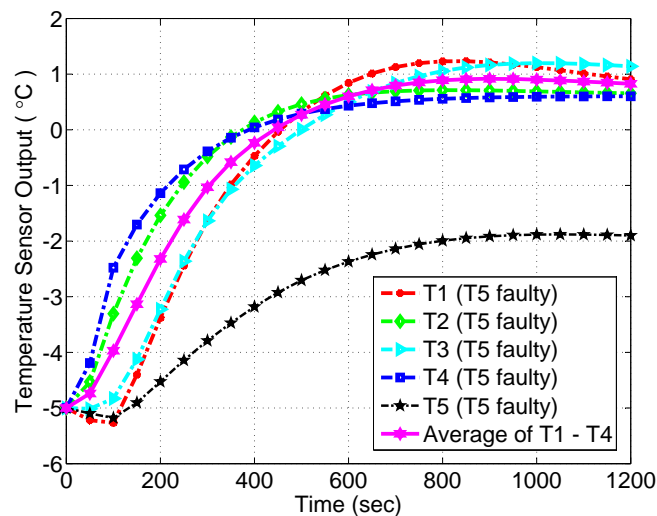


Figure 7.12: Temperature sensor outputs with faulty sensor 5 in the network and using average of sensors 1 to 4 for “HTR5”, proportional controller with $k_p = 500 \text{ Watt}/(\text{m}^2 \cdot ^\circ\text{C})$ and $T_d = 3^\circ\text{C}$ for all of the heaters in 5-piece configuration (Figure 7.10).

performance of de-icing in the modeled distributed network. In this faulty scenario (Figure 7.12), the average temperature of the other sensors (sensor 1 to 4) is used instead. It is seen in Figure 7.12 that this temperature estimation of sensor 5 is not very accurate due to a larger difference in response of the temperature sensor 5 compared to the other sensors (shown in Figure 7.11). Therefore, this faulty scenario for a single temperature

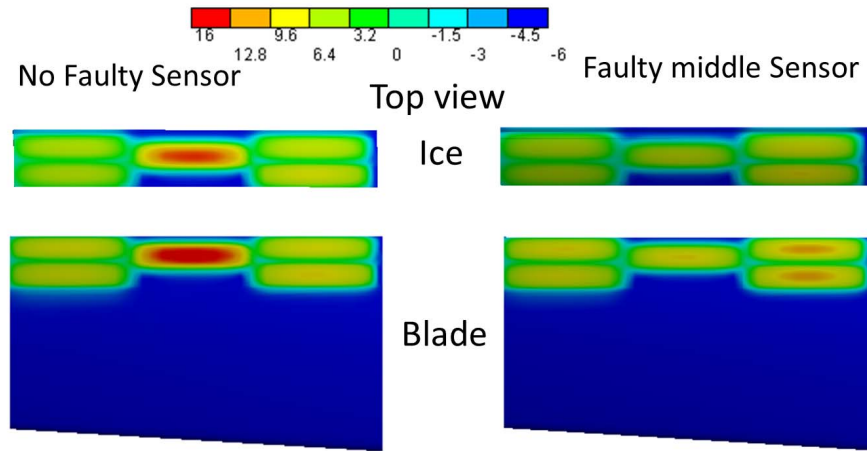


Figure 7.13: Temperature distribution of the ice and blade top surfaces at $t = 1200$ seconds for the modeled 5-piece heater for two scenarios of no faulty sensor and faulty sensor 5.

sensor is the worst case scenario of a faulty sensor in this layout.

It is seen in Figure 7.12 that the average temperature of sensors 1 to 4 estimates larger values than the real temperature of sensor 5 at all times. This leads to a larger temperature error (difference between current and desired temperature of melting T_d) inside the proportional controller for “HTR5”. The reduction of this temperature error term causes an under-heating in “HTR5” for this faulty scenario. Figure 7.13 shows the comparison of temperature distribution at the middle region of the ice layer and the blade for two different scenarios at $t = 1200$ seconds. It is seen that even while having a faulty temperature sensor in this network, heat flux propagates very well through the ice layer and it can be visually seen that ice melting is still successfully achieved under this faulty scenario. In conclusion, this analysis shows that the applied closed-loop proportional controller for de-icing is robust to a known faulty temperature sensor for this distributed layout of heaters. Similar analysis can be done for higher number of known faulty sensors in the network. The proximity of temperature measurements from the sensors 1 through 4 in Figure 7.11 intuitively shows that this network will still be relatively robust to a higher number of faulty temperature sensors by just using the average of known healthy sensors for those corresponding heaters with the faulty sensors.

7.6 Conclusions

Closed-loop numerical simulations of active de-icing using resistive heating and direct temperature sensing have been investigated on a blade segment of a wind turbine blade using ANSYS. A script-base module was developed in ANSYS which provides the capability of (i) closed-loop de-icing simulations for a distributed network of sensors and actuators, (ii) investigating different closed-loop thermal control schemes and their de-icing efficiency, and (iii) optimizing of the controller parameters for each heater in a distributed network to provide more effective de-icing. It was shown that closed-loop control provides much faster de-icing than an open-loop constant heat flux thermal actuation strategy with the same average heat flux. High intensity pulsed thermal actuation slightly improves ice melting but relatively increases the amount of applied thermal stress to the blade structure. The developed computational module can be used to investigate more advanced closed-loop controller schemes for active de-icing using a distributed network of heaters and sensors on wind turbines and aerial vehicles. The developed computational methodology can also be used to investigate the optimal location of the sensors and thermal actuators in a distributed network. Computational modeling of more complex ice dynamics and geometries is also an area of future work.

Chapter 8

Conclusions and Recommendations

Ice accumulation on wind turbine blades in cold regions decreases the aerodynamic power generation by 20-40%. Icing also creates additional loads and mass imbalance on the blade structure which reduce the operational life of the wind turbine. Passive solutions including hydrophobic coatings or spraying anti-freezing chemicals on the blades are not effective under medium to heavy icing conditions and therefore active de-icing techniques need to be implemented for higher effectiveness.

Due to varying amounts of heat loss in different regions of a rotating blade, a more energy efficient de-icing method requires different amounts of thermal power in different blade regions. This motivated this research to use distributed heating with adjustable local heat flux to reduce power consumption for de-icing. Thermodynamic analysis discussed in chapter 3 showed this noticeable variation of required heat flux for different locations, normally with the highest value at the leading edge of the tip of the blade. In such a system, a more accurate direct ice detection on the blade can further reduce the total energy consumption for de-icing by activating those thermal actuators in the icy regions with suitable amount of input power through closed-loop control. In chapter 4, a de-icing profitability analysis was explained without considering maintenance costs of a wind plant. It was shown that de-icing is more profitable for larger wind turbines (especially larger than 1 MW) installed in wind plants with more severe icing conditions. For a more detailed economical analysis of de-icing on wind turbines, this preliminary model needs to be upgraded by considering further factors including design cost and maintenance cost of integrated de-icing system as well as the cost of wind energy production. In chapter 2, the experimental proof of concept of a direct optical ice sensing technique is explained using Optical Frequency Domain Reflectometry (OFDR). The

developed optical sensing technique detects the type of ice or water on the blade by characterizing the reflection from the surface. It also accurately detects the thickness of ice within micron range accuracy. The developed experimental optical sensing method can be used for active distributed de-icing of wind turbines. For commercialization of this approach on a wind turbine, authors suggest the following design improvements: (1) The total cost of the system relative to the manufacturing cost of wind turbine needs to be reduced. This includes the cost of each individual optical sensor as well as the cost of laser source to support the entire network of optical sensors. (2) In order to be utilized in a commercial wind turbine, the size of OFDR setup needs to be reduced to a portable size. (3) Upgrading the current optical sensors with optical fibers to wireless optical fibers provides design versatility and ease of use on a rotating blade. (4) Robustness improvement of the current developed optical sensing response to larger structural vibrations is suggested for improving the reliability of proposed technique under real operational conditions of a wind turbine in cold regions.

In chapter 5, experimental results of closed-loop de-icing were presented using distributed optical ice sensors, temperature sensors, and resistive heaters on a stationary turbine blade part at a fixed pitch angle inside a custom icing chamber. OFDR was used for direct detection of ice on the blade. Distributed temperature sensors mounted at the leading edge of the blade are used for input to the closed-loop controller. Each resistive heater was surrounded by optical ice sensors which were used to inform a heater on/off decision. Scaling up, the experiments showed that using combined OFDR with temperature sensing and distributed PID control uses a total power expenditure of less than 0.5% of the rated power under light/medium icing conditions; de-icing could yield a larger percentage of power improvement and a longer turbine up-time in cold regions. The power consumption for this localized heating was only about 10% of uniformly heating the blade. Furthermore, de-icing performance of high-intensity pulsed actuation versus continuous low intensity actuation was experimentally investigated. The experimental results showed that using high intensity Pulse Amplitude Modulation (PAM) actuation achieves better ice melting performance than continuous PID control but slightly increases the maximum applied blade temperature and thermal stress to the blade structure. Similar results were achieved computationally using the developed framework for computational closed-loop de-icing discussed in chapter 7. The computational approach is validated with

our experimental results using PID control discussed in chapter 5. This presented framework can be used for closed-loop simulations of de-icing on wind turbines and aerial vehicles. A script-based module was developed in ANSYS-APDL software for implementation of different closed-loop thermal controllers. This module enables the capability of closed-loop de-icing simulations using different distributed thermal actuation scenarios for any number and layout of heaters and temperature sensors. The results were presented for a low intensity continuous proportional controller and a higher intensity pulsed proportional controller. The results showed that despite the simplicity of the controller scheme, its de-icing time is about 4 times faster than an open-loop constant heat flux thermal actuation with the same amount of total energy consumption. In addition, the closed-loop controllers reduce the maximum temperature and the volume of high-temperature regions on the blade structure. Further, the computational model was employed to optimize the de-icing response based on surrogate modeling (a computational model for engineering design). De-icing response was quantitatively characterized by calculating a de-icing performance cost function for different values of controller gains. The Multi-Objective Genetic Algorithm (MOGA) optimization tool was used in ANSYS for calculation of the optimal values of controller parameters for a network of distributed resistive heaters on the blade. Different surrogate models were used to enhance the computational efficiency of this approach. The results showed that larger controller gains need to be selected for those heaters that are closer to the blade leading edge due to larger amount of convective heat loss in that region. Furthermore, analysis of existence of a faulty temperature sensor in a distributed network of heaters and temperature sensors showed that closed-loop de-icing is robust to a limited number of known faulty sensors.

The developed and experimentally validated computational framework in this dissertation is a powerful tool that can be used for design and performance evaluation analysis of active distributed de-icing on rotating wind turbines. This tool can be used for design of different heater geometries and layouts as well as evaluation and optimization of closed-loop thermal actuation under different icing conditions for different wind turbine sizes. As explained in chapter 7, this model considers ice melting on the blade but does not model ice shedding due to extreme complexity. After finalizing the layout design and closed-loop actuation strategy, this model can be used for quantitative optimization of closed-loop control parameters by minimization of a de-icing performance cost function to achieve faster de-icing while reducing volume

of high-temperature regions on the blade during de-icing. Ice melting can be visually simulated versus time for different complex ice geometries. The developed framework can also be used to find optimal location of the sensors and resistive heaters knowing the layout and the thermal controller scheme. Furthermore, it can be used to identify those blade areas that do not properly receive thermal flux which can be used to improve heater layout design and closed-loop control strategy to achieve better distributed de-icing.

In summary, main advantages of OFDR ice sensing and closed-loop resistive heating for active de-icing are:

- Significant improvement of aerodynamic power efficiency under icing conditions, annual gross energy production, and longer life expectancy of wind turbines under icing conditions
- Accurate local ice sensing with the capability of additional ice type and thickness information
- Significant de-icing power consumption reduction by only heating up detected icy regions as well as adjusting local input thermal energy at different locations compatible with different nature of heat transfer at different blade areas
- Significant reduction of high-temperature areas on the blade structure by means of distributed closed-loop thermal control

However, cons of this system is potentially high installation cost of embedding distributed optical sensors (wired) and heaters inside rotating blades. Developing a wireless optical sensing with lower cost, and system portability is an important step before commercialization of this system on wind turbines.

The goal of this research has been to provide experimental and computational tools for development and commercialization of more effective ice sensing and active de-icing systems on wind turbines operating under icing conditions.

Bibliography

- [1] ANSYS. Ansys online help manual. <https://www.sharcnet.ca/help/index.php/ANSYS>.
- [2] ANSYS. Ansys theory reference manual. [http://148.204.81.206/Ansys/150/ANSYS Mechanical APDL Theory Reference.pdf](http://148.204.81.206/Ansys/150/ANSYS%20Mechanical%20APDL%20Theory%20Reference.pdf).
- [3] ANSYS. Ansys workbench software. www.ANSYS.com.
- [4] S. Barber, W. Wang, S. Jafari, N. Chokani, and R. S. Abhari. The effect of icing on wind turbine performance and aerodynamics. In Proc. European Wind Energy Conf., 2010.
- [5] I. Baring-Gould, L. Tallhaug, G. Ronsten, R. Horbaty, R. Cattin, T. Laakso, M. Durstewitz, A. Lacroix, E. Peltola, and T. Wallenius. Recommendations for wind energy projects in cold climates. Tech. rep. International Energy Agency, 2009.
- [6] L. Battisti, P. Baggio, and R. Fedrizzi. Warm-air intermittent de-icing system for wind turbines. Wind Engineering, 30(5):361–374, 2006.
- [7] L. Battisti, A. Brighenti, S. D. Savio, and S. Dell’Anna. Evaluation of anti-icing energy and power requirement for wind turbine rotors in cold climates. In BOREAS VII - Proc. Conf. on Wind Energy Production in Cold Climates, Saariselka, Finland, 2005.
- [8] Y. Boluk. Adhesion of freezing precipitates to aircraft surfaces. Transport Canada, 1996.
- [9] M. B. Bragg and E. Loth. Effects of large-droplet ice accretion on airfoil and wing aerodynamics and control. Tech. rep., U.S. Department of Transportation, Federal Aviation Administration, Office of Aviation Research, Report No. DOT/FAA/AR-00/14, 2000.
- [10] Dassault Systemes. Solidworks software. www.solidworks.com.
- [11] S. Dierer, R. Oechslin, and R. Cattin. Wind turbines in icing conditions: performance and prediction. Adv. Sci. Res., 6:245–250, 2011.
- [12] M. Etemaddar, M. O. L. Hansen, , and T. Moan. Wind turbine aerodynamic response under atmospheric icing conditions. Wind Energy, 17:241–265, 2014.
- [13] S. Fikke, G. Ronsten, A. Heimo, S. Kunz, M. Ostrozlik, P. E. Persson, J. Sabata, B. Wareing, B. Wichura, J. Chum, T. Laakso, K. Sntti, and L. Makkonen. Atmospheric icing on structures: Measurements and data collection on icing: State of the art. Tech. Rep. MeteoSwiss, 75, 2006. 110 pages.

- [14] R. C. Finke and B. A. Banks. Piezoelectric de-icing device. Tech. Rep., United States Patent number 4545553 A, 1985.
- [15] P. L. Fuhr and D. R. Huston. Multiplexed fiber optic pressure and vibration sensors for hydroelectric dam monitoring. *Smart Mater. Struct.*, 2:260, 1993.
- [16] J. Gerald, G. Hickman, A. Khatkate, and D. Pruzan. Measuring ice distribution on a surface with attached capacitance electrodes. Tech. Rep., United States Patent number 5-551-288, 1996.
- [17] V. H. Gray, D. T. Bowden, and U. Von Glaim. Preliminary results of cyclical de-icing of a gas-heated airfoil. Tech. Rep. National Advisory Committee for Aeronautics Research Memorandum, Rep. NACA RM E51J29, 1952.
- [18] C. Hochart, G. Fortin, J. Perron, and A. Ilinca. Wind turbine performance under icing conditions. *Wind Energy*, 11(4):319–333, 2008.
- [19] M. Homola, P. Nicklasson, and P. Sundsbo. Ice sensors for wind turbines. *J. Cold Regions Science and Technology*, 46:125–131, 2006.
- [20] R. Huber, M. Wojtkowski, and J. G. Fujimoto. Fourier domain mode locking (fdml): A new laser operating regime and applications for optical coherence tomography. *J. Optics Express*, 14:3225–3237, 2006.
- [21] A. Ilinca. *Analysis and Mitigation of Icing Effects on Wind Turbines*, Book Chapter in *Wind Turbines*. Edited by Ibrahim Al-Bahadly, 1st Edn, InTech, 2011.
- [22] International Organization for Standardization. Atmospheric icing of structures. Tech. Rep. ISO-12494, ISO copyright office, Geneva, Switzerland, 2001.
- [23] S. Kimura, H. Seifert, B. Tammelin, and K. Ishizawa. Flow around the airfoil with ice accretion. In *BOREAS II- Proc. Conf. on Wind Energy Production in Cold Climates*, Pyhtunturi, Finland, pages 205–216, 1994.
- [24] S. Kraemer. Will heat be the winner in de-icing turbine blades? *Wind Energy update*, August 2014.
- [25] T. Laakso, I. Baring-Gould, M. Durstewitz, R. Horbaty, A. Lacroix, E. Peltola, G. Ronsten, L. Tallhaug, and T. Wallenius. State-of-the-art of wind energy in cold climates. Tech. rep. International Energy Agency, 2009.
- [26] T. Laakso and E. Peltola. Review on blade heating technology and future prospects. In *BOREAS VII - Proc. Conf. on Wind Energy Production in Cold Climates*, Saariselka, Finland, 2005.
- [27] J. P. Lewis and D. T. Bowden. Preliminary investigation of cyclic de-icing of an airfoil using an external electric heater. Tech. Rep. National Advisory Committee for Aeronautics Research Memorandum, Rep. NACA RN E51J30, 1952.
- [28] J. Makinen. Ice detection and de-icing system improves the economics of a wind turbine in the arctic weather conditions. In *BOREAS III Proc. Conf. on Wind Energy Production in Cold Climates*, Saariselka, Finland, 1996.
- [29] L. Makkonen. Detection of ice from humidity measurements. Tech. Rep., Report in Finnish to the Vilho, Yrjo and Kalle Vaisala Foundation, Helsinki, Finland, 2000.

- [30] M. Marjaniemi and E. Peltola. Blade heating element design and practical experiences. In BOREAS IV Proc. Conf. on Wind Energy Production in Cold Climates, Yllas, Finland, 1998.
- [31] J. Mason. The physics of clouds. Tech. Rep., Oxford University Press, Ely House, London, England, 1971.
- [32] MathWorks. Matlab software. <http://www.mathworks.com>.
- [33] C. Mayer, A. Illinca, G. Fortin, and J. Perron. Wind tunnel study of electro-thermal de-icing of wind turbine blades. Int. J. Offshore and Polar Engineering, 17:182–188, 2007.
- [34] E. D. Moore and R. R. McLeod. Phase-sensitive swept-source interferometry for absolute ranging with application to measurements of group refractive index and thickness. J. Optics Express, 19:8117–8126, 2011.
- [35] N. Mulherin, J. Richter-Menge, T. Tantillo, L. Gould, G. Durell, and B. Elder. Laboratory test for measurement of adhesion strength of spray ice to coated flat plates. Lab. Rep. 90-2, US Army Corps of Engineers, Cold Regions Research and Engineering, 1990.
- [36] NASA Glenn Research Center. Users manual for lewice version 3.2, 2008.
- [37] NASA Glenn Research Center Icing Branch. Lewice software.
- [38] National Instruments Corporation. Labview software. <http://www.ni.com>.
- [39] Newmerical Technologies. Fensap-ice software: In-flight icing simulation system.
- [40] OMEGA Engineering. <http://www.omega.com>.
- [41] J. L. Palacios, H. Gao, E. C. Smith, and J. L. Rose. Ultrasonic shear wave anti-icing system for helicopter rotor blades. Proc. 62nd Annual Forum of American Helicopter Society, Phoenix, AZ. 11 pages.
- [42] M. Papadakis, H. Yeong, S. Wong, M. Vargas, and M. Potapczuk. Experimental investigation of ice accretion effects on a swept wing. Tech. rep., U.S. Department of Transportation, Federal Aviation Administration, Office of Aviation Research, Report No. DOT/FAA/AR-05/39, 2005.
- [43] O. Parent and A. Ilinca. Anti-icing and de-icing techniques for wind turbines: Critical review. J. Cold Regions Science and Technology, 65:88–96, 2011.
- [44] A. Parrish, M. Rais-Rohani, and A. Najafi. Crashworthiness optimization of vehicle structures with magnesium alloy parts. Int. J. of Crashworthiness, pages 1–23, 2012.
- [45] S. Ramanathan. An Investigation on the De-icing of Helicopter Blades Using Shear Horizontal Guided Waves, Ph.D. Thesis. PhD thesis, Pennsylvania State University, 2005.
- [46] T. Reid and G. Baruzzi. Fensap-ice: Unsteady conjugate heat transfer simulation of electrothermal de-icing. J. of Aircraft, 49:1101–1109, 2012. No. 4.
- [47] T. Reid, G. Baruzzi, and I. Ozcer. Fensap-ice simulation of icing on wind turbine blades, part 1: Performance degradation. In Proc. 51st AIAA Aerospace Sciences Meeting, Grapevine, Texas, 2013. 18 pages.

- [48] T. Reid, G. Baruzzi, and I. Ozcer. Fensap-ice simulation of icing on wind turbine blades, part 2: Ice protection system design. In Proc. 51st AIAA Aerospace Sciences Meeting, Grapevine, Texas, 2013. 14 pages.
- [49] F. Richert. Is rotorcraft icing knowledge transferable to wind turbines? In BOREAS III Proc. Conf. on Wind Energy Production in Cold Climates, Saariselka, Finland, pages 366–380, 1996.
- [50] G. Ronsten, T. Wallenius, M. Hulkkonen, I. Baring-Gould, R. Cattin, M. Durstewitz, A. Krenn, T. Laakso, A. Lacroix, L. Tallhaug, O. Byrkjedal, and E. Peltola. State-of-the-art of wind energy in cold climates. Tech. Rep., IEA Wind Task 19, October 2012 Edition, 2012.
- [51] H. Seifert. Technical requirements for rotor blades operating in cold climate. In BOREAS VI-Proc. Conf. on Wind Energy Production in Cold Climates, Pyhtunturi, Finland, page 13, 2003.
- [52] H. Seifert and F. Richert. Aerodynamics of iced airfoils and their influence on loads and power production. In Proc. European Wind Energy Conf., 1997.
- [53] H. Seifert and F. Richert. A recipe to estimate aerodynamics and loads on iced rotor blades. In BOREAS IV- Proc. Conf. on Wind Energy Production in Cold Climates, Hetta, Finland, pages 305–316, 1998.
- [54] S. Shajjee, L. Y. Pao, and R. R. McLeod. Monitoring Ice Accumulation and Active De-Icing Control of Wind Turbine Blades, Chapter in Wind Turbine Control and Monitoring. Springer, Advances in Industrial Control series, N. Luo, Y. Vidal, and L. Acho (Eds.), 2014. ISBN 978-3-319-08412-1.
- [55] S. Shajjee, L. Y. Pao, and R. R. McLeod. Optimizing the layout of heaters for distributed active de-icing of wind turbine blades. Wind Engineering, 38(6):587–600, 2014.
- [56] S. Shajjee, L. Y. Pao, P. Wagner, E. D. Moore, and R. R. McLeod. Direct ice sensing and localized closed-loop heating for active de-icing of wind turbine blades. In Proc. American Control Conf., Washington, D.C., pages 634–639, 2013.
- [57] S. Shajjee, P. Wagner, L. Y. Pao, and R. R. McLeod. Development of a novel ice sensing and active de-icing method for wind turbines. In Proc. AIAA Aerospace Sciences Meeting, Nashville, Tennessee, 2012. 15 pages.
- [58] D. Shields. A Modeling Study of Ice Accretion on a NACA 4412 Airfoil, Masters Thesis. PhD thesis, Rensselaer Polytechnic Institute, Connecticut, 2011.
- [59] VTT technical research center of Finland. Turbice (turbine blade icing model) software.
- [60] M. Wadham-Gagnon. Quebec’s wind energy industry’s concerns and initiatives relative to cold climate. Wind Power O&M in Canada Part 2, Wind Energy update, August 2014.
- [61] M. Walsh. Accretion and Removal of Wind Turbine Icing in Polar Conditions, Masters Thesis. PhD thesis, AALTO University, Finland, 2010.
- [62] X. Wang. Convective Heat Transfer and Experimental Icing Aerodynamics of Wind Turbine Blades. PhD thesis, University of Manitoba, 2008.

Appendix A

Notation

| | |
|----------------|--|
| A_H | Total area of the heaters |
| AoA | Angle of attack |
| Bi | Biot number |
| c | Chord length |
| c_{tip} | Chord length at the tip of the blade |
| d_H | Distance between two adjacent heaters in the network |
| f | Controller update frequency |
| h | Convective coefficient of heat transfer |
| i_c | Controller switching index |
| J | De-icing performance cost function |
| J_{t_f} | De-icing performance cost function value at the final time |
| K | Thermal conductivity |
| k_p | Gain of the proportional controller |
| $N_{P_{heat}}$ | Ratio of power consumed for de-icing to average wind turbine power |
| Nu_x | Local Nusselt number on the airfoil |
| n_H | Total number of resistive heaters in the distributed network |
| P | Wind turbine rated power |
| P_{ice} | Power generated by the wind turbine with accumulated ice on the blades |
| P_{no-ice} | Power generated by the wind turbine when there is no ice on the blades |

| | |
|------------------|--|
| P_{out} | Average power produced by the wind turbine |
| $Q_{net,ADIS}$ | Energy production by the wind turbine with anti/de-icing system (ADIS) |
| $Q_{net,noADIS}$ | Net energy production by the wind turbine with no anti/de-icing system |
| Q_{out} | $P_{out}t$, Average output energy production by the wind turbine |
| Q_{th} | Anti/de-icing thermal energy |
| \dot{Q}_{th} | Anti/de-icing thermal power |
| q | input heat flux to the thermal resistor |
| q_{conv} | Convection loss heat flux |
| q_{max} | Maximum thermal resistor heat flux at maximum applied voltage |
| q_{sice} | Sensible heat flux required to bring ice temperature to zero degree Celsius in the solid phase |
| q_{latice} | Latent heat flux required for phase change of ice from solid to liquid at zero degree Celsius |
| q_{loc} | Required anti/de-icing local heat flux |
| R | Span-wise radius (distance from the hub) |
| R_{tip} | Span-wise radius at the blade tip |
| T | Temperature |
| T_0 | Desired outer blade surface temperature |
| T_{amb} | Ambient temperature |
| $T_c(t)$ | Current blade surface temperature at time t |
| T_d | Desired blade surface temperature |
| T_{max_b} | Maximum global temperature on the surface of the blade during de-icing |
| t | Time |
| t_{di} | De-icing time |
| $t_{Heat-On}$ | Time heating system is on |
| t_{ice} | Time duration of operating wind turbine with accumulated ice |
| u_w | Wind speed |
| V_{ice} | Volume of ice residue |
| V_{LE1} | Volume of ice residue for "LE ice 1" layer |

| | |
|-----------------|--|
| V_{LE2} | Volume of ice residue for “LE ice 2” layer |
| V_{NonLE} | Volume of ice residue for “Non-LE ice” layer |
| $V_{T>T_0}$ | Volume of the blade experiencing temperature higher than T_0 |
| v | Input voltage to the thermal resistors |
| v_{max} | DC input voltage to the resistor at maximum power |
| W_m | Weighting matrix in de-icing performance cost function |
| X | De-icing performance state vector |
| x | Chord-wise distance from the leading edge of the blade |
| x_b | Longitudinal blade axis along resistor columns |
| y_b | Lateral blade axis along resistor rows |
| β | Constant coefficient for the distance between the heaters |
| Δ_{ice} | Ice thickness on the blade |
| η_{ADIS} | Anti/de-icing efficiency factor |
| η_{ice} | Power loss ratio due to icing |
| ω | Angular velocity of the rotating blade |
| τ_{de-ice} | Heating-time ratio |

Appendix B

Matlab Codes for Calculations of Sensible and Latent Heat Flux for Ice Melting

```
%% Thermal characteristics of ice
% this code calculates amount of heat flux (latent and sensible)
% knowing the type of ice, ice temperature,
% volume of ice, and time to melt.

close all
clear all

%% input parameters

type = input ('type 1=glaze ice, 2= hard rime, 3= soft rime');

if type ==1
    rho_ice = 900 ; %kg/m^3 for glaze ice
elseif type ==2
    rho_ice = 750 ; %kg/m^3 for hard rime ice (600-900)
elseif type ==3
    rho_ice = 400 ; %kg/m^3 for soft rime ice (200-600)
end
```

```

T0_ice = input('Initial ice temperature (C)');
t_deice = input('De-icing time by active de-icing system (minutes)');

t = t_deice*60; % minute to seconds conversion

% coefficients of fitted curve
%for ice mass rate distribution along the radius of the blade
[Coef, dMdt_ice, r, M_ice, th_mean_ice] = ice_dist();
a0 = Coef(1);
b0 = Coef(2);
c0 = Coef(3);
d0 = Coef(4);
e0 = Coef(5);

%% 10% ice thickness melting for shedding due to centrifugal force
A_ice = (3) * (63); % ice adhesion area in m^2
n = 0.1; % proportion of ice thickness to be melted (10%)
th_ice = n.*(th_mean_ice); % ice thickness in meter

Vol_ice = A_ice*th_ice; % for an ice rectangle cube
m_ice = rho_ice*Vol_ice; % mass of ice to be melted
mdot_ice = m_ice/t_deice; % kg/sec melting mass rate

Tf_ice = 0; % final temperature of ice in Celsius

% J/kgK at for ice (phase change from solid to liquid)
% Linearization between 0C- -20C from thermodynamic tables

```

```

Cp_ice = 5.35*(T0_ice + Tf_ice)/2 + 2050;

%% Sensible heat, heat rate and heat flux calculation for ice

% Sensible heat rate
% to bring ice at T0 to zero degree Celsius solid ice
Qdot_Sens_ice = mdot_ice.*Cp_ice.*(Tf_ice - T0_ice);

q_Sens_ice = Qdot_Sens_ice./A_ice; % sensible heat flux for ice

%% Latent heat of fusion for ice
Lf = 333300; %J/kg latent heat of fusion of ice
Qdot_latent_ice = mdot_ice.*Lf; %watts
% Latent heat flux (Watts/m^2) (1 watt/in^2= 1550.0031 watt/m^2)
q_latent_ice = Qdot_latent_ice./A_ice;
q_total = q_latent_ice + q_Sens_ice;

%% Jacob number : ratio of sensible heat to the latent heat
Ja = q_Sens_ice/ q_latent_ice;

%%
figure()
plot(r, q_latent_ice)
xlabel('Radii (m)')
ylabel('latent heat flux for ice phase change (Watts/m^2)')
grid on;

figure()
plot(r, q_Sens_ice)

```

```

xlabel('Radii (m)')
ylabel('Sensible heat flux (Watts/m^2)')
grid on;

figure()
plot(r, q_total)
xlabel('Radii (m)')
ylabel('(Sensible+Latent) heat flux for de-icing (Watts/m^2)')
grid on;

% This code calculates dM_ice/dt
% based on Makonnen 1994 ice accretion model
function [Coef, dMdt_ice, r, M_ice, th_mean_ice] = ice_dist()
%% air
T_amb = -20; % deg C ambient temperature
To = 2; % dec C blade outer surface temperature
k_air = 0.025; % (w/mK)
rho_air = 1.3943; %kg/m^3
mu_air = 1.488*10^(-5); %dynamic viscosity of air at -20C (kg/(ms))
nu_air = 9.49*10^(-6); %kinematic viscosity of air at -20C
Pr_air = 0.7211; % Prandtl number of air at -20C

%% Turbine parameters for Vestas 1.8 MW
alpha = 0*(pi/180); % angle of attack of the blade in rad
RPM= 12.15; % rpm of wind turbine
omega = RPM*(2*pi)/60; % angular velocity of turbine in rad/sec
u_inf = 10; % free stream velocity in m/sec

```

```

r_tip = 61.633; % span of the blade or radius of tip in meters

% 5 MW NREL blade geometry
r = [2.8667 5.6000 8.3333 11.7500 15.8500 19.9500 24.0500 ...
... 28.1500 32.2500 36.3500 40.4500 44.5500 48.6500 52.7500 ...
... 56.1667 58.9000 61.6333];

Chord = [3.542 3.854 4.167 4.557 4.652 4.458 4.249 4.007 3.748 ...
... 3.502 3.256 3.010 2.764 2.518 2.313 2.086 1.419];

% Calculating blade total velocity (u_rel) at radius r
a=0; % axial induction factor

% tangential flow induction
a_prim=0; %a_prim = u_inf^2*a*(1-a)./(r.^2*omega^2);
u_wind = u_inf*(1-a); %m/sec
u_tang = r.*omega.*(1+a_prim); % tangential velocity to the blade
u_rel = sqrt(u_wind.^2+u_tang.^2);
Re_C = rho_air.*u_rel.*Chord./mu_air; % local Reynolds number

% Calculating collision efficiency (alpha1)
d = 50*10^(-6); % droplet diameter (MVD): 2-50 micro meter typically
LWC = 1*10^(-3); % liquid water content 0.1-2.5 g/m^3
rho_w = 1000; % water density (kg/m^3)
mu_air= 1.488*10^(-5); % dynamic viscosity kg/(m.s) of air at -20C
D = 0.05; % surface cross sectional diameter

```

```

K_Stokes      = rho_w.*d^2.*u_rel./(9*mu_air*D);
Re_drop       = rho_air.*u_rel*d/mu_air;
Phi_alpha1    = Re_drop.^2./K_Stokes;

A_alpha1 = 1.066.*K_Stokes.^(-0.00616).*exp(-1.103.*K_Stokes.^(-0.688));
B_alpha1 = 3.641.*K_Stokes.^(-0.498).*exp(-1.497.*K_Stokes.^(-0.694));
C_alpha1 = 0.00637.*(Phi_alpha1-100).^ (0.381);

alpha1        = A_alpha1-0.028-C_alpha1.*(B_alpha1-0.0454);

% Calculating sticking efficiency
alpha2 = zeros(1,length(u_rel));
for i=1:length(alpha2)
    if u_rel(i) < 1
        alpha2(:,i) = 1;
    else
        alpha2(:,i) = 1/u_rel(i);
    end
end

% Accretion efficiency (alpha3)
alpha3 = 1;

% Assuming constant airfoil thickness
% throughout the blade from root to tip

th_mean_blade = 0.03; % Mean blade thickness
Area_cross = Chord.*th_mean_blade;

```

```

dMdt_ice = alpha1.*alpha2.*alpha3.*LWC.*u_rel.*Area_cross;
t_ice = 2*60*60; % Seconds
M_ice = dMdt_ice.*t_ice;
rho_ice = 900; % density for glaze ice = 900 kg/m^3
Vol_ice = M_ice/rho_ice;

% Length of ice at the airfoil (relative to chord length)
l_ice = Chord./10;
th_mean_ice = Vol_ice./l_ice;

Coef = polyfit(r, dMdt_ice,4);
% Coefficients of fitted curve for ice mass rate distribution
% along the radius of the blade
a0 = Coef(1);
b0 = Coef(2);
c0 = Coef(3);
d0 = Coef(4);
e0 = Coef(5);
dMdt_fit = a0*r.^4 + b0*r.^3 + c0*r.^2 + d0*r + e0;

```

Appendix C

ANSYS-APDL Codes for Closed-Loop Distributed Thermal Actuation

C.1 Codes written for the Implementation of a Proportional Closed-Loop Controller

C.1.1 Heat flux Initialization for a Network of Five Heaters

```
!Active UNIT system in Workbench when this object was created:
!Metric (m, kg, N, s, V, A)
!NOTE: Any data that requires units (such as mass) is assumed to be
!in the consistent solver unit system.
!See Solving Units in the help system for more information.
numHTR=5          !Number of distributed heaters in the network
*DIM,HTRnm,CHAR,numHTR,1,1, , ,
!List heater Names
HTRnm(1,1,1)='HTR1Surf'
HTRnm(2,1,1)='HTR2Surf'
HTRnm(3,1,1)='HTR3Surf'
HTRnm(4,1,1)='HTR4Surf'
HTRnm(5,1,1)='HTR5Surf'
*DO,K,1,numHTR,1
/PREP7
! Select surface
```



```

cmsel,s,%HTRnm(K,1,1)%
et,50000+K,152
keyop,50000+K,8,1
type,50000+K
mat,50000+K
real,50000+K

Esurf

ESEL,TYPE,50000+K

!Apply heat flux

/SOLU

!SFE,All, ,HFLUX, , %TDHFLX%

SFE,All, ,HFLUX, , 3000

ALLS

*ENDDO

```

C.1.2 Proportional Controller Communicating with the Finite-Element Solver

```

numHTR=5

*DIM,HTRnm,CHAR,numHTR,1,1, , ,

!List heater Names

HTRnm(1,1,1)='HTR1Surf'

HTRnm(2,1,1)='HTR2Surf'

HTRnm(3,1,1)='HTR3Surf'

HTRnm(4,1,1)='HTR4Surf'

HTRnm(5,1,1)='HTR5Surf'

! List Temperature Sensor Names

*DIM,TempNode,CHAR,numHTR,1,1, , ,

TempNode(1,1,1)='TempNod1'

```

```

TempNode (2,1,1) ='TempNod2'
TempNode (3,1,1) ='TempNod3'
TempNode (4,1,1) ='TempNod4'
TempNode (5,1,1) ='TempNod5'
*DIM,Tempavg,ARRAY,numHTR,1,1, , ,
*DIM,Kp_AR,ARRAY,numHTR,1,1, , ,
Kp_AR (1,1,1) =ARG1
Kp_AR (2,1,1) =ARG2
Kp_AR (3,1,1) =ARG3
Kp_AR (4,1,1) =ARG4
Kp_AR (5,1,1) =ARG5
!***** Do not modify below this line *****
*DO,J,1,numHTR,1
!Get the value for the current load-step
*GET,CurLS,ACTIVE,0,SET,LSTP
!Check if we are before the first solve command
*IF,CurLS,EQ,0,THEN
    fini                !Temporarily leave /solu
    /config,noeldb,0    !Write results after a solution
    /solu                !Re-enter/solu
*ENDIF                !End of if statement
cmsel,s,%TempNode(J,1,1)%!Selecting array of temp sensors
!cmsel,s,TempNode1
cnn=0
!Find the number of nodes in the selection
*GET,NumNods,NODE,0,COUNT
*DIM,Tval_all,ARRAY,NumNods,1,1, , ,

```

```

*DO, I, 1, NumNods, 1      !Do loop to loop through the nodes in the selection
/gopr                    !Specify verbose output of this loop
cnn=NDNEXT(cnn)          !Get the current node's number
val=0                    !Reset val to ensure no carryover
      *GET, val, NODE, cnn, TEMP, !Get the current node's temperature
      Tval_all(i, 1, 1)= val
*ENDDO !End of loop

Tempsum=0.0

*DO, I, 1, NumNods, 1
      Tempsum = Tempsum + Tval_all(i, 1, 1)
*ENDDO

!Store all nodal temperatures
!Average the Node Temperature
Tempavg(j, 1, 1)= Tempsum/NumNods

ALLS

-----Implementing Controller to each Heater-----
cmsel, s, %HTRnm(J, 1, 1)% !Selecting array of resistive heaters
!Temperature based closed-loop thermal actuation
!*****APPLY HEAT FLUX
ESEL, TYPE, 50000+J
!Delete previous heat flux
!SFEDELE, ALL, ALL, HFLUX
!Apply new heat flux

Td = ARG6                !Desired temperature of melting
!-----Modeling a faulty temperature sensor
!Replacing temperature of faulty sensor with average of other sensors
!*IF, j, EQ, 5, THEN

```

```

!Tempavg(j,1,1) = (Tempavg(j-1,1,1)+Tempavg(j-2,1,1)+ ...
!
!           ... (Tempavg(j-3,1,1)+Tempavg(j-4,1,1)) / (numHTR-1)
!*ENDIF

!-----Closed-loop controller for heat flux calculation
*IF, Td, GE, Tempavg(j,1,1), THEN
SFE,ALL, ,HFLUX, , Kp_AR(J,1,1)*(Td - Tempavg(j,1,1))
*ELSE
SFE,ALL, ,HFLUX, , 0
*ENDIF

ALLS
*ENDDO

```

C.2 ANSYS Code for Calculation of Volume of Ice Residue

```

Low=-10.0      !Lower bound of temperature
Up=0.0         !Melting temperature of ice in Celsius
timeres=1200

!SET, LAST

SET, NEAR, , 1, , timeres, ,

ETABLE, , TEMP,

CMSEL, S, ICE_Total

!ESEL, R, MAT, , IceMATNU

ESEL, R, ETAB, TEMP, Low, UP, , 0

*GET, nelem, ELEM, , NUM, MAX

*DEL, volume(1), , nopr

*DIM, volume, , NELEM

*DIM, mask, , NELEM

*VABS, 1

```

```

*VGET,volume(1),ELEM,1,GEOM
*VGET,mask(1),ELEM,1,ESEL
*VMASK,mask(1)
*VSCFUN,total_V,SUM,volume(1)
ALLS
*STAT
my_IceVol_1200s = total_V

```

C.3 ANSYS Code for Calculation of High Temperature Regions on the Blade

```

Low=5
Up=100
timeres=1200
!SET, LAST
SET, NEAR, , 1, , timeres, ,
ETABLE, , TEMP,
ESEL, S, MAT, , BladeMATNU
ESEL, R, ETAB, TEMP, Low, UP, , 0
*GET, nelem, ELEM, , NUM, MAX
*DEL, volume(1), , nopr
*DIM, volume, , NELEM
*DIM, mask, , NELEM
*VABS, 1
*VGET,volume(1),ELEM,1,GEOM
*VGET,mask(1),ELEM,1,ESEL
*VMASK,mask(1)
*VSCFUN,total_V,SUM,volume(1)
ALLS

```

*STAT

my_BladeVolTemp30up_200s = total_V